

Preparation and Characterization of Mo/Al Layered Thin Films

by

Jayaramachandran Giridhar

thesis submitted to the Faculty of the
Virginia Polytechnic Institute and State University
in partial fulfillment of the requirements for the degree of
Master of Science
in
Materials Engineering

APPROVED:

Diana Farkas, Chairperson

Charles R. Houska, Co-Chairperson

Jack L. Lytton

April, 1987
Blacksburg, Virginia

Preparation and Characterization of Mo/Al Layered Thin Films

by

Jayaramachandran Giridhar

Diana Farkas, Chairperson

Materials Engineering

(ABSTRACT)

The fabrication of bilayer and multilayer Mo/Al thin films using a conventional multi-target rf-diode sputter deposition system was studied. The films were deposited on glass and Si(100) substrates. The as-deposited films were characterized with respect to their structure and composition profiles using X-Ray diffraction, AES, SEM, TEM, and RBS techniques. The as-deposited bilayer films were of good quality with an interface thickness of about 200 Å. They were annealed at different temperatures in the range of 300-600°C for different times. Diffusional intermixing and phase changes were monitored and diffusivity measurements were made. The growth characteristics of intermetallic compounds were analysed. Mo/Al multilayer thin films with layer thicknesses less than 200 Å were also deposited. An assessment of structural and compositional modulations in these multilayer films revealed the need for the conversion of the conventional diode sources to magnetron sources for improvement of film quality. Also presented are a few preliminary theoretical calculations for high-energy ion-beam mixing of the Mo/Al bilayer thin films.

Acknowledgements

The author wishes to acknowledge the constant advice and support from the committee chairpersons Dr. Diana Farkas and Dr. Charles R. Houska. The author is specially thankful to Dr. Houska for granting permission to use the sputter deposition unit and the facilities in the X-ray laboratory.

The author greatly appreciates and acknowledges the valuable suggestions and ideas in the area of Electron Microscopy from [REDACTED]. The discussions the author had with [REDACTED] in the areas of AES and Sputter-etch composition profiling were very useful in conducting the present study and the author wishes to thank [REDACTED] for the interesting discussions. Thanks also to [REDACTED] for the helpful discussions in RBS analysis and ion-beam mixing.

Special thanks are due to [REDACTED], X-ray Lab technician in the Materials Engineering department, whose immense help, patience and cooperation were responsible for the thin film fabrication being completed. Sincere thanks are also due to [REDACTED], Polymer Lab supervisor in Materials Engineering department, for his help in operating the PHILIPS 420 STEM. The author also wishes to acknowledge the help extended by [REDACTED], Surface Analysis Lab supervisor in Chemistry department in the operation of PERKIN-ELMER PHI610 Scanning Auger Microprobe.

The author wishes to acknowledge the valuable discussions he had with , and of the Naval Research Laboratories, Washington D.C., in the areas of RBS analysis, Thin film fabrication, and ion beam mixing. The author also acknowledges the use of the software package RUMP for the analysis of RBS data, which was developed and distributed by of Cornell University. Special thanks to for providing the RBS experimental data obtained from ion-beam mixed Sn film on Fe substrate and the discussions pertaining to RBS analysis and ion-beam mixing.

Sincere thanks is given to for helping the author in Electron Microscopy work. Very special thanks to for his help, encouragement, and support without which the thesis would not have been completed on time. The author wishes to thank , and for their help and valuable suggestions. The author also thanks his friends and for the help in typing the thesis. Thanks to the secretarial staff of the Materials Engineering department for their assistance.

This work was partially supported by the Graduate Research Development Project (GRDP), Graduate Student Assembly (GSA) of Virginia Tech. and by Office of Naval Research (ONR). The author gratefully acknowledges the above financial support.

Table of Contents

1.0 INTRODUCTION	1
2.0 LITERATURE REVIEW	4
2.1 Fabrication of Layered Thin Films	4
2.1.1 Planar Diode Glow Discharge Sputtering	5
2.1.2 Deposition Parameters and Control	6
2.1.3 Sputter Deposition of Layered Thin Films	12
2.2 The Mo/Al System	16
2.2.1 Phase Diagram and Crystal Structures	16
2.2.2 Diffusion and Reactions	18
2.3 Other BCC/FCC Metallic Layered Thin Films	23
2.4 Techniques of Characterization of Layered Thin Films	25
2.4.1 AES with Argon Ion-beam Sputter-etch Profiling	25
2.4.2 X-Ray Diffraction	27
2.4.3 Analytical Electron Microscopy	29
2.4.4 Rutherford Backscattering Spectroscopy	30

3.0 THEORY	32
3.1 Sputter-etch Composition-Depth Profiling with AES	32
3.2 X-Ray Diffraction	35
3.2.1 X-Ray Line Shape Analysis	36
3.2.2 Diffraction from Ideal Multilayer Thin Films	40
3.3 RBS Analysis for Composition Profiles	42
3.4 Electron Diffraction Patterns	45
3.4.1 Ring Patterns	45
3.4.2 Spot Patterns	46
3.5 Diffusion Analysis for Bilayers	48
4.0 EXPERIMENTAL PROCEDURE	50
4.1 Fabrication of Thin Films	50
4.1.1 Sputter Deposition System	50
4.1.2 Calibration and Control of Sputter Deposition.	52
4.1.3 Measurement of Film Thickness and Deposition Rate	55
4.1.4 Deposition of Mo/Al Bilayer Samples	58
4.1.5 Deposition of Mo/Al multilayers	58
4.2 Annealing Procedure	63
4.3 Characterization of Bilayer Thin Film Samples	64
4.3.1 Analysis using AES	64
4.3.2 Analysis using X-ray diffraction	65
4.3.3 Analysis using STEM	66
4.4 Characterization of Multilayer Films	68
4.4.1 Analysis with AES	68
4.4.2 Analysis using X-ray diffraction	68
4.4.3 Analysis using RBS	69

5.0 RESULTS AND DISCUSSION	70
5.1 Results for Mo/Al Bilayers	70
5.1.1 Analysis of As-deposited Bilayer Films	70
5.1.2 Analysis of Annealed Bilayer Thin Films	78
5.2 Results for Mo/Al Multilayers	120
6.0 CONCLUSIONS AND RECOMMENDATIONS FOR FUTURE WORK	128
REFERENCES	130
Appendix A. CHARACTERISTICS OF MAGNETRON SPUTTERING SOURCES	133
Appendix B. THEORETICAL CALCULATIONS ON ION-BEAM MIXING OF Mo/Al BILAYERS	138
Appendix C. RBS ANALYSIS OF ION-BEAM MIXING OF Sn THIN FILM ON Fe SUBSTRATE	153

List of Illustrations

Figure 1. Planar diode source	7
Figure 2. Multi-target deposition system	8
Figure 3. Effect of sputtering gas pressure	10
Figure 4. Morphology of sputtered films	13
Figure 5. Composition modulation amplitude obtained with a diode source	15
Figure 6. Al-Mo Equilibrium binary phase diagram [Ref.19].	17
Figure 7. Schematic experimental geometry of RBS.	44
Figure 8. Formation of an electron diffraction pattern in a TEM.	47
Figure 9. Film thickness measurement using Å-scope.	57
Figure 10. Measured APPH as a function of sputtering time for an as-deposited bilayer film	72
Figure 11. Sputter-etch rate and Sputter depth as functions of time for an as-deposited bilayer film	73
Figure 12. Bulk concentration versus depth profiles of Mo and Al in an as-deposited bilayer film	74
Figure 13. X-ray diffraction pattern (Intensity vs. 2θ)of an as-deposited Mo/Al bilayer sample.	76
Figure 14. Bright field image and electron diffraction pattern of an as-deposited bilayer film.	79
Figure 15. Electron diffraction pattern of an as-deposited bilayer film showing double diffraction effect.	80
Figure 16. Surface topography of a pure Mo film	81
Figure 17. Surface topography of a pure Al and Mo/Al as-deposited bilayer films.	82
Figure 18. Measured APPH as a function of sputtering time for a bilayer film annealed at 300°C for 3 hours.	84

Figure 19. Sputter-etch rate and Sputter depth as functions of time for a bilayer film annealed at 300°C for 3 hours.	85
Figure 20. Bulk concentration versus depth profiles of Mo and Al in a bilayer film annealed at 300°C for 3 hours.	86
Figure 21. Measured APPH as a function of sputtering time for a bilayer film annealed at 350°C for 3 hours.	87
Figure 22. Sputter-etch rate and Sputter depth as functions of time for a bilayer film annealed at 350°C for 3 hours.	88
Figure 23. Bulk concentration versus depth profiles of Mo and Al in a bilayer film annealed at 350°C for 3 hours.	89
Figure 24. Measured APPH as a function of sputtering time for a bilayer film annealed at 400°C for 3 hours.	90
Figure 25. Sputter-etch rate and Sputter depth as functions of time for a bilayer film annealed at 400°C for 3 hours.	91
Figure 26. Bulk concentration versus depth profiles of Mo and Al in a bilayer film annealed at 400°C for 3 hours.	92
Figure 27. Measured APPH as a function of sputtering time for a bilayer film annealed at 450°C for 3 hours.	93
Figure 28. Sputter-etch rate and Sputter depth as functions of time for a bilayer film annealed at 450°C for 3 hours.	94
Figure 29. Bulk concentration versus depth profiles of Mo and Al in a bilayer film annealed at 450°C for 3 hours.	95
Figure 30. X-ray diffraction pattern (Intensity vs. 2θ) of a Mo/Al bilayer thin film sample annealed at 300°C for 3 hours.	96
Figure 31. X-ray diffraction pattern (Intensity vs. 2θ) of a Mo/Al bilayer thin film sample annealed at 350°C for 3 hours.	97
Figure 32. X-ray diffraction pattern (Intensity vs. 2θ) of a Mo/Al bilayer thin film sample annealed at 400°C for 3 hours.	98
Figure 33. X-ray diffraction pattern (Intensity vs. 2θ) of a Mo/Al bilayer thin film sample annealed at 450°C for 3 hours.	99
Figure 34. X-ray diffraction pattern (Intensity vs. 2θ) of a Mo/Al bilayer thin film sample annealed at 500°C for 3 hours.	100
Figure 35. X-ray diffraction pattern (Intensity vs. 2θ) of a Mo/Al bilayer thin film sample annealed at 600°C for 3 hours.	101
Figure 36. Bright field image and electron diffraction pattern of a bilayer film annealed at 300°C for 3 hours.	104
Figure 37. Bright field image and electron diffraction pattern of a bilayer film annealed at 350°C for 3 hours.	105

Figure 38. Bright field image and electron diffraction pattern of a bilayer film annealed at 400°C for 3 hours.	106
Figure 39. Bright field image and electron diffraction pattern of a bilayer film annealed at 450°C for 3 hours.	107
Figure 40. Bright field image and electron diffraction pattern of a bilayer film annealed at 500°C for 3 hours.	108
Figure 41. Bright field image and electron diffraction pattern of a bilayer film annealed at 600°C for 3 hours.	109
Figure 42. Surface topography of a Mo/Al bilayer film	111
Figure 43. Surface topography of a Mo/Al bilayer film	112
Figure 44. Surface topography of a Mo/Al bilayer film	113
Figure 45. Surface topography of a Mo/Al bilayer film	114
Figure 46. Surface topography of a Mo/Al bilayer film	115
Figure 47. $\ln(D_{\text{Mo}})$ as a function of $(1000/T)$	117
Figure 48. $\ln(D_{\text{Al}})$ as a function of $(1000/T)$	118
Figure 49. Experimental and simulated RBS spectra for a Mo/Al multilayer.	122
Figure 50. Ideal multilayer X-ray diffraction simulation for a film with modulation wavelength $\lambda \sim 400 \text{ \AA}$	124
Figure 51. Ideal multilayer X-ray diffraction simulation for a film with modulation wavelength $\lambda \sim 120 \text{ \AA}$	125
Figure 52. AES composition-depth profile for the Mo/Al multilayer with expected layer thickness of $\sim 200 \text{ \AA}$ of Mo and Al.	127
Figure 53. Circular planar magnetron sputtering source	135
Figure 54. Damage energy profile of sample of a 400 Å Mo layer on Al (sample #1), ion-beam mixed with a 100 keV Ar beam.	140
Figure 55. Concentration profile of sample #1 after ion-beam mixing to a dose of $2 \times 10^{16} \text{ ions/cm}^2$	141
Figure 56. Concentration profile of sample #1 after ion-beam mixing to a dose of $4 \times 10^{16} \text{ ions/cm}^2$	142
Figure 57. Concentration profile of sample #1 after ion-beam mixing to a dose of $6 \times 10^{16} \text{ ions/cm}^2$	143
Figure 58. Concentration profile of sample #1 after ion-beam mixing to a dose of $8 \times 10^{16} \text{ ions/cm}^2$	144
Figure 59. Damage energy profile of a 1200 Å Mo layer on Al (sample #2), ion-beam mixed with a 300 keV Ar beam.	145

Figure 60. Concentration profile of sample #2 after ion-beam mixing to a dose of 2×10^{16} ions/cm ²	146
Figure 61. Concentration profile of sample #2 after ion-beam mixing to a dose of 4×10^{16} ions/cm ²	147
Figure 62. Concentration profile of sample #2 after ion-beam mixing to a dose of 6×10^{16} ions/cm ²	148
Figure 63. Concentration profile of sample #2 after ion-beam mixing to a dose of 8×10^{16} ions/cm ²	149
Figure 64. Damage energy profile of a 4000 Å Mo layer on Al (sample #3), ion-beam mixed with a 1 MeV Ar beam.	150
Figure 65. Concentration profile of sample #3 after ion-beam mixing to a dose of 4×10^{16} ions/cm ²	151
Figure 66. Concentration profile of sample #3 after ion-beam mixing to a dose of 8×10^{16} ions/cm ²	152
Figure 67. Experimental and simulated RBS spectra of an as-deposited ~ 1200 Å Sn film on Fe substrate.	155
Figure 68. Experimental and simulated RBS spectra after irradiation at 20°K and fluence of 4×10^{16} ions/cm ²	156
Figure 69. Experimental and simulated RBS spectra after irradiation at 20°K and fluence of 6×10^{16} ions/cm ²	157
Figure 70. Experimental and simulated RBS spectra after irradiation at 20°K and fluence of 8×10^{16} ions/cm ²	158
Figure 71. Experimental and simulated RBS spectra after irradiation at 180°C and fluence of 4×10^{16} ions/cm ²	159
Figure 72. Experimental and simulated RBS spectra after irradiation at 180°C and fluence of 8×10^{16} ions/cm ²	160
Figure 73. Experimental and simulated RBS spectra after irradiation with 400keV Ar and fluence of 6×10^{16} ions/cm ²	161
Figure 74. Experimental and simulated RBS spectra after irradiation with 400keV Ar and fluence of 8×10^{16} ions/cm ²	162
Figure 75. Experimental and simulated RBS spectra of an as-deposited ~ 450 Å Sn film on Fe.	163
Figure 76. Experimental and simulated RBS spectra after irradiation with 200keV Ar and fluence of 4×10^{16} ions/cm ²	164
Figure 77. Experimental and simulated RBS spectra after irradiation with 200keV Ar and fluence of 6×10^{16} ions/cm ²	165

List of Tables

Table 1. Lattice parameters of the equilibrium phases present below 600°C in Al-Mo binary system.	19
Table 2. Atomic positions of some intermetallic compounds in Al-Mo system.	21
Table 3. Typical sputter deposition conditions used for the deposition of 1200 Å Mo on Al bilayer film.	59
Table 4. Typical sputter deposition conditions used for the deposition of 6000 Å Mo on Al bilayer film.	60
Table 5. Typical sputter deposition conditions used for the deposition of 330 Å Mo on Al bilayer film for TEM studies.	61
Table 6. Typical sputter deposition conditions used for the deposition of 200 Å Mo/Al multilayer film.	62
Table 7. Results of X-ray line shape analysis of Mo(110) and Al(111) reflections from Mo, Al and Mo/Al bilayer thin films.	77
Table 8. Diffraction data for intermetallics in Al-Mo.	102
Table 9. D ₀ and Q values for diffusion of Mo into Al.	119
Table 10. Simulated composition-depth profile information for a Mo/Al multilayer.	123

1.0 INTRODUCTION

Transition metal films are being used extensively in Integrated Circuits (ICs) as Schottky barriers and as ohmic contacts [1]. One of these transition metals is Molybdenum (Mo), which is deposited as a thin film on silicon to form refractory Molybdenum silicide gates and interconnects in VLSI and VVLSI circuits. Aluminium (Al) thin film stripes are being used as electrode and wiring material in these IC devices. Al/Mo bilayer thin films also find applications in solar energy devices, planar type magnetic sensors and other thin film devices. The Mo thin film layer acts as a diffusion barrier that prevents reactions between the Al electrode and the silicon active layer in such devices. It may also help prevent electromigration failures of the Al thin film stripes, caused by field-assisted Grain Boundary diffusion of Al, by solute-vacancy trapping and intermetallic compound formation [2]. These applications stress the importance of the characterization of Mo/Al bilayer thin films for their preparation, structure, thermal stability and phase transformations.

Currently, there is renewed interest in the production and stabilization of synthetic metallic multilayered superlattice thin films that have a eutectic phase diagram and have different crystal structures [3, 4, 5, 6]. These multilayer films are found to exhibit several interesting properties such as electrical resistivity controlled by layer thickness, a sudden sign change in Tem-

perature Coefficient of Resistivity (TCR) from positive (metallic) to negative (non-metallic) as a function of layer thickness with zero TCR over a wide temperature range at the appropriate layer thickness [7], increased superconducting transition temperature, two-dimensional magnetic behavior, and elastic 'Supermodulus Effects' [8]. Further, Mo/Al multilayer thin films are best suited for BCC/FCC interface coherency studies and interdiffusion studies for very short diffusion distance and time scales. These multilayers, being made of alternating layers of dense high atomic number Mo with the low atomic number Al, may be used as a dispersion element for soft X-rays in X-ray optics, thus producing wavelength selectivity through Bragg diffraction at low angles less than approximately 15°. They can also be used to form complex X-ray interference structures [9].

Formation of amorphous alloys in layered thin films through solid state diffusional reactions or high-energy ion-beam mixing, in general, increases the corrosion and oxidation resistance by promoting the formation of a uniform passive protective film [10]. A comparative study of thermal diffusion and high-energy ion-beam mixing would lead to a better understanding of the mechanisms involved in radiation enhanced diffusion. Ion-beam mixing of the Mo/Al bilayer and multilayer thin films to examine the differences in mixing rates and the efficiency of mixing may help optimize the parameters involved in the fabrication of protective layered thin film coatings, surface-alloyed by ion-beam mixing. Further, Mo/Al layered films are amenable to easy RBS composition profile analysis because the RBS spectral peaks corresponding to Mo and Al are well separated in energy due to the large differences in their atomic densities and atomic numbers.

Considering the theoretical importance and potential applications of Mo/Al bilayer and multilayer thin films, the thesis work presented here concentrates on the fabrication of these films using a conventional radio-frequency (rf-) diode sputter deposition system and their characterization with respect to structure and composition. The films were deposited on glass and Si(100) substrates. The methods used for film characterization were Auger Electron Spectroscopy

(AES), X-ray diffraction, Analytical Electron Microscopy (AEM), and Rutherford Backscattering Spectroscopy (RBS).

The as-deposited Mo/Al bilayer films were annealed at different temperatures in the range of 300-600°C for different lengths of time. The annealed films were examined for composition profile changes due to interdiffusion, intermetallic compound formation and metastable or amorphous phase formations. The lattice diffusivity of Mo in Al thin film and the growth characteristics of intermetallic compounds are presented. Attempts were made to deposit Mo/Al multilayer thin films with different layer thicknesses. Parameters determining the structural quality and composition modulation amplitude of these multilayer films were analysed.

In this thesis, the second chapter reviews relevant literature on sputter deposition technique, the Mo/Al phase diagram and crystal structures of possible intermetallic compounds, and the results of earlier studies on similar BCC/FCC layered thin films. It also briefly reviews the characterization techniques used in the present study. Chapter 3 presents the theory based on which the experimental results obtained using the various techniques were analysed. The various experimental procedures adopted for fabrication and characterization of the Mo/Al layered thin films and for the study of diffusional reactions in them are presented in Chapter 4. The results of these experimental studies are presented in Chapter 5 along with discussions of the results. Conclusions and recommendations for future work are presented in the last Chapter 6. Finally, in the appendices, recommendations are made for improvement of film quality and for obtaining sharper interfaces using rf-magnetron sputtering sources. Results of a few preliminary theoretical calculations to predict the effect of ion-beam mixing with a high-energy Argon ion beam on Mo/Al bilayer thin films are presented. Few experimental RBS analysis results from ion-beam mixing of Tin (Sn) thin films on pure Iron (Fe) substrates are also presented for a qualitative comparison with the theoretical predictions for ion-beam mixing of the Mo/Al films.

2.0 LITERATURE REVIEW

In this chapter, the literature on the fabrication of thin films using sputter deposition technique is first reviewed. Special attention is given to the optimization and control of parameters that affect the quality of the deposited films. Following the above review of sputter deposition technique, a survey of the equilibrium phase diagram of the Mo/Al binary system and the crystal structures of the intermetallic compounds is presented. Data available in the literature on interdiffusion and compound formation for the Mo/Al system are also presented. Further, other similar BCC/FCC metallic layered thin film systems are reviewed. Finally, a brief review of the techniques of characterization of layered thin films is presented. This review concentrates on the techniques (AES, XRD, TEM, SEM, and RBS) used in this research effort.

2.1 Fabrication of Layered Thin Films

Traditionally, films that are less than a few microns thick are considered as thin films. Several methods exist for the deposition of these thin films. Among these methods, the most widely used ones for the preparation of metallic thin films are Glow Discharge Sputter depo-

sition, Chemical Vapor deposition, Ion Beam deposition, Electron Beam Evaporation, and Molecular Beam Epitaxy. Each of these methods has its own advantages and limitations, depending on the material to be deposited and the requirements on the physical properties of the deposited film. One of the major advantages of Glow Discharge Sputtering is that thin films of almost any element in the periodic table can, in principle, be deposited using this technique. Specifically, the radio frequency (rf-) glow discharge sputtering technique, which was first described by Anderson et. al. [11], can be used to deposit thin films of even semi- and non-conductive materials. This is the technique that was used for the fabrication of layered Mo/Al thin films in the research work presented here. Hence, the processes and parameters involved in this sputter deposition technique are reviewed in the following section.

2.1.1 Planar Diode Glow Discharge Sputtering

Because of the importance of thin films in modern technology and the high utility of sputtering technology to fabricate these films, there are several books and critical review articles in the literature about sputtering and the sputter deposition processes. The review presented here pertains specifically to glow discharge inert gas sputter deposition technique using a conventional planar diode source and is derived from a few recent review articles and books on the subjects of sputtering and thin films [12, 13, 14, 15].

A conventional glow discharge planar diode sputtering system has one or more targets (cathodes) and an adjacent substrate mounting table (anode) as depicted in Figure 1 on page 7. A low pressure abnormal negative glow discharge is established between the anode and the cathode(s) by exciting the inert gas (usually pure Argon), using excitation coils. The glow discharge environment is maintained by the application of DC or RF (5-30 MHz) power. Normally, gas pressures ranging from a few millitorr to about 100 mTorr are used. The positive ions in the glow discharge strike the cathode target and remove mainly neutral target atoms by momentum

transfer and these neutral atoms condense on to the substrate to form the thin film. Together with these neutral atoms, secondary electrons and ions, desorbed gases, X-rays, and photons are also produced and all of these can affect the properties of the deposited film. The growing film and the substrate platform are bombarded by the secondary electrons and ions. This is always the case in simple planar diode sputtering because the substrate platform is at a relatively high positive potential (normally 'floating' in the glow discharge) with respect to the target which is connected to a high negative voltage supply. In many instances, a negative bias potential is applied to the substrate platform, so that the growing film is subject to positive ion bombardment. When operated in this way, the system is said to be in 'Bias Sputtering' mode.

For the deposition of layered thin films, multi-target configurations [16] are required so that sequential deposition of two or more materials is possible. A typical multi-source sputter deposition system that can be used for sequential deposition of metals to form layered metallic thin films is shown in Figure 2 on page 8. In such sputter deposition systems, the targets are well separated and the substrate table or hoder moves past the targets. A single layer of appropriate metal gets deposited as the substrates pass by a target. These sputtering systems have the capability to split and share the total available power between the depositing targets in any specific ratio so that deposition rate of each target material can be controlled.

2.1.2 Deposition Parameters and Control

Westwood [12], in his critical review of glow discharge sputtering, analyses the parameters that affect the characteristics of the deposited thin film. The rate of sputtering of the target depends on the flux, type, and energy of the incident sputtering ions and the target material. For a given sputtering gas and target material, the sputtering rate increases with both the energy and the flux of ions produced in the glow discharge. Increase of sputtering rate can be achieved by increasing either the target bias voltage or the ion current density because in a diode discharge, the

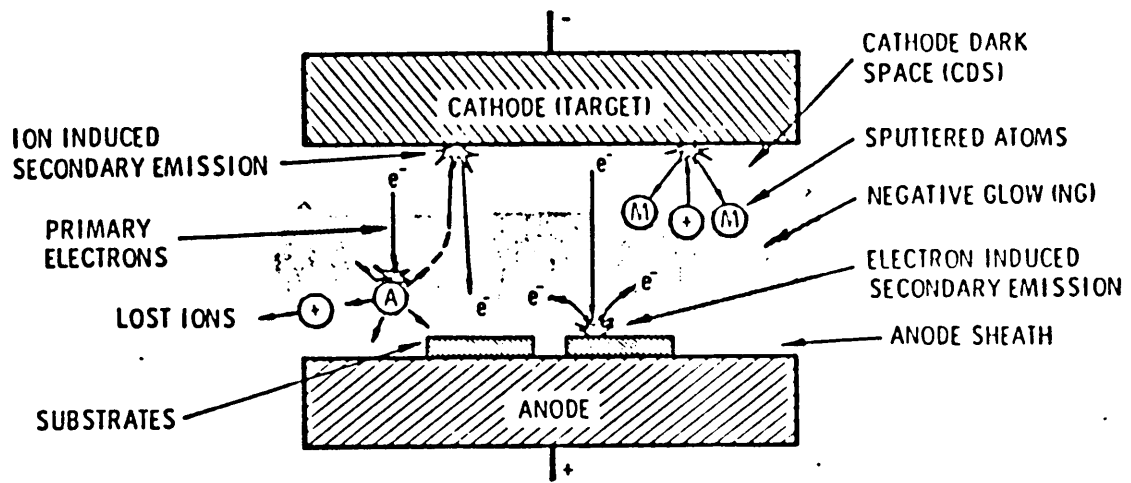


Figure 1. Planar diode source: Schematic representation of a conventional planar diode sputtering source.

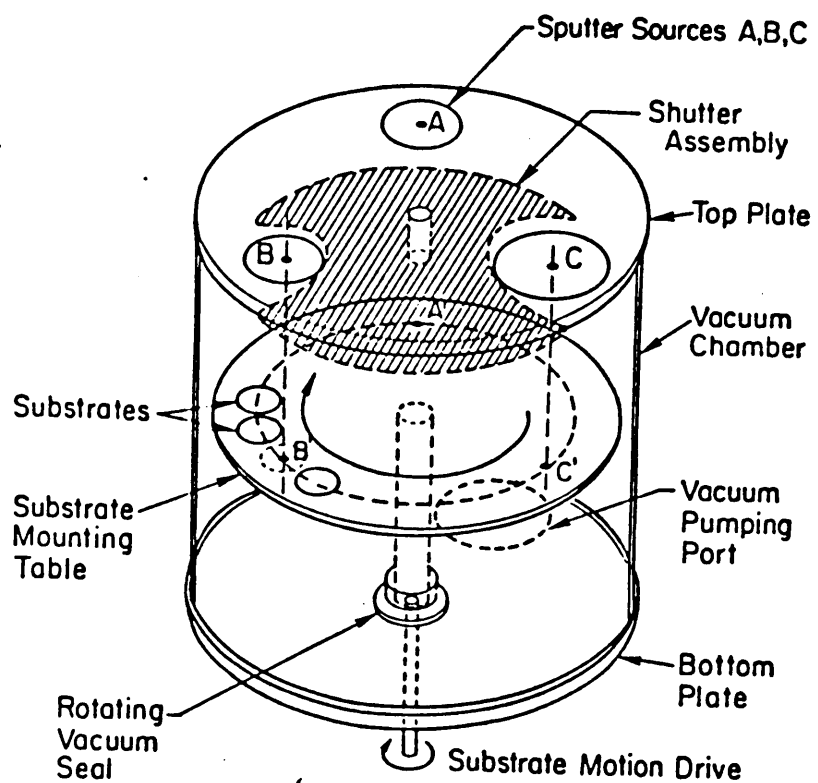


Figure 2. Multi-target deposition system: Schematic representation of a multi-target sputter deposition system.

target bias voltage and the ion current density are interdependent. The maximum value of target bias voltage is determined by the maximum power capacity of the rf- or dc power supply. Thus, the power supplied to a target directly controls the target sputtering rate and consequently the thin film deposition rate.

Another very important parameter that directly determines the sputtering rate and the deposition rate is the inert gas pressure. Increasing the sputtering gas pressure increases the glow discharge current and thus tends to increase the deposition rate. But, this increase in gas pressure also increases the return of the sputtered material back to the target by backscattering; this tends to decrease the deposition rate. Increase in gas pressure also slows down the energetic particles by inelastic collisions so that the energy of particles incident on the substrates is minimized. Further, at higher pressures, self-sputtering may occur due to increased Penning ionization which tends to increase the sputtering rate and consequently the deposition rate. The overall effect of these competing processes as the sputtering gas pressure is varied is that there is a small range of gas pressure at which the deposition rate is maximum. This optimum gas pressure also depends on the system geometry (especially the target-substrate separation distance), the target bias voltage and the sputtering gas used. The effect of sputtering gas pressure on the deposition rate of nickel is depicted in Figure 3 on page 10 [17]. The deposition rate curve in this figure was obtained for a target-substrate separation of 4.5 cm and target voltage of 3000 V. The optimum pressure for this system is at \sim 75 mTorr that yields a current density of \sim 1 mA/cm² and a deposition rate of 360 Å/min. Since the optimum pressure depends on many parameters, it must be determined empirically for each application under fixed conditions of geometry and target voltage. In most cases, this optimum pressure lies between 10-150 mTorr for Argon gas.

It should be recognized that true deposition rate is the difference between the arrival rate and the resputtering rate of the target material at the substrate. The arrival rate is controlled by the control of target sputtering rate. The resputtering of the film deposited at the substrate is controlled by the value of negative bias that the substrates are subjected to. The

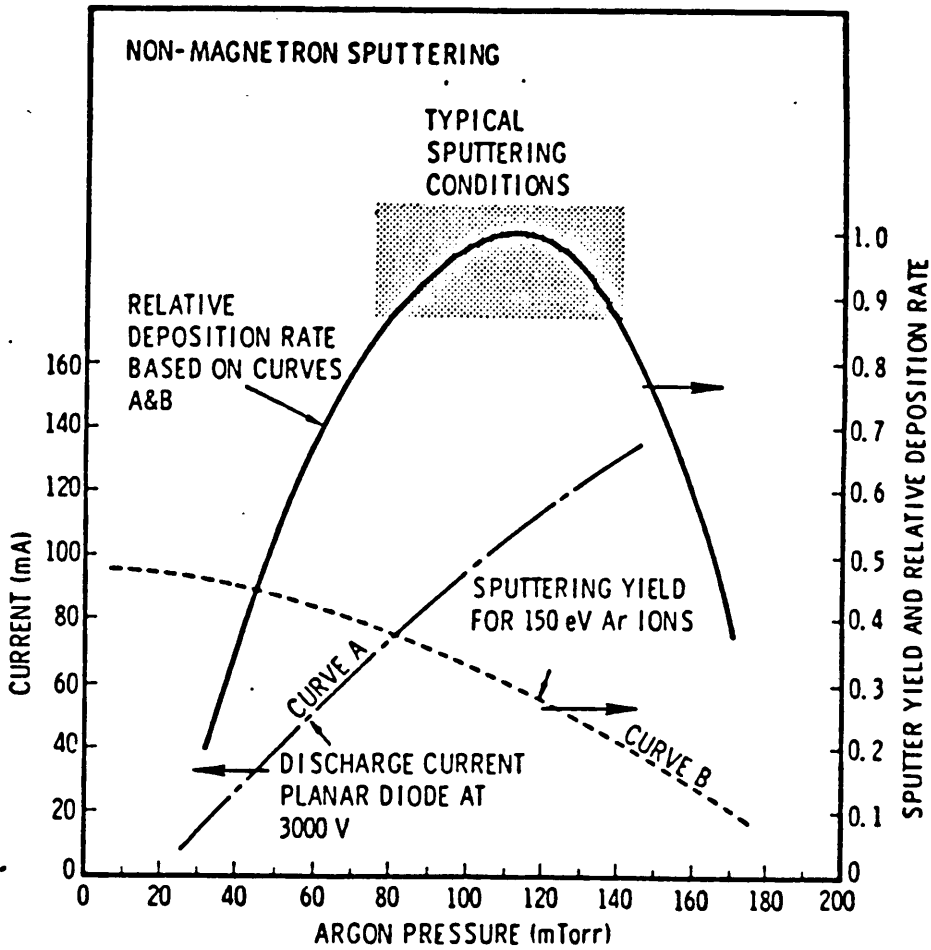


Figure 3. Effect of sputtering gas pressure: Figure depicts the effect of sputtering gas pressure on deposition rate for a conventional diode sputtering source.

substrates in a diode sputtering system are generally left 'floating' (not grounded) at a slight negative bias and hence are always subject to ion bombardment and resputtering. It is generally found that controlled resputtering often improves the physical properties of the deposited film such as film density, grain size, adhesion, and surface morphology [12]. Control of resputtering is achieved by applying a negative substrate bias voltage from an external power source. Usually, a small fraction of the negative bias applied to the target from the main power source is redirected to the substrate holder. Increasing the substrate bias increases the resputtering rate and hence decreases the net deposition rate. However in most cases, the uniformity of deposit and the quality of the film are improved by this. Substrate biasing also increases the substrate temperature considerably and if the bias is high enough, it may lead to an increase in inert gas incorporation in the growing film. Because of these effects, it is generally preferred not to use a high substrate bias. Since substrate bias is very critical for control of film quality, a proper biasing voltage has to be chosen empirically for optimal control of the physical properties of the deposited film. The optimum value of this bias usually depends on the geometry of the system, the film material being deposited, sputtering gas and gas pressure.

In short, for a specific target material, the rate of deposition and the quality of the film are influenced by the following parameters -

- System geometry (target-substrate separation distance)
- Target voltage and power
- Sputtering gas pressure
- Substrate bias voltage
- Substrate temperature (if externally heated or cooled)
- Residual and impurity gases in the system
- Type of substrate and its surface conditions

The effect of substrate temperature and sputtering gas pressure on the morphology of thick metallic sputtered films is schematically represented in Figure 4 on page 13. All the parameters listed above are inter-related and attempts must be made to control the parameters through prior knowledge and experience about the system and through empirical calibration of the system so that films with desired physical properties could be deposited.

2.1.3 Sputter Deposition of Layered Thin Films

Fabrication of bilayer and multilayer thin films by sequential sputter deposition of two or more different materials makes use of sputtering systems with multi-target configurations represented in Figure 2 on page 8. Though the deposition process and the control parameters are the same as discussed in section 2.1.2., the optimization of these parameters is much more difficult and involved. Sometimes, it may not be possible to obtain unique optimum values for the control parameters, especially when sequentially depositing two different materials which exhibit widely different sputtering and resputtering characteristics [12]. The important considerations for obtaining sharp or abrupt interfaces and large coherent composition and structural modulation amplitudes using sputter deposition systems [15] are -

1. Sputter source - deposition surface decoupling
2. Energy distribution of sputtered atoms
3. Geometry of source - substrate configuration.

Since the source is plasma based, plasma-substrate coupling is of primary concern. This coupling is due to the secondary electron bombardment, inert gas ion bombardment, neutral inert gas atom bombardment, and vacuum ultraviolet irradiation of the substrates and it causes substrate heating, enhanced atomic mobility for depositing atoms at the surface of the growing film, inert gas ion implantation, and ion-beam mixing of the deposit surface. One or more

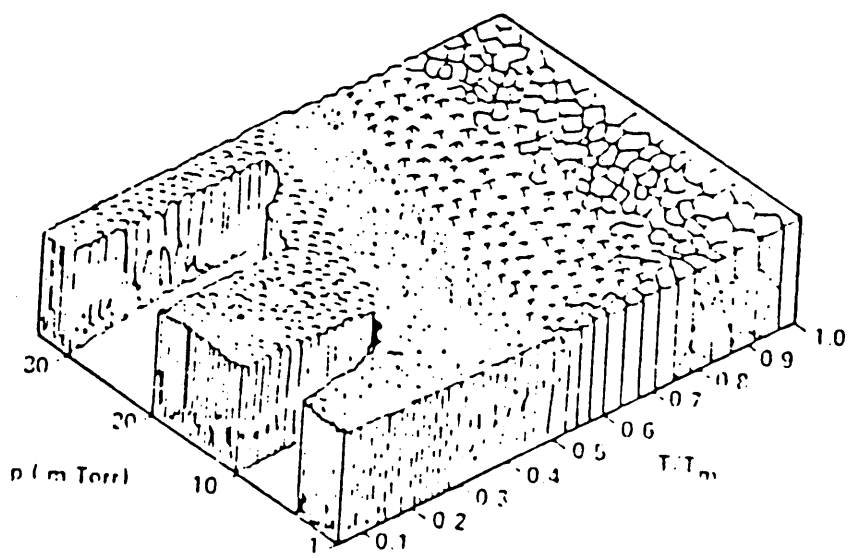


Figure 4. Morphology of sputtered films: Schematic representation of film morphology as a function of sputtering gas pressure and of substrate temperature to bulk melting point ratio [Ref.12].

of these effects lead to the degradation of interface character with respect to sharpness up to a few hundred Angstroms in extent. Unfortunately, due to the inherent nature of conventional diode sources, it is almost impossible to completely decouple the interacting plasma from the substrates. The effect of plasma-substrate coupling on the composition modulation amplitude of a semiconductor multilayer superlattice thin film deposited using a conventional diode sputtering source is illustrated in Figure 5 on page 15 [18]. Increasing the sputtering gas pressure tends to decouple the plasma from the substrate and reduces the effect of plasma-substrate coupling. However, it should be noted that the modulation amplitude was well below 100% at all the indicated sputtering gas pressures and modulation wavelengths. Though such effects have not been reported for the deposition of a metallic multilayer system, one can expect similar effects in metallic systems also. This makes it difficult to fabricate compositionally abrupt interfaces using a diode sputter deposition source. Magnetron sources are capable of completely decoupling the plasma from the substrate and the advantages of magnetron sources over conventional diode sources for deposition of layered thin films are discussed in appendix A.

The energy distribution of sputtered atoms also determines the energy or power deposited by these atoms at the substrate surface or the surface of the growing film that leads to substrate heating. Considerable increase in substrate temperature is possible when the substrate is thermally isolated. To minimize this effect, the sputtering system may be operated at relatively higher sputtering gas pressures so as to thermalize sputtered atoms by gas scattering.

The angle of incidence of the depositing atoms on to the substrate together with the roughness of the substrate determines the uniformity of layer formation and the in-plane or lateral coherence of the deposited layered films. Sputter sources are 'distributed' in nature and provide deposition at many different angles of incidence at the substrate. Also, the motion of the substrates past the targets in a multi-target configuration results in deposition at nearly all angles of incidence. These two effects tend to minimize the role of surface roughness of the substrate in

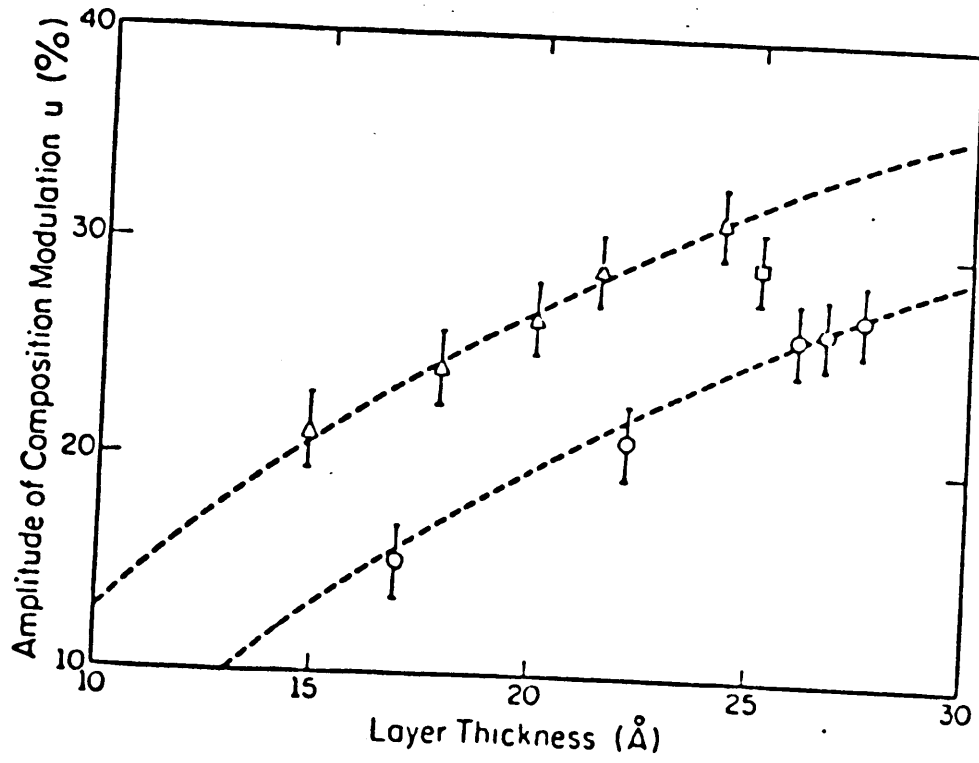


Figure 5. Composition modulation amplitude obtained with a diode source: InSb-GaSb multilayers-
 $\Delta, 15\text{mTorr}; \bigcirc, 1\text{mTorr}; \square, 3\text{mTorr}$ [Ref.18].

producing films of non-uniform thickness [12]. However, for obtaining good lateral coherency, the substrate surface should be as atomically smooth as possible.

2.2 *The Mo/Al System*

2.2.1 Phase Diagram and Crystal Structures

The most recent equilibrium phase diagram [19] of the Al-Mo binary system is shown in Figure 6 on page 17. The diagram was assessed based on earlier work by other investigators and was obtained by thermodynamic modelling. This diagram shows that there are at least nine intermetallic phases in the Al-Mo system. Since diffusion and phase formation studies of the sputter deposited Mo/Al bilayer thin films in the present investigation were carried out at temperatures between 300°C and 600°C, only those intermetallics that form below 600°C are of immediate concern. These compounds are, Al_{12}Mo (BCC), Al_6Mo (Unknown structure; possibly Monoclinic), Al_5Mo (Hexagonal), $\text{Al}_{22}\text{Mo}_5$, or $\text{Al}_{17}\text{Mo}_4$ (Unknown structure), Al_4Mo (C - centered Monoclinic), Al_8Mo_3 (C - centered Monoclinic), and AlMo_3 (Cubic - A15). Of these, AlMo_3 and Al_8Mo_3 exhibit some amount of solid solubility. The other intermetallics do not show any significant solid solubility. According to Kamei et. al.[20], the solubility of Mo in Al at 660°C (approximately the melting point of Al) is probably much less than 0.06 atomic %. At lower temperatures, solubility decreases rapidly such that at 400°C it is probably less than 0.01 atomic %. The solubility of Al in Mo is not clear at low temperatures from the diagram. The given solid solubility curve is based on lattice parametric work [21]. It can be seen that an extrapolation of the solubility curve to lower temperatures (< 600°C) would indicate only small amounts of Al solid solubility in Mo (< 0.3 atomic %).

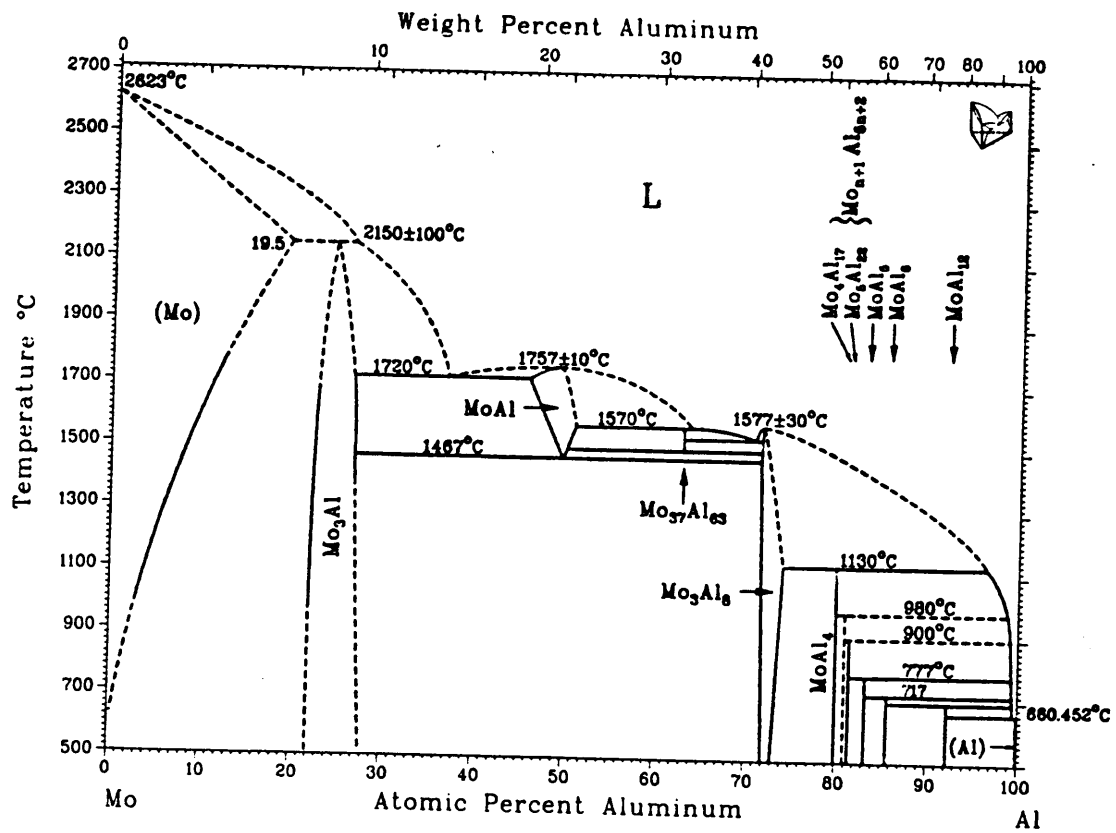


Figure 6. Al-Mo Equilibrium binary phase diagram [Ref.19].

The crystal structures of the equilibrium phases present at temperatures below 600°C for the Al-Mo system are -

1. Face centered cubic Al [22]
2. Body centered cubic Al_{12}Mo with space group Im3 [23]
3. Al_6Mo with unknown crystal structure that is possibly Monoclinic [23]
4. Hexagonal Al_5Mo with space group P6₃ [25]
5. $\text{Al}_{22}\text{Mo}_5$ or $\text{Al}_{17}\text{Mo}_4$ with unknown crystal structure [19]
6. C - centered monoclinic Al_4Mo with space group Cm [24]
7. C - centered monoclinic Al_8Mo_3 with space group C2/m [25, 26, 27]
8. Cubic AlMo_3 which is of the type A15 with space group Pm3n [28]
9. Body centered cubic Mo [29]

The lattice parameters of the above phases are listed in Table 1 on page 19. The atomic positions for some of the intermetallic compounds listed above are given in Table 2 on page 21.

2.2.2 Diffusion and Reactions

Thin film diffusion and reaction kinetics differ from that of bulk specimens. The factors that are responsible for this difference are critically reviewed by Balluffi and Blakely [30]. In most cases of thin film reactions, many of the factors discussed by them such as the presence of large amounts of short-circuit diffusion paths, large bi-axial stresses, and steep concentration gradients tend to be actively controlling the diffusion and growth kinetics. Because of these factors, generally one can expect 'interface controlled' kinetics to dominate thin film diffusion reactions. Further, because of the steep concentration gradients, it is more difficult for the interface reactions to maintain local equilibrium at reaction boundaries. This may lead to the formation of non-equilibrium metastable phases in thin films. Interface controlled reactions exhibit linear growth

Table 1. Lattice parameters of the equilibrium phases present below 600°C in Al-Mo binary system.

Phases	Lattice Parameters (\AA)	Cell Angles
Al	FCC $a = 3.1469$	
Al_{12}Mo	Cubic $a = 7.5815$	
Al_5Mo	Hexagonal $a = 4.89; c = 8.80$	
Al_4Mo	Monoclinic $a = 5.255; b = 17.768;$ $c = 5.225$	$\beta = 100.7^\circ$
Al_8Mo_3	Monoclinic $a = 9.208; b = 3.6378;$ $c = 10.065$	$\beta = 100.78^\circ$
AlMo_3	Cubic $a = 4.950$	
Mo	BCC $a = 3.1469$	

Atomic Positions of the Al₁₂Mo Phase

Space group T_h^5 - Im3

$$(0,0,0; \frac{1}{2}, \frac{1}{2}, \frac{1}{2}) +$$

24 Al in g (0,y,z; z,0,y; y,z,0; 0, \bar{y} , \bar{z} ; \bar{z} , 0, \bar{y} ; \bar{y} , \bar{z} , 0; \bar{z} , 0, y; y, \bar{z} , 0; 0, \bar{y} , z; z, 0, \bar{y} ; \bar{y} , z, 0) with

$$y = 0.1854; z = 0.3083$$

2 Mo in a (0,0,0)

Atomic Positions of the Al₄Mo Phase

Space group C_s^3 – Cm

$$(0,0,0; \frac{1}{2},\frac{1}{2},0) +$$

2 Al in a (x,0,z) with x = 0.1611; z = 0.5103

2 Al in a (x,0,z) with x = 0.5117; z = 0.1481

4 Al in b $(x,y,z; x,\bar{y},z)$ with $x = 0.6753$; $y = 0.0767$; $z = 0.6951$

4 Al in b $(x,y,z; x,\bar{y},z)$ with $x = 0.8322$; $y = 0.1180$; $z = 0.2246$

4 Al in b ($x,y,z; x,\bar{y},z$) with $x = 0.2067; y = 0.1218; z = 0.8267$

4 Al in b ($x,y,z; x,\bar{y},z$) with $x = 0.7087; y = 0.2351; z = 0.6057$

4 Al in b $(x,y,z; x,\bar{y},z)$ with $x = 0.5414$; $y = 0.25$

2 Mo in a (x,0,z) with x = 0.0000; z = 0.0000

4 Mo in b $(x,y,z; x,\bar{y},z)$ with $x = 0.3514$; $y = 0.5$

Table 2. Atomic positions of some intermetallic compounds in Al-Mo system.

Atomic Positions of the Al_8Mo_3 Phase

Space group C_{2h}^3 - C2/m

4 Al in i	(x,0,z; \bar{x} , 0, \bar{z}) with x = 0.272 z = 0.906
4 Al in i	(x,0,z; \bar{x} , 0, \bar{z}) with x = 0.460 z = 0.178
4 Al in i	(x,0,z; \bar{x} , 0, \bar{z}) with x = 0.187 z = 0.279
4 Al in i	(x,0,z; \bar{x} , 0, \bar{z}) with x = 0.367 z = 0.542
2 Mo in a	(0,0,0)
4 Mo in i	(x,0,z; \bar{x} , 0, \bar{z}) with x = 0.094 z = 0.660

Atomic Positions of the AlMo_3 Phase

Space group O_h^3 - Pm3n

6 Mo in c	($\frac{1}{4}, 0, \frac{1}{2}; \frac{1}{2}, \frac{1}{4}, 0; 0, \frac{1}{2}, \frac{1}{4}; \frac{1}{4}, 0, \frac{1}{2}; \frac{1}{2}, \frac{1}{4}, 0; 0, \frac{1}{2}, \frac{1}{4}$)
2 Al in a	(0,0,0; $\frac{1}{2}, \frac{1}{2}, \frac{1}{2}$)

rates. If short-circuit diffusion controls the thin film reactions, the new phases being formed might be nucleated along these short-circuit paths and may grow into irregular shapes with complex growth kinetics. The stress in thin films generally tend to assist lattice and grain boundary diffusion.

Reviewing specifically the diffusion data available for Al-Mo system, it was found that very few studies were performed on this system so far. Nguyen van Chi [31] studied the diffusion of Cr, Mo, Ti, V, and W in Al using electron microscopy techniques in the temperature range of 560 - 655°C. He concluded that the diffusion coefficients near the melting point of Al were greatly influenced by the number of d-electrons involved and also obtained a linear relation between the results and the number of d-electrons of the diffusing element. He obtained a value of $D_0 \cong 18 \text{ cm}^2/\text{sec}$. for the pre-exponent factor and $Q \cong 60 \pm 4 \text{ kcals}$ for the activation energy for diffusion of Mo in Al for a composition of 0.2 to 0.3 atomic % Mo in Al in the temperature range of 625 - 655 °C. Rexer [32] studied the phase equilibria in Al-Mo system at temperatures above 1400°C. He obtained the relation

$$C_{\max} = 2.11 \times \exp(-5400/T)$$

for the maximum solubility of Al in Mo (C_{\max}), where T is the temperature in °K. However, these studies were done on bulk samples.

Recently, reactions in Al/Mo bilayer thin films were briefly studied by Kitada and Shimizu [33] using Auger depth profiling technique and TEM. In their bilayer films, Al was deposited on Mo, on various substrates using a conventional electron beam evaporation system. The thickness of the layers were $\cong 500 \text{ \AA}$ each. These investigators used TEM techniques to study the microstructure of the as-deposited and annealed films. Intermetallic compounds formed were identified using electron diffraction patterns. They could find compounds Al_{12}Mo and AlMo_3 being formed in films that were annealed between 300 to 500°C. However, they could not clarify the other phases that might have formed due to the complicated nature of the electron

diffraction patterns. They also could not use the composition profiles obtained by Auger depth profiling to determine the interdiffusion and intermetallic compound growth characteristics. This was because of an unknown amount of profile shift caused by the analyzing method itself. Study of electrical resistivity changes with annealing time led them to believe that the compound formation kinetics was parabolic and hence was diffusion controlled. It was also found that a reduction in annealing vacuum caused Mo to diffuse to the surface and get oxidized. The Mo oxide was reported to be amorphous.

2.3 Other BCC/FCC Metallic Layered Thin Films

Several other bilayer and multilayer thin film systems have been investigated so far in which alternating BCC/FCC metallic layers were deposited. One such bilayer system that is similar to Mo/Al system is the Cr/Al system. Like the Mo/Al system, Cr/Al system also exhibits several equilibrium intermetallic compounds. Interdiffusion of Al and Cr in a bilayer thin film was investigated by Chamberlain [34] using AES combined with Argon ion-beam sputter depth profiling. Though several intermetallics were possible, only Al_7Cr was observed at the interface of the isothermally annealed samples. The growth rate of this compound was found to be parabolic and the growth rate constant was estimated. The chemical interdiffusion coefficient D was calculated and the lattice diffusivity of Cr in Al was estimated. This bilayer film was deposited by electron beam evaporation technique.

The multilayer system involving Nb/Cu [3,35] was studied extensively for structural and physical properties. Characterization of the films using X-ray diffraction revealed one dimensional coherence with [110] and [111] texture in Nb and Cu layers respectively. These two elements are not mutually soluble and hence there is no interdiffusion. The quality of the films

however deteriorated at smaller layer thicknesses and the grain size was also found to decrease. The as-deposited interfaces were found to be quite sharp at layer thickness $> 20 \text{ \AA}$. No evidence was found for the presence of coherency strains.

The Nb/Al system was investigated by McWhan et. al. [5]. This system showed orthorhombic distortions of the Nb layers indicating the presence of anisotropic coherency strains. Nb seemed to have contracted and Al expanded. The composition modulation wave was approximately trapizoidal and the interfaces were $\cong 11 \text{ \AA}$ thick. The interdiffusion was found to be asymmetric with Al diffusing into Nb.

Another investigation was on the Mo/Ni [4] multilayer thin film system. The Mo/Ni multilayer films also showed [110] and [111] preferred orientation respectively. Several substrates were used to find out which substrates would give near-epitaxial growth. Anomalies in lattice spacings, elastic modulii, and electrical resistivity as a function of modulation wavelength were observed. These anomalies were attributed to the strains in the Ni lattice. Interdiffusion was found to be negligible in the as-deposited films. These films were polycrystalline with a high degree of texture.

It should be noted here that all the above multilayer thin films were deposited using magnetron source sputter deposition systems and not a conventional diode sputtering system which was used in the present research effort. The interfaces in the cases cited above were almost atomically sharp and the layering was also found to be very uniform and even coherent in some cases, down to layer thicknesses of 10-20 \AA .

2.4 Techniques of Characterization of Layered Thin Films

Several destructive and non-destructive techniques are available for characterizing layered thin films for the structure, texture, interface character, uniform and non-uniform microstrains, surface condition, composition profile, intermixing of layers due to diffusion and/or ion-beam mixing and possible new phase or compound formations. Some of the popular techniques are X-Ray Diffraction (XRD), Auger Electron Spectroscopy (AES), X-ray Photoelectron Spectroscopy (XPS), Rutherford Backscattering Spectroscopy (RBS), Secondary Ion Mass Spectrometry (SIMS), Analytical Electron Microscopy (AEM), High Energy Ion Channelling, Conversion Electron Mossbauer Scattering (CEMS), and Ion Scattering Spectrometry (ISS). Of these techniques, AES, XPS, SIMS, and ISS need to be combined with sputter-etching of the surface by an ion-beam to obtain composition-depth profiles and hence are considered destructive to various degrees. Since the present study of layered Mo/Al thin films utilized four of these techniques, namely, AES with Argon ion-beam sputter-etch profiling, X-ray diffraction, RBS, and AEM, these four techniques are briefly reviewed here.

2.4.1 AES with Argon Ion-beam Sputter-etch Profiling

AES is based on the Auger effect whereby an incoming electron with sufficient energy ionizes an atom by removing a core electron and the excited atom relaxes to ground state with the emission of a kinetic electron called the Auger electron. Energy analysis of these Auger electrons yields elemental identification of the surface atoms within the sampling depth which is roughly 5-20 Å. This sampling depth depends slightly on the material being analyzed. Because of the small sampling depth, AES is now a very popular technique for surface analysis [36]. Good quantitative analysis using AES requires careful calibration as well as sufficient knowledge of the

influencing parameters such as the current density, ionization cross-section, Auger transition probability, analyzer transmission, contribution of backscattered electrons and surface topography. Any element in the periodic table starting from Lithium could be detected with 0.001 to 0.01 atomic fraction limit of detection. Primarily, quantitative AES analysis is done by comparison with standard measurements, (the measured Auger signal of a specimen with unknown composition is compared with the Auger signal of a standard with known elemental concentration) or by the use of elemental sensitivity factors. The latter method is very useful in that it does not require any standard measurements. If all Auger signals I_i of the elements representing the specimen are known, the concentration of the element A in the sampling volume is given by [37]

$$C_A = \frac{(I_A/K_A)}{\sum(I_i/K_i)}$$

where K_i is the relative sensitivity factor of element i. In this method, however, the matrix dependence of sensitivity factors and the influence of surface topography are ignored. These two effects may be important when AES is combined with sputter-etch profiling for the determination of the composition profile in layered thin films. Despite the uncertainties in using the relative sensitivity factors of pure element standards, quantitative analysis can be carried out with an accuracy of 10 - 30 atomic %.

Composition-depth profiling with AES can be done either by removing surface layers by ion-beam sputter-etching with simultaneous surface elemental analysis [38] or by using tapered sectioning methods. When adopting the former method for analysis of a multicomponent system, one should always be aware of the possibility of 'selective sputtering' which may alter the very surface composition of the system that is being analyzed [39]. While sputter-etching solid solutions or compounds, steady-state sputtering conditions are reached quickly after removal of a layer comparable to the penetration depth of the primary ions. However, when a multi-phase system is sputter-etched, steady-state conditions will be reached only after the removal of a layer with a thickness of several grain diameters which is in general in the micron range. This may lead

to severe roughening of the surface and an altered surface topography, and hence an altered surface concentration as measured by AES [40]. This tends to alter the overall composition profile obtained. A study of Al-Au, Al-Fe, Al-Ni, and Al-Cr compounds [40, 41] under 2 keV Argon ion-beam sputter-etching showed depletion in Al, which is always the lighter and low sputtering-yield component. The factor that determines the enrichment of a component during the sputter-etching of a multi-component system seems to be the recoil energy density deposited at the surface from the collision cascade created by the impinging ion. It is experimentally observed [40] that for alloys with quite different recoil energy densities of the constituents, collision cascade effects generally play the dominant role and the enrichment of the heavier component occurs. One may expect to find these effects when the Mo/Al layered films are subjected to sputter-etch composition-depth profiling with AES. Also, the depth resolution in this case is affected by microtopography of the sputter-etched surface and by ion bombardment damage or ion-beam mixing. Ion bombardment 'knock-on' causes motion of the atoms in the sample so that a sharp compositional interface is homogenized to a certain extent by the momentum of the incident particles. Because of these topographical changes and ion-beam damage effects, sputter-etch Auger depth profiling method is not suitable for layered films in which the layer thickness is less than approximately 100 Å. Higher energies of sputter-etching ion-beam would increase this limiting layer thickness to larger values.

2.4.2 X-Ray Diffraction

X-ray diffraction techniques are well suited for studying thin film systems because they are non-destructive and provide relatively high resolution over the small dimensions of thin films. Techniques of analysis have been developed for analyzing the integrated intensities and shapes of the X-ray diffraction peaks [42, 43]. These analyses give the thickness and orientation of the phases present in the thin film. Any changes in thickness can be directly related to the growth kinetics of the phases being formed as a result of thin film reactions. New phases could be easily

identified in most cases provided they are crystalline and give rise to specific diffraction patterns. The dispersion status of the growing phases can also be determined using diffraction peak analysis. X-ray peak positions and peak shifts indicate changes in the average lattice spacing of the corresponding phases as a result of composition changes and stresses in the thin film. From the diffraction peak width and shape, information about the subgrain particle size and non-uniform root-mean-squared microstrain can be obtained. An improved Fourier analysis method based on the Warren and Averbach [44, 45] method of diffraction line shape analysis was developed by Smith and Houska [46]. Computer programs are available to do routine line shape analysis on the diffraction data to extract the above information.

X-ray diffraction technique for monitoring solid-state diffusion in thin film systems has also been developed well [47]. The technique is based on the dependence of diffracted intensity on the lattice parameter gradient which in turn depends on the composition profile in the sample. Computer programs are available to simulate the diffracted intensity band for a given composition profile. The simulated band is adjusted to fit the experimental intensity band by changing the composition profile. From the composition profiles obtained at different temperatures and times, diffusion data for the system can be obtained.

Analysis of multilayer thin films for structural information is most easily done with X-ray diffraction. Simple reflection geometry is enough to make the measurements so that the thin film need not be removed from the substrate. Composition and structural modulations perpendicular to the layers can be studied on a standard diffractometer. However, structural information parallel to the layers including texture and interface coherency can be studied only when the X-ray scans are made in general directions in reciprocal space. The positions and line shapes of the Bragg reflections of the average lattice and of the surrounding 'satellite' reflections arising from the layering are used to calculate the average lattice constants and the average modulation wavelength. Fluctuations in average lattice constant and modulation wavelength resulting from composition gradients and loss of coherence can also be measured [48]. The integrated intensities of the re-

flections are used for obtaining the composition and strain wave profiles. Interdiffusion and mixing between layers causes the amplitude of the modulation to decrease, which is reflected in the intensities and positions of the satellite peaks and is easily measured in most cases. Low-angle (satellites of (000) reflection) diffraction peaks around the main beam arise due to the composition wave resulting from the layering and are observable only when the thickness of the individual layers is ≤ 60 Å depending on the wavelength of the X-rays used. These low-angle peaks are insensitive to strain modulations and are directly related to the structure factor modulation which in turn is directly related to composition modulation. Hence, they make it possible to monitor diffusion even in amorphous multilayer thin film systems [49].

2.4.3 Analytical Electron Microscopy

The power of the electron microscope in characterizing layered thin films lies in it being able to give real space images of the layering and to detect various kinds of defects in the films. Electron diffraction techniques could be utilized for the identification of various phases that might be present and their crystal structures. It is well known that for all Transmission Electron Microscopy (TEM) studies, thin specimens usually < 1 μm are required. It is relatively easier to prepare specimens thin enough to view under TEM by depositing the thin films on either electron transparent carbon coated copper grids or easily dissolvable substrates such as cloven single crystal NaCl. However, layered thin films are generally deposited on the surface of a thick substrate and hence require thinning. Also, the most revealing mode of thinning for layered thin films is perpendicular to the direction of layering. Ion-milling technique is generally used for obtaining thin cross-sectional samples so that any differential thinning effects can be avoided. However, ion-milling itself may introduce unwanted defects into the metallic layers due to ion-beam induced damage. It may also induce amorphization due to ion-beam mixing and give rise to misleading results [50]. So, if differential thinning could be avoided, one should always resort to chemical and electrochemical

thinning techniques which are associated with less damage. There are several modes of contrast available through which layered structures could be revealed in TEM. Some of them are : crystallographic contrast, absorption contrast, structure factor amplitude contrast, strain contrast, and phase contrast. A critical review of the use of TEM for the analysis and imaging of layered thin films is presented by Gibson [50].

The surface morphology of thin films can be studied using the scanning facility of an AEM or a STEM. Surface micro-topography is an important feature that in many instances indicates the quality of the film. It may also reflect the interface sharpness one can expect in layered films. It is important to estimate surface roughness because it plays a vital role in determining the results of other analytical techniques such as AES, RBS etc. Reactions in layered films may lead to the formation of compounds which alter the surface structure due to cracking or blistering of the film. Formation of oxides on the surface and affinity for oxygen may influence the interdiffusion rate of layered structures [33]. Scanning images obtained with secondary electron detector and backscattered electron detector would reveal information about the morphology of the surface and subsurface of the films. This information in many cases turns out to be important for assessing the quality of the thin films.

2.4.4 Rutherford Backscattering Spectroscopy

This is an analytical method which involves bombardment of the thin film sample with very high energy (0.5 to 3.0 MeV), low mass ions (usually H^+ , He^+ , or He^{++}) which penetrate into the sample [51]. The elemental identification of the sample constituents in RBS is derived from the energy distribution of the backscattered projectile ions. Composition information is obtained from depths upto 1 μm into the sample, depending on the energy of the incident ion-beam. The energy spectrum of the backscattered projectiles contains both depth and composition

information because the incident ions lose energy to the outer shell electrons of the target atoms as the projectile passes through the sample before and after the binary collision with a target atom. Separation of depth information from the composition information is easily done through prior knowledge of the sample constituents or by changing the angle of incidence of the projectile ion-beam. The sensitivity of RBS technique depends on the atomic mass of the element being analyzed and the atomic mass of the matrix it is in. High mass element analysis in a low mass matrix would exhibit higher sensitivity. The influence of the incident ion-beam radiation on most metallic target materials is negligible within the sampling depth. A spatial resolution of $\cong 1 \mu\text{m}$ and a depth resolution of about 200 Å are possible with RBS technique. However, mass resolution is poor and it is hard to resolve high mass elements that are closer than 10 amu in mass. So, RBS method is best suited for layered thin films in which the two layered materials are well separated in atomic mass. Such a separation does exist in Mo/Al layered thin films and RBS technique is ideally suited for composition-depth profile analysis of this system. RBS technique has been applied to study the effect of ion-implantation and radiation enhanced diffusion of Tin into Iron [52]. In fact, as an example of another thin film system, experimental RBS spectra obtained from Argon ion-beam mixed Sn film on pure Fe substrate [53] were analyzed by the author to obtain Sn composition profiles. A software package called RUMP [54, 55] was used for the analysis of the RBS spectra and the results of the analysis are presented in appendix C.

3.0 THEORY

The theoretical basis for the equations and expressions that were used for interpreting the experimental results obtained from the various thin film characterization techniques and for diffusion analysis are presented in the following sections.

3.1 Sputter-etch Composition-Depth Profiling with AES

The technique of sputter-etching using an energetic Argon ion beam in combination with AES elemental analysis (Auger composition-depth profiling) has been applied successfully in the past for obtaining composition versus depth profiles for bilayer [34, 56] and multilayer [57] thin films. For reasons of depth resolution and ion-beam mixing effects, Auger depth profiling technique is applicable only for layered films whose layer thicknesses are in general greater than 100 Å. Using the Auger depth profiling technique, one obtains a profile of Auger Peak to Peak Heights (APPH) of the elements of interest in the Auger derivative spectrum, as a function of the sputter-etch time as raw data. In order to extract composition-depth profiles from this raw

data, it is necessary to convert the sputter-etch time to depth and the APPH signals to elemental concentrations appropriately.

For proper conversion of sputter-etch time to depth information, an exact expression for the sputter-etch rate is required. Such an expression should take into account effects of the differences in sputtering yields and atomic volumes of the layer constituents on etch rate. Chamberlain and Lehoczky [56] have derived an expression for the alloy sputtering rate which includes both the above effects. The derivation of this expression was based on the following three assumptions.

1. The atoms are sputtered off only from the outermost atomic plane of the film
2. The sputtering rate of a constituent is proportional to the surface coverage or surface concentration of that constituent
3. The sputtering yield of each of the constituent is equal to the value of pure material. (i.e., the Mo and Al sputtering yields are equal to the pure metal values.)

Along the lines of Ref.56, the following equations were developed for the etch-rate and concentrations of Mo/Al layered films.

The active surface coverage $\Theta_{Mo}(t)$ of element Mo after an etch time t is

$$\Theta_{Mo}(t) = \frac{(A_{Mo}(t) / S_{Mo})}{(A_{Mo}(t) / S_{Mo}) + (A_{Al}(t) / S_{Al})} \quad (1)$$

and for Aluminum surface coverage Θ_{Al} ,

$$\Theta_{Al}(t) = \frac{(A_{Al}(t) / S_{Al})}{(A_{Mo}(t) / S_{Mo}) + (A_{Al}(t) / S_{Al})} \quad (2)$$

where,

$A_{Mo}(t)$ = Measured APPH in Auger derivative spectrum of Mo (186 eV) Auger line

$A_{Al}(t)$ = Measured APPH in Auger derivative spectrum of Al (68 eV) Auger line

S_{Mo} = Relative Auger Sensitivity factor for Mo

S_{Al} = Relative Auger Sensitivity factor for Al

To obtain the sputtering rate of the alloy in etching time t , one must equate the total volume of the sputtered atoms to the volume of the thin film sample removed in a short time t . This yields the equation

$$\dot{y}(t) = v^+ \left[\frac{M_{Mo}}{\rho_{Mo}N} \gamma_{Mo} \Theta_{Mo}(t) + \frac{M_{Al}}{\rho_{Al}N} \gamma_{Al} \Theta_{Al}(t) \right] \quad (3)$$

where,

$\dot{y}(t)$ = The alloy sputtering rate in nm/sec at time t

v^+ = The Ar^+ ion flux in ions/(cm^2 sec)

M_{Mo} = Molecular weight of Mo

M_{Al} = Molecular weight of Al

ρ_{Mo} = Mass density of Mo

ρ_{Al} = Mass density of Al

N = Avogadro's number

γ_{Mo} = Sputtering yield for pure Mo

γ_{Al} = Sputtering yield for pure Al

With the substitution of equation (1) and (2) in (3), equation (3) can be rewritten in terms of the experimentally measured sputter-etch rates for pure metals as

$$\dot{y}(t) = I^+ \frac{(R_{Mo}A_{Mo}(t) / S_{Mo}) + (R_{Al}A_{Al}(t) / S_{Al})}{(A_{Mo}(t) / S_{Mo}) + (A_{Al}(t) / S_{Al})} \quad (4)$$

where,

I^+ = Ar^+ ion beam current in μA

R_{Mo} = Experimentally measured etch rate for pure Mo film normalized to a $1.0\mu A$ current

R_{Al} = Experimentally measured etch rate for pure Al film normalized to a $1.0\mu A$ current

Integration of Equation (4) from $t = 0$ to $t = t'$ gives the depth $y(t')$ perpendicular to the specimen surface at sputtering time t' . Hence, the sputter-etch time scale can be converted to depth scale. If one further assumes that the top altered layer is close to its steady state composition, the following expressions for bulk concentrations of Mo and Al can be easily obtained from equations (1) and (2).

$$C_{Mo}(t) = \frac{(A_{Mo}(t) / S_{Mo})}{(A_{Mo}(t) / S_{Mo}) + R(A_{Al}(t) / S_{Al})} \quad (5)$$

and

$$C_{Al}(t) = \frac{(A_{Al}(t) / S_{Al})}{(A_{Mo}(t) / S_{Mo})(1/R) + (A_{Al}(t) / S_{Al})} \quad (6)$$

where

$$R = \frac{\rho_{Mo} R_{Al} M_{Al}}{\rho_{Al} R_{Mo} M_{Mo}} \quad (7)$$

The factor R is introduced as a correction factor for differences in atomic volumes of Mo and Al. It must be noted here that these bulk concentrations are values averaged over the Auger excitation spot which is approximately the size of the electron beam of the AES probe.

3.2 X-Ray Diffraction

Brief descriptions of the least-squares analysis of X-ray diffraction line shapes for assessing non-uniform strain and subgrain size parameters of sputtered thin films are presented below. Following this, X-ray diffraction theory for ideal multilayer thin films is surveyed.

3.2.1 X-Ray Line Shape Analysis

A simplified version of X-ray diffraction line shape analysis based on the Warren and Averbach [44] method was developed by Houska and Smith [46] with relevant computer programs to perform routine line shape analysis of diffraction profiles. A brief review of the development of theoretical intensity expressions used in this line shape analysis program [46] is presented below. The computer program LSA is used to determine the instrumental parameters first. Then, the same program is used to fit the theoretical intensity expression to the experimental data to yield the particle size and two strain parameters. The two strain parameters are then used for determining the total mean square strain. The LSA program makes use of a non-linear least squares analysis that fits the experimental data to the theoretical function given below by minimizing the sum of the squares.

The intensity profile of a x-ray diffraction peak with instrumental, particle size, and strain broadening can be expressed by the Fourier series

$$P'(h_3) = Y_0 \left\{ 1 + 2 \sum_{n=1}^{\infty} A_n \cos[2\pi n(h_3 - h_3' \ell)] \right\} \quad (8)$$

where h_3 is the scattering vector in reciprocal space, $h_3 = 2 < d > \sin\theta/\lambda$. With a transformation to orthorhombic axes, reflections considered are of the type (00ℓ) . $< d >$ is the interplanar spacings for the (00ℓ) planes. Y_0 is a scaling parameter considered constant for a reflection. Effect of peak shift caused by uniform strain in the sample is removed by translating the origin of the h_3 axis to the peak maximum through $h_3' \ell$. In the case of line profiles obtained from thin films, the Fourier coefficient A_n can be represented by an equivalent product of several coefficients as

$$A_n = [A_C^I]^n [A_G^I]^{n^2} A_n^S [A_I^D]^n [A_I^U]^{n^2} \quad (9)$$

where,

$[A_C^I]^n$ = Instrumental coefficient with Cauchy profile

$[A_G^I]^n$ = Instrumental coefficient with Gaussian profile

A_n^S = Particle size coefficient

$[A_P^C]^n$ = Strain coefficient with Cauchy profile

$[A_P^G]^n$ = Strain coefficient with Gaussian profile.

The Cauchy instrumental broadening coefficient is given by the Fourier transform of the Cauchy function

$$A_C^I = \exp(-2\pi a_\gamma) \quad (10)$$

Similarly, the Gaussian instrumental broadening coefficient is obtained by taking the Fourier transform of Gaussian function, as

$$A_G^I = \exp(-\pi a_\beta^2) \quad (11)$$

The expression for particle size coefficient can be obtained by equating the distribution of column lengths in the subgrains of the sample to the distribution of column lengths in a sphere of correct mean diameter. This yields,

$$A_n^S = 1 - \frac{n}{N_3} + \frac{4}{27} \left[\frac{n}{N_3} \right]^3, \quad n < \frac{3}{2} N_3 \quad (12)$$

and,

$$A_n^S = 0, \quad n \geq \frac{3}{2} N_3 \quad (13)$$

where, N_3 is the average number of cells per column. The two strain coefficients can be expressed in terms of two first neighbor root mean square strain parameters as follows.

$$[A_1^D]^n = \left[\exp(-2\pi^2 \langle \varepsilon_{1D}^2 \rangle / \ell^2) \right]^n, \quad r = \frac{1}{2} \quad (14)$$

and,

$$\left[A_1^U \right]^{n^2} = \left[\exp(-2\pi^2 < \varepsilon_{1U}^2 > \ell^2) \right]^{n^2}, r = 0 \quad (15)$$

where, $< \varepsilon_{1U}^2 >$ and $< \varepsilon_{1D}^2 >$ are the first neighbor root mean square parameters that describe the non-uniform strain with distance according to the equation

$$\frac{1}{n} < \varepsilon_{1D}^2 > + < \varepsilon_{1U}^2 > = n^{2r} < \varepsilon_1^2 > \quad (16)$$

$< \varepsilon_{1U}^2 >$ and $< \varepsilon_{1D}^2 >$ are first evaluated by the LSA program and then used to determine 'r' and $< \varepsilon_1^2 >$ through the above equation.

The X-ray diffracted intensity equation (8) is transformed into the following integral by introducing the various line broadening functions as,

$$\frac{P'(h_3^0)}{2N_3 Y_0} = \int_0^{3/2} \left[1 - u + \frac{4}{27} u^3 \right] e^{-(\gamma u + \beta u^2)} \cos 2\pi h_3^0 u du \quad (17)$$

where,

$$u = \frac{n}{N_3} \quad (18)$$

$$h_3^0 = N_3 (h_3 - h_3' \ell) \quad (19)$$

$$\gamma = 2\pi N_3 (a_\gamma + \pi < \varepsilon_{1D}^2 > \ell^2) \quad (20)$$

$$\beta = \pi N_3^2 (a_\beta^2 + 2\pi < \varepsilon_{1U}^2 > \ell^2) \quad (21)$$

Equation (17) can be shown to be equivalent to the integral

$$P_2'(h_3^0) = Y_0' \int_{-b}^b g_1(x) P_1'(h_3^0 - x) dx \quad (22)$$

where the functions g_1 and P_1' are given by

$$\frac{g_1(h_3^0)}{2Y_0N_3} = \int_0^{3/2} e^{-\beta u^2} \cos 2\pi h_3^0 u du \quad (23)$$

and,

$$\frac{P_1'(h_3^0)}{2Y_0N_3} = \int_0^{3/2} \left[1 - u + \frac{4}{27}u^3 \right] e^{-\gamma u} \cos 2\pi h_3^0 u du \quad (24)$$

Equation (22) is numerically evaluated with a nine point Gauss-Legendre quadrature which requires the integration limits to be -1 to 1. To accomplish this the variable x is changed to a new variable z such that equation (22) becomes

$$P_2'(h_3^0) = Y_0'' \int_{-1}^1 g_1(bz) P_1'(h_3^0 - bz) dz \quad (25)$$

Using this numerical approach, the final intensity expression is derived as

$$P_2'(h_3^0) = Y_0'' \sum_{i=1}^9 W_i \exp \left[\frac{-\pi b^2 z_i^2}{(a_\beta^2 + 2N_3^2 \pi < \epsilon_{1U}^2 > \ell^2)} \right] \times \left[\frac{\gamma}{D} + \frac{\{2\pi(h_3^0 - bz_i)\}^2 - \gamma^2 + \frac{8}{9} \cos(4T)}{D^2} - FLC_i \right] \quad (26)$$

where

$$FLC_i = \frac{e^{-\frac{3}{2}\gamma}}{D^{3/2}} \left[\frac{4}{3} \cos \{3\pi(h_3^0 - bz_i) + 3T\} + \frac{\frac{8}{9} \cos \{3\pi(h_3^0 - bz_i) + 4T\}}{D^{1/2}} \right] \quad (27)$$

$$D = \{2\pi(h_3^0 - bz_i)\}^2 + \gamma^2 \quad (28)$$

$$T = \tan^{-1} \left[\frac{2\pi(h_3^0 - bz_i)}{\gamma} \right] \quad (29)$$

$$b = \frac{1}{z_{\max}} \left[\frac{\ln(125)}{\pi} \right]^{1/2} \left(a_\beta^2 + 2N_3^2 \pi \langle \epsilon_{1U}^2 \rangle \ell^2 \right)^{1/2} \quad (30)$$

Here, z_i and w_i are the roots and weighting factors of the Gauss-Legendre quadrature. The program LSA performs a least squares fit of the experimental diffracted peak intensity profile to the above final intensity expression. Detailed descriptions of the program LSA and the theory are given in Ref.46. The instrumental parameters a_γ and a_β are to be estimated from the line shape analysis of diffraction peaks of a stress-free powder sample with no particle size broadening effects.

3.2.2 Diffraction from Ideal Multilayer Thin Films

An ideal multilayer thin film can be visualized as a layered structure in which there are periodic alternating thin blocks of two different materials with perfect one-dimensional order in the direction perpendicular to the plane of the film. In other words, both chemical and structural modulation waves in the ideal multilayer film are perfect square or rectangular waves and the interfaces are atomically sharp and abrupt. An ideal multilayer film also is assumed to contain an integral number of layers and the layers are considered to be completely coherent with each other so as to form a 'one-dimensional superlattice'. In the case of a metallic multilayer film in which two metals are deposited to form alternating layers, it is usually found that the thin layers are polycrystalline with a high degree of texture [3, 4, 5, 6]. It is also observed that high-quality multilayer thin films with ultra-thin layers ($< 40 \text{ \AA}$) have a tendency to form coherent or at least semi-coherent interfaces even when metals with two different crystal structures are deposited [3, 4, 5]. Any lattice mismatch is accommodated by elastic coherency strains. The one-dimensional lattice distortion due to the variation of the d-spacing of the crystal planes that are perpendicular to the modulation direction in such ideal multilayers can be described with a periodic

step function. Segmuller and Blakeslee [58] have used this step model to derive the expression for the X-ray diffracted intensity. This model was adopted for the simulation of X-ray diffraction pattern arising an ideal Mo/Al superlattice thin film as follows.

The d-spacing variation in an ideal Mo/Al multilayer superlattice can be described by the periodic step function

$$\begin{aligned} d_n &= d_{Al} && \text{for } 0 < n < N_{Al} \\ d_n &= d_{Mo} && \text{for } N_{Al} < n < N = N_{Al} + N_{Mo} \\ d_n &= \frac{(d_{Al} + d_{Mo})}{2} && \text{for } n = N_{Al} \text{ and } n = N \end{aligned} \quad (31)$$

where,

- d_{Al} = Lattice spacing of Al (111) planes
- d_{Mo} = Lattice spacing of Mo (110) planes
- N_{Al} = The number of (111) planes in an Al layer
- N_{Mo} = The number of (110) planes in a Mo layer

In this ideal case, the super lattice unit cell consists of one layer pair Al/Mo and its period is given by

$$d_0N = d_{Al}N_{Al} + d_{Mo}N_{Mo} \quad (32)$$

The diffracted amplitude A of X-rays from this superlattice is given by the summation, (with orthorhombic axes and general (00ℓ) reflection)

$$\begin{aligned} A(h_3) &= \sum_{n_1, n_2, n_3} \exp[2\pi i(h_1 n_1 + h_2 n_2 + h_3 N n_3)] \times \left[F_{Al} \sum_{n=0}^{N_{Al}-1} \exp\left[2\pi i h_3(n + 1/2) \frac{d_{Al}}{d_0}\right] \right. \\ &\quad \left. + F_{Mo} \exp\left[2\pi i h_3 N_{Al} \frac{d_{Al}}{d_0}\right] \times \sum_{n=0}^{N_{Mo}-1} \exp\left[2\pi i h_3(n + 1/2) \frac{d_{Mo}}{d_0}\right] \right] \quad (33) \end{aligned}$$

where,

- F_{Al} = Structure factor for Al layer

F_{Mo} = Structure factor for Mo layer

Here the reciprocal lattice vector h_3 is defined in the reciprocal lattice of the superlattice crystal with the d-spacing d_0 . The first summation is performed over this lattice with unit cell size d_0N in the a_3 direction. The above summations can be made using the sum formula for geometric series. The final expression obtained for the diffracted intensity [58] from the ideal Mo/Al multilayer thin film is obtained as

$$I(h_3) = \left[\frac{\sin \pi h_3 N N_L}{\sin \pi h_3 N} \right]^2 \times \left[F_{Al}^2 \left[\frac{\sin \pi h_3 N_{Al} d_{Al}/d_0}{\sin \pi h_3 d_{Al}/d_0} \right]^2 + F_{Mo}^2 \left[\frac{\sin \pi h_3 N_{Mo} d_{Mo}/d_0}{\sin \pi h_3 d_{Mo}/d_0} \right]^2 \right. \\ \left. + 2F_{Al}F_{Mo} \cos \pi h_3 N \left[\frac{\sin \pi h_3 N_{Al} d_{Al}/d_0}{\sin \pi h_3 d_{Al}/d_0} \right] \left[\frac{\sin \pi h_3 N_{Mo} d_{Mo}/d_0}{\sin \pi h_3 d_{Mo}/d_0} \right] \right] \quad (34)$$

where,

N_L = Total number of Mo + Al layer pairs in the film

The above expression was used to simulate the diffraction pattern from an ideal Mo/Al multilayer film with Mo(110) texture and Al(111) texture. The expression gives the integrated intensity of main and satellite reflections with their positions in reciprocal space.

3.3 RBS Analysis for Composition Profiles

The principle behind RBS analysis is that elemental composition and depth information is obtained from the energy loss suffered by high energy light ions in a single collision with a target atom. A primary ion with energy E_1 incident on the sample surface penetrates into the sample to a depth x due to its high energy where it suffers a single collision with a target atom and is scattered back to the surface where it emerges at energy E_2 . The ion paths before and after

collision are straight lines along which the ion loses energy into collision with electrons and plasmons but is not deflected. The schematic geometry of a RBS experimental arrangement is given in Figure 7 on page 44. According to Behrisch and Scherzer [59], the differential electronic energy loss dE per unit path length s is given by

$$\frac{dE}{ds} = -A_v E^v \quad (35)$$

where E is the ion energy, v is an exponent depending on the energy range, and A_v is a constant dependent on v . When the ion reaches the depth x below the surface its energy is reduced to E_1' given by

$$E_1' = [E_1^{1-v} - (1-v)A_v(x/\cos\alpha)]^{1/(1-v)} \quad (36)$$

The collision with the target atom causes a further energy loss characterized by the nuclear energy loss factor k given by,

$$k = \frac{E_2' M_1 \cos\theta}{E_1' M_1 + M_2} + \left[\frac{M_1 \cos\theta}{M_1 + M_2} + \frac{M_2 - M_1}{M_1 + M_2} \right]^{1/2} \quad (37)$$

where E_2' is the ion energy immediately after collision. The ion coming out again suffers energy loss so that the final energy E_2 is given by

$$E_2 = \left[(k^2 E_1)^{1-v} - (1-v)A_v \frac{x}{\cos\alpha} \left[k^{2(1-v)} + \frac{\cos\alpha}{\cos\beta} \right] \right]^{1/(1-v)} \quad (38)$$

As can be seen from the above equation, the final energy of the ion yields information on the mass number M_2 of the target atom via k , and the depth x where the collision had taken place. The software package RUMP which was written based on this theory, is also capable of generating simulated RBS spectrum of a sample with the composition versus depth information given as input to the program. The sample is divided into layers of varying thicknesses with each layer having either a constant composition or having more sublayers in it with each sublayer having constant composition. The thickness of each layer with its composition profile is input

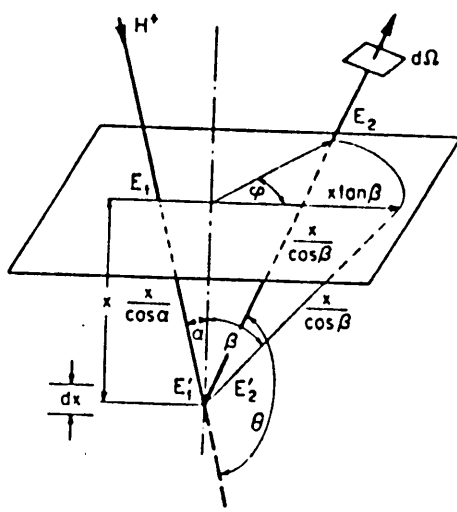


Figure 7. Schematic experimental geometry of RBS.

starting from the topmost layer. The thickness and composition values of each layer so specified is adjusted so as to fit the experimental RBS spectrum. The sample description in terms of layer thickness and composition that gives a near perfect fit to the experimental spectrum is the composition-depth profile of the sample. Details of the RUMP program layout, algorithms, and operation can be had from the References [54] and [55].

3.4 *Electron Diffraction Patterns*

The method of solving electron diffraction patterns (both spot and ring patterns) with the relevant equation is discussed in this section.

3.4.1 Ring Patterns

Electron diffraction occurring from randomly oriented grains of a polycrystalline thin film gives rise to a series of cones of reflection with each cone of apex angle 4θ , where θ is the Bragg angle for the particular reflection. If one constructs the Ewald reflecting sphere by drawing a sphere of radius $(1/\lambda)$ from the thin film sample so that it passes through the origin of the reciprocal lattice, each of the above diffraction cones intersect the reflection sphere on a circle. These circles are the ones that are seen in a electron diffraction ring pattern. The radius of the circle is the magnitude of the reciprocal lattice vector g ($= 1/d_{hkl}$) ($= 2 \sin\theta/\lambda$) for that particular reflection. However, the radius of a ring measured on the diffraction pattern is actually magnified by the electron microscope. This magnification factor is the camera constant of the microscope, λL , where L is the effective camera length resulting from the magnifications of the im-

aging lenses of the microscope. The formation of a diffraction pattern in a transmission electron microscope is illustrated in Figure 8 on page 47. Thus, the radius 'r' of a ring in a diffraction ring pattern is given by

$$r = L \tan 2\theta \cong L \sin 2\theta = (\lambda L/d) \quad (39)$$

Using this simple formula, one can obtain the d-spacings of various allowed reflections for the reflecting crystals. This information can then be used to identify the crystal structure, the lattice parameter and the identity of the unknown substance being studied. The breadth and spottiness of the ring pattern depend on the grain size and total number of grains contributing to the diffraction. Difficulties arise in indexing these ring patterns when the thin film has preferred orientation in which case some of the allowed reflections may be absent. Also, if care is not taken to avoid double diffraction, then one of the main diffracted beams itself gets diffracted and may cause rings corresponding to forbidden reflections to appear in the diffraction pattern. The indexing of ring patterns is carried out in much the same way as indexing of X-ray powder patterns using powder diffraction data files.

3.4.2 Spot Patterns

Electron diffraction spot patterns are obtained when only one grain or crystal in the sample thin film contributes to the diffraction. A diffraction spot occurs when the Ewald reflecting sphere passes through or very close to a reciprocal lattice point (hkl) for which the structure factor is non-zero. As seen before, the magnitude of reciprocal lattice vector ($1/d$) is related to the distance 'r' of the corresponding diffraction spot from the origin (000) by equation (). The procedure for solving the diffraction spot pattern for the general case involves the following steps [60].

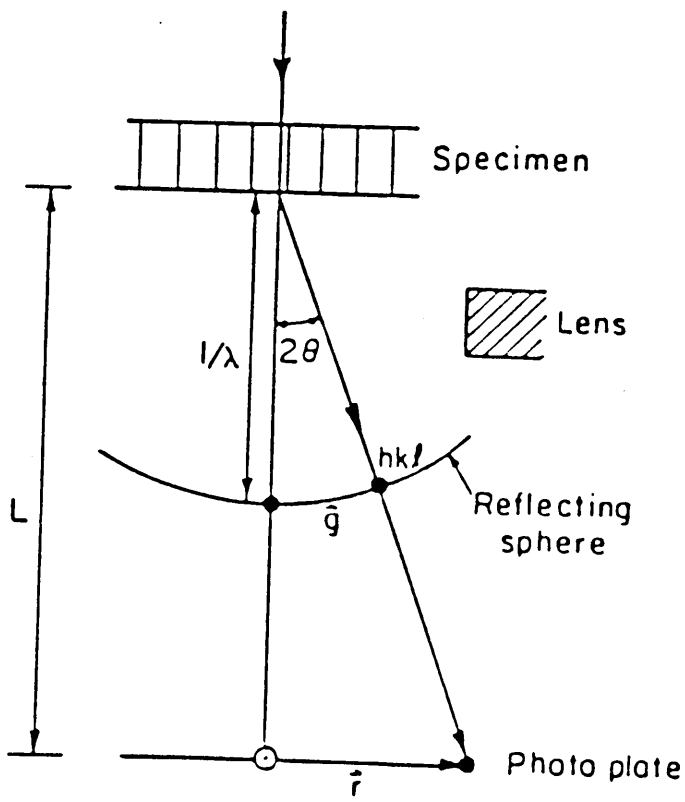


Figure 8. Formation of an electron diffraction pattern in a TEM.

1. The distances 'r' between the origin (000) and other spots in the pattern which are at different non-linear distances are measured.
2. The ratios of these distances are calculated and based on the ratios tentative (hkl) values are assigned to the spots in the pattern.
3. Then, the angle between two reciprocal lattice vectors (i.e., the angle between the two (hkl) planes giving rise to the two diffraction spots) is measured on the pattern and the signs and positions of the two indices are altered so that the measured angle is correct.
4. The zone axis of the reflecting planes in the pattern is determined by taking the cross-product of the above two reciprocal lattice vectors (rel vector).
5. Based on this consistent indices are assigned to the rest of the spots on the spot pattern.

Double diffraction usually causes difficulties in indexing spot patterns by causing some forbidden spots to occur. Since the missing reflections are important clues to the crystal structure it is necessary to eliminate double diffraction effects in obtaining spot patterns. Usually, tilting the sample removes the forbidden reflections caused by double diffraction by removing one of the strong diffracted beams required for double diffraction [60].

3.5 Diffusion Analysis for Bilayers

The composition profiles obtained from as-deposited and annealed bilayer Mo/Al thin films were analysed for interdiffusion. If the annealing conditions are such that the outer Mo layer is not depleted completely due to its inward diffusion into the Al layer, then the composition profiles obtained would satisfy the boundary conditions of the semi-infinite solid-state diffusion problem. For the general case of diffusion in bimetallic systems consisting of more than one phase, with the diffusion coefficients dependent on concentration, the Boltzmann-Matano method

of solution can be used for calculating interdiffusion coefficient [61] provided the diffusion process is one-dimensional with the new phases forming and growing in a planar fashion. If one defines the chemical interdiffusion coefficient \bar{D} by the equation

$$J_{Mo} = - \bar{D} \frac{\partial C_{Mo}}{\partial x} \quad (40)$$

where

- J_{Mo} = Mo flux in $\text{cm}^{-2} \text{ sec}^{-1}$
- C_{Mo} = Measured Mo concentration in atom fraction
- x = The distance from the Matano interface ($x=0$)

then Boltzmann-Matano solution of the diffusion equation

$$\frac{\partial C_{Mo}}{\partial t} = D(C_{Mo}) \frac{\partial^2 C_{Mo}}{\partial x^2} + \frac{dD(C_{Mo})}{dC_{Mo}} \left[\frac{\partial C_{Mo}}{\partial x} \right]^2 \quad (41)$$

gives the following expression for $D(C_{Mo})$ for a constant time 't' of diffusion.

$$D(C_{Mo}) = - \frac{1}{2t} \left[\frac{\partial C_{Mo}}{\partial x} \right]^{-1} \int_0^{C_{Mo}} x(C_{Mo}') dC_{Mo}' \quad (42)$$

where C_{Mo}' is the measured Mo concentration at a distance of $x(C_{Mo}')$ from the Matano interface. As usual, the Matano-interface location ($x=0$) is determined by requiring that the numerically integrated areas to the left and to the right of the interface be equal. The chemical interdiffusion coefficient \bar{D} is related to the individual volume diffusivities of Mo and Al by the Darken relation :

$$\bar{D} = C_{Al}D_{Mo} + C_{Mo}D_{Al} \quad (43)$$

From this relation it can be seen that \bar{D} would be approximately equal to D_{Mo} if C_{Mo} approaches a value of zero and would be equal to D_{Al} if C_{Mo} approaches the value 1. Using the above relation, it is then possible to calculate the lattice diffusivities of Mo and Al from $D(C_{Mo})$ versus C_{Mo} information obtained through the diffusion analysis.

4.0 EXPERIMENTAL PROCEDURE

The techniques used for fabrication and analysis of Mo/Al bilayer and multilayer films are presented in the following sections.

4.1 Fabrication of Thin Films

4.1.1 Sputter Deposition System

The preparation of the thin film samples were carried out in a Randex 2400-8J (Perkin Elmer Ultek Inc.) auto-tuned conventional rf-diode sputter deposition system. This sputtering system has three target sources which facilitates sequential deposition of up to three materials. Films of thickness varying from a few Angstroms to 0.1mm can be deposited with the system. Sputter-etching of the substrate is also possible. The targets are circular and of a size either 8 inches or 6 inches in diameter. Any of the three targets could be powered independently or the total power could be split between any two targets. The system has an annular substrate table that

is 21 inches in diameter and a J-arm substrate table that is approximately 8 inches in diameter. The J-arm table is supported by a J-arm through which chilled water could be circulated to water cool the J-arm table. The vacuum deposition chamber is evacuated by a high vacuum cryopump with liquid Nitrogen trap. The vacuum chamber could be pumped to as low as 3.5×10^{-7} torr pressure. The sputtering gas usually 99.99% pure Argon is admitted into the deposition chamber through a micrometer valve which is used for control of sputtering gas pressure. The sputtering system can be operated in the following modes:

1. Sputter deposit : All the supplied rf power goes to the target. The substrate table is grounded.
2. Bias sputter : A small amount of rf-power is applied to the substrate table. bias voltage is controlled manually and can be set to any value between 0 volts to -500 volts. Positive biasing is not possible in this mode.
3. Sputter etch : The rf power is applied to the substrate table so that the substrate could be sputtered etched.
4. DC bias : This mode is same as 1 but allows for external DC bias to be applied to the substrate table.

The target selection switch enables the selection of one of the targets to which power is applied. It also allows two targets to be powered simultaneously which is essential for the fabrication of the multilayered films. The sputtering system is powered by a 1000 watts (13.5 MHz) rf generator. The substrate table rotation can be set to continuous rotation. The rotation speed is controlled by a DC motor and can be set to designed speed. The target and the deposition chamber are cooled with chilled water from a water coolant system. The outlet water temperature was always maintained at less than 45°C. Panel meters were provided to indicate the values of target forward power, target bias, substrate bias and reflected power. The rf system is autotuned or manually tuned so that the reflected power never exceeds 10 watts. The sputtering pressure is monitored with a separate sensitive Pirani Gauge vacuum meter. The system does not have a load lock and the vacuum chamber is exposed to atmosphere after each deposition, and needs to be

pumped to a high vacuum before each depositing cycle. Also there are no substrate heating, or substrate temperature measurement and control facilities. The system geometry or substrate-target separation can be varied from 1 inch to 2.5 inches. This is an important deposition control parameter.

4.1.2 Calibration and Control of Sputter Deposition.

Before the final layered thin film deposition, the sputtering process parameters need to be optimized and the system calibrated to obtain the desired quality of the deposited films. The process parameters that can be varied to change the deposition conditions of the film are :

1. Forward power and target bias.
2. Sputtering gas, Argon pressure and flow rate.
3. Substrate negative bias potential.
4. Target-substrate separation distance.
5. Initial pumpdown vacuum.
6. Substrate sputter etch cleaning.
7. Substrate cooling.

Since the initial pump down vacuum determines how clean the system is when the actual deposition is started and hence the purity of the deposited film, always the maximum achievable vacuum was attained. This vacuum level was in the range $7 \text{ to } 3 \times 10^{-7}$ Torr. It was also found that the system needs to be cleaned with methenol after every 30-40 hours of usage to achieve levels of vacuum in the above range. Since the deposition of layered thin films require as much decoupling of substrate from the source, the substrate to source separation distance was kept at its maximum possible $2\frac{1}{2}$ inches, even though this may cause a decrease in deposition

rate. The effect of substrate bias was examined by depositing pure Mo and pure Al films at 0, -30, and -40 volts substrate bias voltages. Higher substrate biasing was not attempted because it was seen that increasing substrate bias deteriorated the interface sharpness in layered films. The effect of argon gas pressure was examined by setting the pressure levels at 10, 15, 20 and 25 mTorr during the deposition of pure metal (Mo and Al) films. The vacuum system was operated at its full capacity to maintain maximum flow rate. The Argon gas pressure was controlled not by the outlet pressure valve but by the control of inlet flow. The forward power and target bias applied to the targets was maintained at the maximum possible steady value, since it was desired to have the maximum possible steady deposition rates. The power was usually between 800 watts to 1000 watts. The target biasing voltages were between a 1000 V to 1300V, depending upon the power applied.

Firstly for optimization of deposition parameters and for calibration of the deposition rate under optimized conditions, pure Mo and pure Al thin film samples were prepared. The pure metal targets used were of 99.99% purity. The Mo target was 6 inches in diameter and the Al was 8 inches. Each time before the deposition of the film, each target was sputtered for 30 minutes to 1 hour to clear the target surface to remove any surface oxides and contaminants that may have formed when the targets were exposed to the atmosphere. To asses the effect of substrate sputter etching, in some cases the substrate were sputtered etched for 30 seconds, 1 minute and 2 minutes. The substrate used were highly polished Si(100) single crystal with a cut better than $\pm \frac{1}{2}^\circ$ and scratch free optically perfect thin microscope cover grass. The silicon substrates were circular with $\frac{1}{8}$ inch diameter and $1/16$ inch thick and were polished on one side only. The glass substrates were either 22mm diameter circles or 18x18mm squares with thickness of 0.2mm. Sputter etching for longer times seemed to introduce surface roughness and hence was restricted to 30 seconds or less, which should be enough for homogenizing the substrate.

The as deposited pure metal films were examined visually and under SEM for surface roughness and uniformity of coverage of the substrate. These films then were subjected to examination by X-ray diffraction. The strain and subgrain sizes were roughly estimated from the diffraction profile shifts and full width at half maximum of the diffraction peaks. Several trial de-

positions were done with pure metals under different settings of the deposition control parameters such as substrate bias, gas pressure, substrate etching and substrate cooling. The films were examined for quality and the deposition conditions were optimized. The pure metal films were of approximately 1mm thickness. It was found that the Mo films got deposited with uniform substrate coverage with very smooth and highly reflecting surface. However, it was difficult to obtain good quality Al films. Substrate biasing was necessary to get uniform coverage of the substrate. Also Al deposition rate is about 3 times faster than Mo deposited under similar conditions. Both for Al and Mo substrate biasing at -30V improved the film quality and also the texture of the films. Mo films deposited with substrate bias had (110) texture and Al films had (111) texture. The texture was qualitatively studied by measuring the ratios of the X-ray integrated intensities of various (hkl) reflections from thin samples and comparing it with the ratios obtained from stress free powder samples.

Increase of Ar gas pressure increased the rate of deposition and also the uniformity of surface coverage in both Mo and Al thin films. However, beyond 20 mTorr pressure the deposition rate decreased for Al and the uniformity of film coverage deteriorated with pores and discontinuities observable in the Al films. Except for the increased texture and strain, Mo films did not show any significant changes in film quality. The Al films had poor surface reflectivity which is probably due to the Al oxide layer. However the backside of the film as seen through the transparent glass substrates was highly reflective and continuous when Al was deposited with -30 V substrate bias on a substrate sputter etched for 2 minutes, at a sputtering gas pressure of 18 mTorr. The aim being the deposition of layered films, it is necessary to minimize the substrate negative bias to as low a value as possible if it could not be avoided. This is to improve the sharpness of the layer interfaces which may be affected adversely by positive ion bombardment of the growing film.

The question of whether to apply substrate bias or not during the deposition of layered films is easily resolved for deposition of bilayers. First a thick uniform layer of Al is deposited with a -30V substrate bias on top of which the Mo layer of required thickness is deposited

with no substrate biasing. In the case of the deposition of multi-layers with ultra-thin layers, substrate biasing becomes a problem.

Once the effects of variation of deposition parameters were estimated, the optimum values for these parameters were established and were used in the further depositions of layered films. The established optimum value for the sputtering gas pressure is 18 mTorr. Whenever substrate bias was applied, the value of the applied negative bias was 30 volts. To get the least possible interfacial diffusion in the samples during deposition, the substrate was cooled by circulating chilled water. However, since the Si and glass substrates are poor thermal conductors, it is expected that the substrate deposition surface temperature would rise to somewhere in the region of 100-200°C. It was not possible to measure the substrate temperature during deposition. Problems of arcing and fluctuations in the applied power were encountered when the full forward power of 1000 Watts was applied to the targets. Hence, in most cases the forward power applied was restricted to 800 Watts.

• 4.1.3 Measurement of Film Thickness and Deposition Rate

After setting the deposition parameters suitable for layered film deposition, pure Mo and Al films were deposited under these optimized conditions to estimate the deposition rate. To estimate the deposition rate accurately, one needs to measure the film thickness precisely. The film thickness of the deposited thin films were measured in two ways. The first method is to measure the weight gained by the substrate due to the deposition of the film on it. Assuming the density of the film to be the same as that of bulk Mo or bulk Al, the volume of the film was calculated by dividing the weight gain by bulk density. The volume of the film so obtained is then divided by the area covered by the film to get the thickness of the film. This method is used for getting a rough estimate of the film thickness. The accuracy of the thickness estimated using this method would be about $\pm 10\%$ of the total thickness of the Al film and about $\pm 5\%$ for Mo film.

The second and more accurate method involves the direct measurement of film thickness using an Å-Scope. The Varian Å-Scope employs the technique of multiple-beam optical interference. It can measure microscopic surface variations in the range from 30 Å to 2 µm. The accuracy of measurement is between 20 to 10 Å for measurement of thickness of thin films on smooth substrates. The instrument uses a sodium vapor lamp and optical elements to direct the light through specially coated Fizeau plate, which makes contact with the surface of the film sample at a slight angle and forms an air wedge. An interference fringe pattern is formed in the air wedge and is viewed through the filar eyepiece. If the thin film has high reflectivity, the fringes produced are sharp, dark, and well defined. A beveled edge on thin film specimen is necessary for clear measurement of pattern. This is achieved by the use of a steel mask placed on the substrate during the deposition. The mask produces a circular film on the substrate with beveled outer edge that makes an angle between 95 to 100° as shown in Figure 9 on page 57. The thin films themselves had good reflectivity and it was not necessary to put a reflective overcoat. The offset in the fringes caused by the surface variation from the substrate to the film at the beveled edge of the film is measured together with the fringe spacing using the graduated knob and cross-hair arrangement in the filar eyepiece. Using these measurements, the thickness of the thin film is calculated from the formula

$$\text{Thickness of thin film} = \frac{\text{Fringe offset}}{\text{Fringe spacing}} \times 2946 \text{ Å} \quad (44)$$

It was found that thickness estimates using the weight gain method agreed with the much more accurate Å-Scope measurements to within five percent of the total film thickness.

The deposition rates of pure Al and pure Mo thin films were obtained by dividing the measured thickness of the films by the total time of deposition. Typical deposition rate for Mo at 800 Watts forward power, 700 volts target bias, 30 volts substrate bias, 18 mTorr Ar gas pressure and 2½ inches target-substrate separation was 2.2 Å/sec. Deposition rate of Al under the same conditions except for the 1000 volts target bias was 3.5 Å/sec. The accuracy of these calibrations is again $\pm 10\%$ minimum.

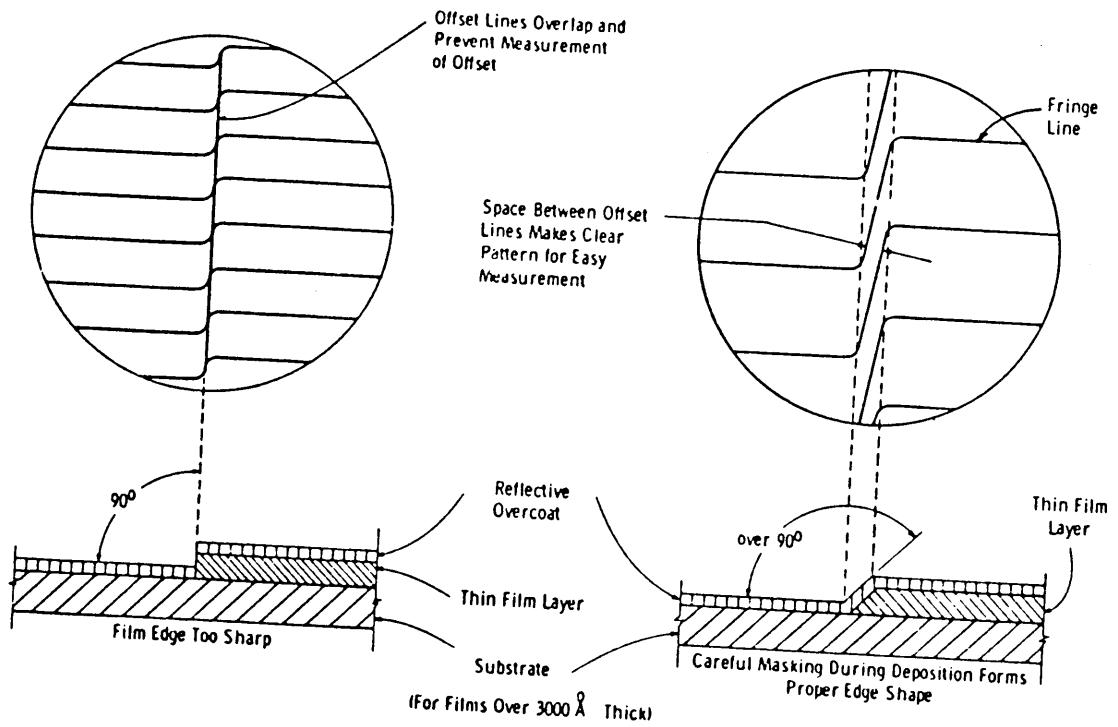


Figure 9. Film thickness measurement using \AA -scope.

4.1.4 Deposition of Mo/Al Bilayer Samples

The Mo/Al bilayer samples to be analysed by X-ray, AES, and SEM were deposited on to Si(100) and glass substrates placed on a water-cooled J-arm substrate table. The substrates were sputter-etched at 700 Watts power for 2 minutes after which a relatively thick layer of Al was sputter deposited on to the substrate with a substrate bias of -30 volts. The layer thickness of Al in bilayer samples used for X-ray analysis was 1.8 μm . The layer thickness of Al in bilayer samples used for AES and SEM analysis was 1.2 μm . Immediately after the deposition of the Al layer, the substrates were moved under the Mo target and the Mo layer was deposited to form the top layer. The thickness of the Mo layer analysed by X-ray diffraction was approximately 6000 \AA . The thickness of Mo layer analysed by AES and SEM was about 1200 \AA . The as-deposited films were analysed within two days after their fabrication and were always stored in a desiccator which was kept refrigerated at a temperature of about 15°C.

The bilayer thin film samples to be analysed by TEM were sputter deposited onto a carbon-coated standard TEM grid. The carbon layer is transparent to electron beam and provides support to the ultra-thin layers of Al and Mo deposited on the TEM grid. No substrate bias was applied during the deposition to avoid risking damage to the supporting carbon film. An Al layer of thickness 200 \AA was deposited first, on top of which a Mo layer of thickness 130 \AA was deposited. The as-deposited films were examined by TEM and then stored in a desiccator and kept refrigerated. Tables 3, 4, and 5 show the sputter deposition conditions employed during the deposition of the above three sets of Mo/Al bilayer thin films.

4.1.5 Deposition of Mo/Al multilayers

Attempts were made to deposit Mo/Al multilayer films on Si(100) single crystal substrates by sequential deposition. Sequential deposition of Mo and Al layers can be

Table 3. Typical sputter deposition conditions used for the deposition of 1200 Å Mo on Al bilayer film.

Film specimen:	1200 Å Mo on Al Bilayer Film
Initial Pressure:	3×10^{-7} Torr
Ar Pressure:	18 mTorr
Sputter Etch	
Time	2 min.
Substrate Bias	800 volts
Forward Power	700 watts
Reflected Power	< 2 watts
Deposition	
Mode	Al bias sputter / Mo sputter deposit
Time	61 min Al / 9 min Mo
Target Bias	1000 volts
Substrate Bias	30 volts for Al
Forward Power	800 watts
Reflected Power	< 2 watts
Anode Spacing	2 ½ inches
Deposition Rate	Mo-2.22 Å/sec ; Al-3.47 Å/sec
Substrate Temp.	< 150°C (Water cooled table)
Actual Thickness	1180 Å Mo / 12060 Å Al

Table 4. Typical sputter deposition conditions used for the deposition of 6000 Å Mo on Al bilayer film.

Film specimen:	6000 Å Mo on Al Bilayer Film
Initial Pressure:	3×10^{-7} Torr
Ar Pressure:	18 mTorr
Sputter Etch	
Time	2 min.
Substrate Bias	800 volts
Forward Power	700 watts
Reflected Power	< 2 watts
Deposition	
Mode	Al bias sputter / Mo sputter deposit
Time	61 min Al / 30 min Mo
Target Bias	1000 volts
Substrate Bias	30 volts for Al
Forward Power	800 watts
Reflected Power	< 2 watts
Anode Spacing	2 ½ inches
Deposition Rate	Mo-2.22 Å/sec ; Al-3.47 Å/sec
Substrate Temp.	< 150°C (Water cooled table)
Actual Thickness	5820 Å Mo / 12200 Å Al

Table 5. Typical sputter deposition conditions used for the deposition of 330 Å Mo on Al bilayer film for TEM studies.

Film specimen:	130 Å Mo on 200 Å Al - Bilayer Film
Initial Pressure:	3×10^{-7} Torr
Ar Pressure:	18 mTorr
Sputter Etch	
Time	0 min.
Substrate Bias	
Forward Power	
Reflected Power	
Deposition	
Mode	Al sputter deposit / Mo sputter deposit
Time	1 min Al / 1 min Mo
Target Bias	1000 volts
Substrate Bias	0 volts for Al
Forward Power	800 watts
Reflected Power	< 2 watts
Anode Spacing	2 ½ inches
Deposition Rate	Mo-2.22 Å/sec ; Al-3.47 Å/sec
Substrate Temp.	< 150°C (Water cooled table)
Actual Thickness	130 Å Mo / 200 Å Al

Table 6. Typical sputter deposition conditions used for the deposition of 200 Å Mo/Al multilayer film.

Film specimen:	Mo/Al - multilayer Film
Initial Pressure:	3.8×10^{-7} Torr
Ar Pressure:	18 mTorr
Sputter Etch	
Time	3 min.
Substrate Bias	800 volts
Forward Power	700 watts
Reflected Power	< 2 watts
Deposition	
Mode	Al bias sputter / Mo bias sputter
Time	113 sec Al / 39 sec Mo \times 24 revolutions
Target Bias	1000 volts
Substrate Bias	35 volts for Al
Forward Power	1000 watts
Reflected Power	< 10 watts
Anode Spacing	2 ½ inches
Deposition Rate	Mo-2.0 Å/sec ; Al-3.28 Å/sec
Substrate Temp.	< 150°C (Water cooled table)
Actual Thickness	187.5 Å Mo / 224.0 Å Al

achieved either by continuous rotation of the substrate table with both the Mo and Al targets depositing at the same time which requires splitting the power between the targets or by moving the substrates in sequence under one depositing target and then switching the power and the substrates to under the next target which does not require power splitting. Both methods were tried for the fabrication of Mo/Al multilayers. Once the deposition rates of the targets are established, the layer thickness of Mo and Al layers are determined by the time the substrates spend under each target or the rotational speed of the substrate table. The modulation wavelength of the films can be calculated from individual deposition rates and the stay time under the target and from the total thickness of the film divided by the total number of revolutions of the substrate table. The multilayers were deposited both with and without any substrate bias at 20 mTorr gas pressure. The films obtained by all of these various settings of deposition parameters were examined mainly by X-ray diffraction and AES for layer or interface quality and film texture.

4.2 Annealing Procedure

The Mo/Al bilayer thin films were annealed in 99.99% pure Argon atmosphere in a fused one inch I.D. quartz tube furnace. The thin film samples were supported in the tube on a horizontal alumina platform. The thermocouple control unit of the furnace allowed control of the temperature within $\pm 2^{\circ}\text{C}$. The furnace was precalibrated with a digital thermometer. The temperatures employed during the annealing process were 300, 350, 400, 450, 500, and 600 $^{\circ}\text{C}$. The furnace was preheated to the required temperature with the argon flowing and the sample introduced into the furnace after the furnace temperature stabilized. The samples were annealed at the required temperature for predetermined lengths of time in the range of 30 minutes to 48 hours. After the annealing cycle was completed the furnace was switched off and the samples were quickly brought to the cooler end of the furnace and allowed to cool to room temperature with argon flowing to prevent oxidation of the film material. Once the samples cooled down to room tem-

perature they were removed from the furnace and kept in a desiccator at 15°C, until they were examined later on. Continuous argon flow during annealing was ensured to prevent contamination of the film at higher temperatures.

4.3 Characterization of Bilayer Thin Film Samples

4.3.1 Analysis using AES

The as-deposited and annealed bilayer samples were analyzed using a Perkin Elmer scanning Auger Microprobe model PHI 610. The Auger microprobe was used in combination with a argon ion beam sputter gun to obtain composition-depth profiles of the bilayer samples. The sputter-etch rate of the argon sputter gun was calibrated using pure Mo and pure Al thin films of known thickness. The same conditions of ion beam current, beam voltage and raster size of the beam which were used during calibration runs were used during the analysis of bilayer films. This was to make sure that the instrument conditions were the same. The probe size of the electron beam was about 3 to 4 μm . The electron beam current used for acquiring the AES spectra and the peak to peak heights of Mo (186 eV) and Al (68 eV) lines during the sputter profiling was 0.02 μA and the beam voltage was 3 kV. The Argon ion beam voltage was 4 kV and the current was 5 μ . The raster size of the ion beam was 0.5mm \times 0.5mm. The initial vacuum level inside the specimen chamber was of the order of 10^{-9} Torr. Bilayer samples analyzed using this technique were cleaned with acetone and dried to remove any surface contaminants that might interfere with the profiling process.

The sputter-etch rates of pure Mo and pure Al were determined by sputtering through pure thin films of known standard thickness until the signal from the substrate silicon became stronger than the signal from the film material. These measured values of sputter-etch rates

for pure thin films were used in the analysis of composition profiles obtained from bilayer thin films.

4.3.2 Analysis using X-ray diffraction

A Siemens diffractometer with copper X-ray tube was used to collect the X-ray diffraction data from Mo and Al powder samples and the layered thin films (both bilayer and multi-layer samples). The samples were rotated in the plane of the film about the ϕ axis to bring more crystallites into the diffracting position. The diffractometer was used with a 0.2mm receiver slit, a one-half degree entrance slit, and Soller slits in the incident beam. The diffraction data was collected with a scintillation counter, a diffracted beam quartz crystal monochromator, a pulse-height analyzer, a ratemeter and a chart recorder. A standard (NBS) silicon powder was used to make small corrections to the peak 2θ positions. The monochromator was used to remove the $\text{Cu K}_{\alpha 2}$ component of the radiation whenever detailed slow scans were made to get integrated intensities, peak positions, and line shape.

The thin film samples and the powder samples were mounted on the X-ray specimen holder by the conventional method using mounting clay. Attempts were made to ensure that the sample surface was parallel to the face of the sample holder every time a sample was mounted. However, bilayer thin films deposited on thin glass substrates and annealed at temperatures higher than 400°C exhibited pronounced bending of the substrate and was difficult to mount exactly parallel to the sample holder.

Fast survey scans were used on the layered film samples first to identify the diffraction peaks. These scans were made at a speed of 1° per minute. The 2θ positions of all the observed peaks were recorded and were matched against the positions from the powder diffraction data book. It was found that most of the possible intermetallic compounds that form below 600°C were not reported in the powder diffraction data book. However, the crystal structures of most of these intermetallic compounds were available in the literature and the crystal structure data were

used to generate the powder diffraction data for most of the intermetallic compounds using the computer code POWDERT written in PL1 language. This program was available for use in generating powder diffraction pattern for crystalline materials whose structure is known. The observed peaks were compared with the patterns generated for intermetallic compounds in Mo/Al system using the powder diffraction program.

Detailed slow scans were made and the data were taken directly from the charts. The slow scans were made at a speed of 1/10 of a degree per minute. The integrated intensities were measured with an electronic planimeter after subtracting the background. The ratios of the integrated intensities were taken to estimate the texture in the thin film samples roughly. The strains in the pure and layered films were estimated by comparison with strain-free Mo and Al powder samples. Diffraction line profiles from Pure Mo, pureAl and the as-deposited bilayer film were subjected to line shape analysis to determine the subgrain particle size and root-mean-squared microstrain in these films.

4.3.3 Analysis using STEM

The TEM, SEM and EDAX facilities of the Philips-EM420 Scanning Transmission Electron Microscope were used to study the Mo/Al thin film for reactions, surface features and elemental analysis respectively. The TEM samples deposited on carbon-coated copper grids were viewed in the transmission mode to examine their micro-structure and to obtain crystal structure information about the phases through electron diffraction patterns. Bright-field images and diffraction spot and ring patterns were obtained from the as-deposited and annealed thin film samples. The microscope was calibrated for camera length and camera constant using a standard Al thin film sample with known d-spacing. The ring patterns obtained from the Al standard at a nominal camera length setting of 660mm were used to calculate the actual camera length at this setting. The same setting was used for all the diffraction patterns recorded on film for ease of comparison and analysis. The microscope however could not be calibrated for magnification settings and image ro-

tation of bright-field image with respect to the diffraction pattern because of problems of stability of the standard films used for such calibrations under the electron beam. So, the magnification values indicated on the TEM micrographs are only approximate. It was found that the bilayer TEM sample thin films get heated easily under a fairly intense electron beam that is focussed to smaller spot sizes and start to either bend or burn up thus drifting out of focus. For this reason, the TEM was operated at 100 kV at the minimum possible beam current setting just sufficient to illuminate the sample features when very small spot sizes were employed. Standard procedures for beam alignment, aperture alignment and stigmator adjustment were carried out to ensure optimum beam conditions. Standard procedures for obtaining TEM images and diffraction patterns are given in the operators' instruction manual for the EM420 STEM system and are not repeated here. The low beam current used necessitated long exposure times for recording the photomicrographs.

The use of the SEM facility in EM420 STEM restricts the maximum sample size to 6mm × 3mm area and less than 2mm height. This height requirement made it difficult to focus the electron beam on film surfaces deposited on 1/16 inch thick Si(100) substrates. The films deposited on thin glass substrates however were of ideally suited height for high magnification SEM studies of the film surface. The thin film samples on glass substrates were cut to appropriate area requirements with a fine diamond scribe. The sample was mounted in the sample holder with silver paint which not only serves as an adhesive that holds the sample to the holder but also serves as a grounding conductor so that the film surface gets grounded to prevent any charging of the surface. Surface and subsurface images were produced using both the dedicated backscattered electron detector and the secondary electron detector. The surface images were recorded on polaroid films with attached negative which enables prints to be made later when required. The surfaces were also viewed in Y-modulation mode to get a three dimensional view of the surface features. The images were analysed for quality of the surface and surface morphology.

Energy Dispersive X-ray spectra were obtained from both the TEM and the SEM samples so as to determine the elements present and possibly the ratio of Mo to Al in the thin film samples.

No TEM samples were prepared of multilayer samples. Only the surface roughness was examined in the high resolution SEM mode using EM420 STEM.

4.4 Characterization of Multilayer Films

4.4.1 Analysis with AES

Composition depth profiles were obtained from Mo/Al multilayer thin film sample with an estimated layer thickness of 200 Å for both Mo and Al layers in much the same way as for the bilayer thin films except that the sputtering rate of the Ar ion beam was reduced by increasing the raster area and decreasing the beam current. Sputter-etch rates for pure Mo and pure Al films were once again estimated under the new conditions and were found to be 35 Å/sec and 60 Å/sec respectively. The conditions of sputter-etching were 0.2 μ A beam current, 4.0 kV beam voltage and 2.0mm × 2.0mm raster size. The composition profile was extracted from the APPH versus sputter-time profile as in the case of bilayers. Only multilayer films that have layers thicker than 100 Å can be analysed by AES and hence only this multilayer film was analysed.

4.4.2 Analysis using X-ray diffraction

As discussed in the multilayer diffraction theory in Chapter 3, ideal multilayer thin films exhibit satellite reflections and low angle reflections around the main beam which reflect the layering and strain wave modulations in the film. The satellite and normal peaks at high angles were examined in much the same way as for bilayer thin films scanned in detail at high angles. To examine the probable low angle peaks that may occur close to the main beam, it is pref-

erable to use a Cr X-ray wavelength than Cu for the simple reason that the low angle peaks would be slightly farther away from the highly intense main beam and could possibly be separated from the main (000) reflection if the layer thickness is thin enough. Hence, a diffractometer with Cr tube was used along with a Ni filter. An accessory attachment to the specimen holder table called 'edge aperture' was used to prevent the main beam from reaching the detector directly which would prove disastrous for the detector. With the edge aperture, one can go as close to the main beam as 1/10 of a degree. The multi-layer sample was mounted on the specimen holder and the edge of the edge aperture was moved very close to the surface of the sample so as to avoid main beam spill-over directly to the detector. Slow scans at 1/10 of a degree per minute were made to detect any low angle peaks. These peaks would be observable only when the modulation wavelength of the multilayer is less than about 100 Å. Slow scans were made to detect any satellite reflections around a normal reflection at high angles. Texture of the films were examined by comparing the ratio of integrated intensities of various peaks from the multilayers to those from powder sample.

4.4.3 Analysis using RBS

A Mo/Al multilayer thin film was examined by the RBS technique at Naval Research Laboratories (NRL). He^+ ions derived from a Van de Graff generator at 2.0 MeV energy were used to bombard the sample multilayer. The Mo and Al layer thickness values estimated based on the deposition conditions for this film was approximately 200 Å. The sample mounting geometry was the IBM type in which the sample normal is in the same plane of the detector and incident beam. The detector resolution was 15 keV. Other relevant parameters set during the experiment is given along with the RBS spectrum of the sample and the composition-depth profile in the results section.

5.0 RESULTS AND DISCUSSION

5.1 Results for Mo/Al Bilayers

The results obtained for Mo/Al bilayer thin films in terms of their film quality and diffusional reactions at temperatures in the range of 300 to 600°C are presented in the following sections. The results are grouped into sections based on the analysis technique used for obtaining the results.

5.1.1 Analysis of As-deposited Bilayer Films

The bilayer films sputter deposited under conditions specified in tables 3, 4 and 5 were analyzed using AES, X-ray diffraction, and TEM techniques. The results of AES sputter depth profiling are presented in Figure 10 on page 72, Figure 11 on page 73, and Figure 12 on page 74. The Auger Peak to Peak Height (APPH) as a function of sputter-etch time is shown in Figure 10 on page 72. The peaks used for Mo and Al peak height measurement were the 186eV Mo Auger line and 68eV Al Auger line. The data presented in Figure 11 on page 73

is the sputter etch rate and sputter etch depth as a function of time. This figure was obtained using the data presented in Figure 10 on page 72 together with Equation 4 of Chapter 3. Using Equation 4, the sputter etch rate was obtained as a function of time. Then the sputtering depth was obtained by graphically integrating the etch-rate versus time curve. This depth-time relation was used in plotting Figure 12 on page 74 which presents the concentrations of Mo and Al as a function of depth. The APPH data of Figure 10 on page 72 were converted to bulk concentrations using Equations 5 and 6. The typical value used for R, the correction factor that accounts for atomic volume differences between Mo and Al was calculated to be 0.5579 from Equation 7. The sputter-etch rates of pure Mo and pure Al were experimentally measured to be 240 Å/sec and 405 Å/sec respectively. The density values used for Mo and Al in Equation 7 were the bulk density values of 10.2 g/cc and 2.7 g/cc respectively. The composition versus depth profile obtained in this way indicate that the interface thickness of the bilayer film to be about 200 Å. The examination of this 1200 Å thick Mo on Al bilayer using X-ray diffraction revealed a very fine sub-grain size of approximately 125 Å estimated using Scherrer's formula for sub-grain size of Mo. The observed peak width at half-maximum for Mo was 0.019 radians. The Aluminum reflection (111) was sharp and the sub-grain size estimated was about 900 Å. These values were only slightly less than the values of sub-grain sizes obtained with pure Mo and pure Al thin films. This means that the deposition of thinner layers does not affect the structure of the films once the deposition conditions are fixed.

Another bilayer film with the top Mo layer of thickness 6000 Å was examined with X-ray diffraction technique and it was found that the grain sizes remained approximately same as their original values for both Mo and Al. The X-ray diffraction pattern obtained from the 6000Å Mo on Al as-deposited thin film sample is presented in Figure 13 on page 76. Pure Mo and Al films that were used as standards were also examined using X-ray diffraction using line shape analysis of the Mo (110) and Al (111) reflections. Line shape analysis used only the first order peaks because the other reflections were of very low intensity. This may affect the values estimated for non-uniform strain in the film because one peak analysis is found to give results of particle size and strain that is not unique and to have a lot of fluctuations. In general first order peak line shape

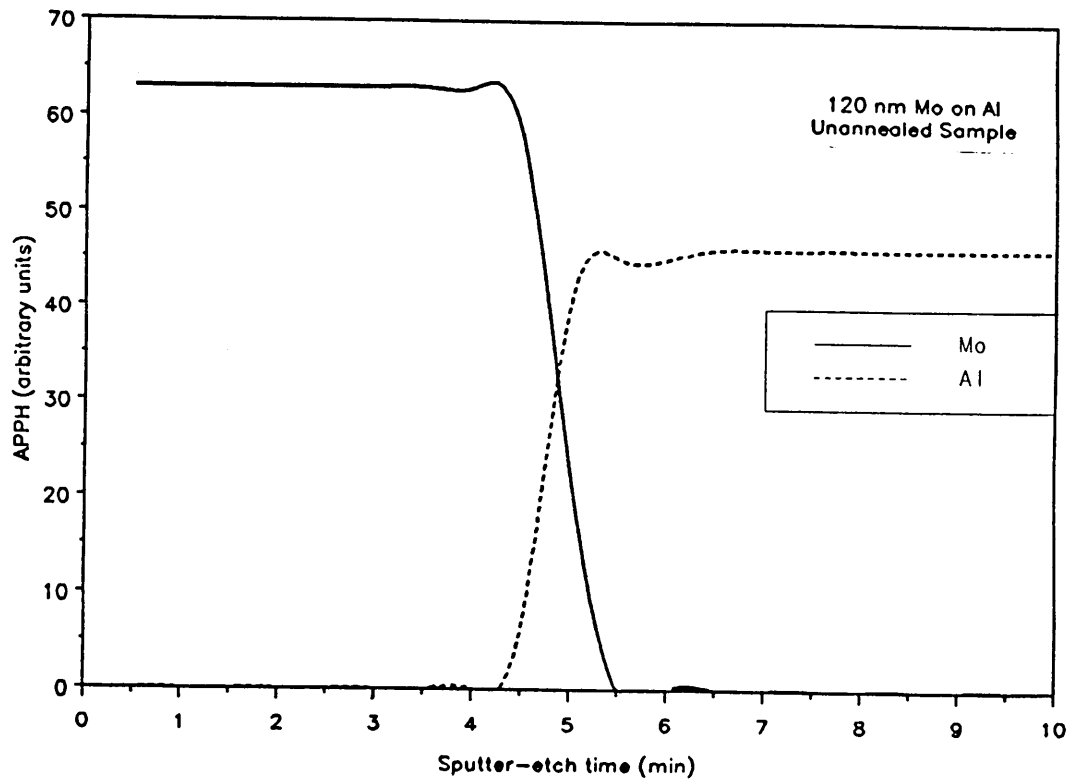


Figure 10. Measured APPH as a function of sputtering time for an as-deposited bilayer film: $\sim 1200 \text{ \AA}$ Mo layer on Al layer.

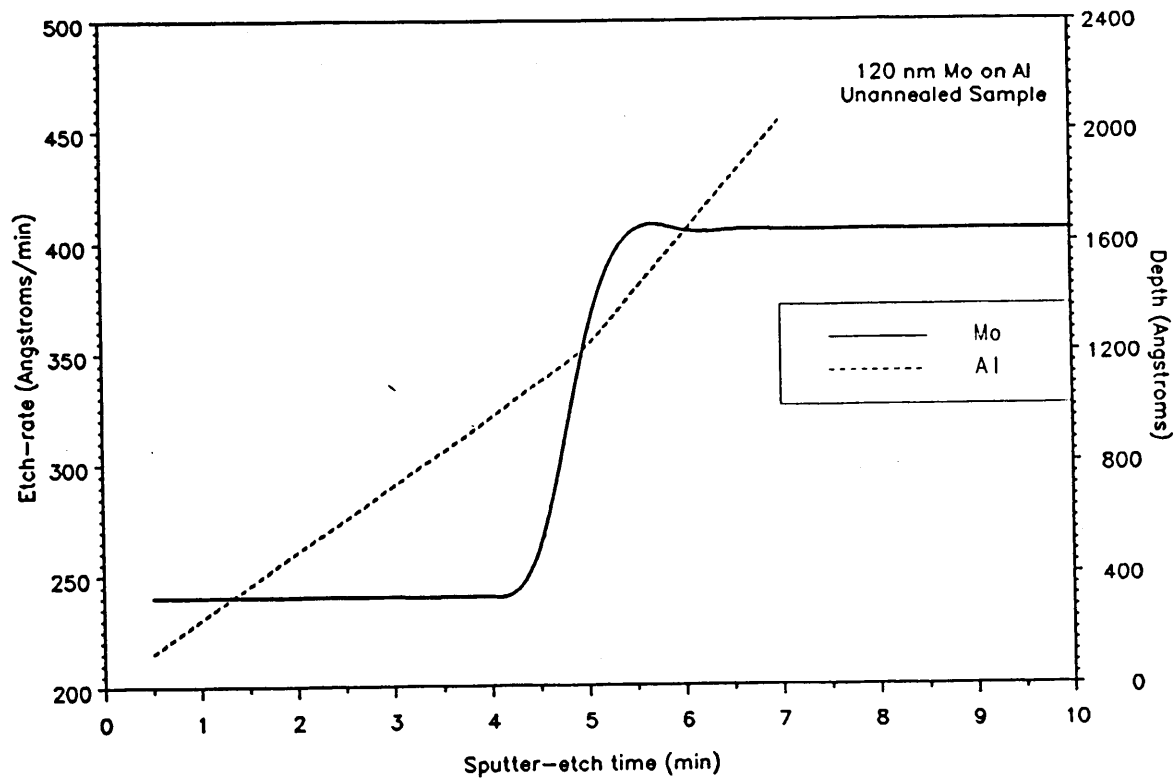


Figure 11. Sputter-etch rate and Sputter depth as functions of time for an as-deposited bilayer film: $\sim 1200 \text{ \AA}$ Mo layer on Al layer.

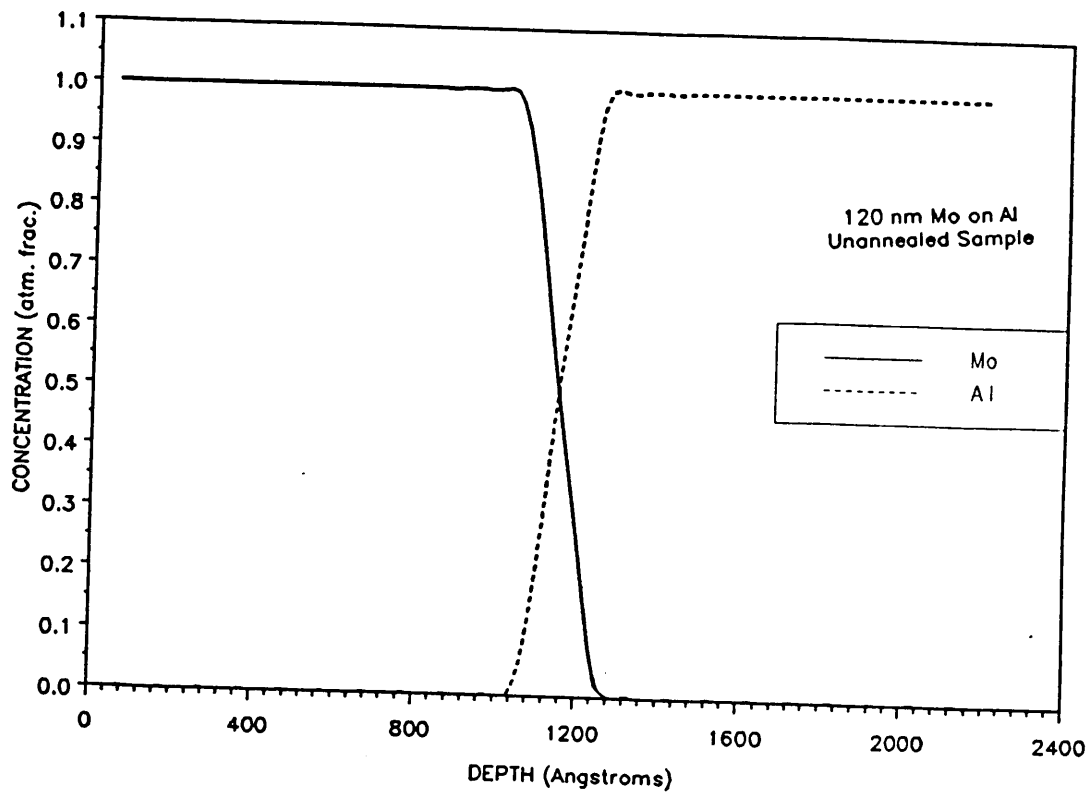


Figure 12. Bulk concentration versus depth profiles of Mo and Al in an as-deposited bilayer film: $\sim 1200 \text{ \AA}$ Mo layer on Al layer.

analysis gives better estimation of sub-grain particle size than of strain. The results obtained from line shape analysis of pure and bilayer films are presented in Table 7 on page 77. Such small grain sizes could possibly give rise to grain boundary diffusion dominating over bulk lattice diffusion at temperatures comparatively lower than the melting point of Al.

Analysis of as-deposited samples deposited on carbon coated copper grid for use in TEM revealed that the grain size of Mo to be much finer than Al. The bright field image of the as deposited sample along with the electron diffraction pattern obtained from a typical region of the sample is presented in Figure 14 on page 79. The bright or white areas in the image represent larger Al grains. As can be seen from the diffraction patterns, the diffraction pattern has a spot pattern superimposed on a ring pattern. The ring pattern corresponds to diffraction from several Mo crystals and the spot pattern corresponds to diffraction from a single Al grain oriented the [100] direction normal to the plane of the film. This is the case when a fine spot size for the electron beam was used. It is also found that some spots on the Mo ring pattern are stronger and that the rings are spotty and not continuous. This indicates that some of the Mo grains have a specific crystallographic orientation with the Al layer on which they were deposited. The orientation of the beam with respect to the Al diffracting grain was determined for different Al grains and it was found that Al did grow with [100] preferred orientation when deposited on carbon coated grids. In other words, the Al grains had [100] preferred orientation. The sample was viewed both from the Mo layer and the Al layer facing the electron beam. A classic case of double diffraction was observed when the Al layer was facing the electron beam and the beam reached the Mo layer after passing through the Al layer. This gives rise to a diffraction pattern in which there is a Mo ring pattern around several of the strong diffraction spots of Mo. The diffraction pattern showing this double diffraction effect is presented in Figure 15 on page 80. Since the Al layer is thin and is probably not favorably oriented for strong diffraction, the beam passes through the Al layer without diffracting. Then it seems to be diffracted strongly by a large Mo grain and each of the strongly diffracted beams serves as the input beam to the lower finer Mo grains and suffers double diffraction. This gives rise to the pattern shown. This indicates that the layering is good with less island formation effects even when the layer thickness is of the order of 100 Å at least in the case of TEM samples.

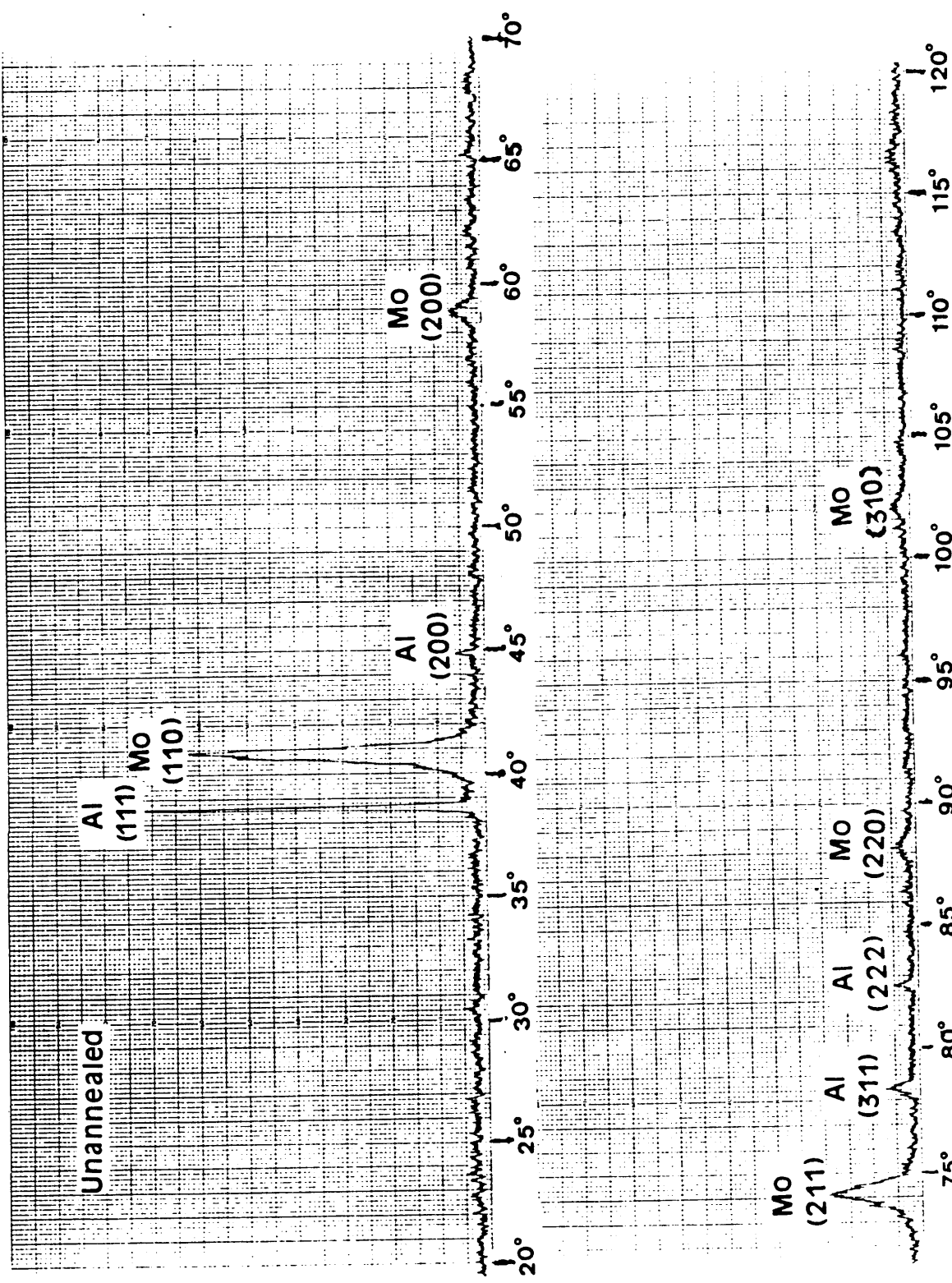


Figure 13. X-ray diffraction pattern (Intensity vs. 2 θ) of an as-deposited Mo/Al bilayer sample.

Table 7. Results of X-ray line shape analysis of Mo(110) and Al(111) reflections from Mo, Al and Mo/Al bilayer thin films.

Specimen	Particle Size $\langle L \rangle$ (Å)	Root-mean-squared strain	
		r	$\langle \varepsilon_1^2 \rangle^{1/2}$
As-deposited Mo film	142	-0.282	0.0120
As-deposited Al film	481	-0.210	0.0105
As-deposited Mo/Al film			
Mo	125	-0.296	0.0132
Al	403	-0.261	0.0117

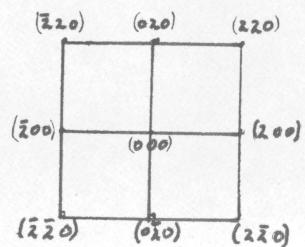
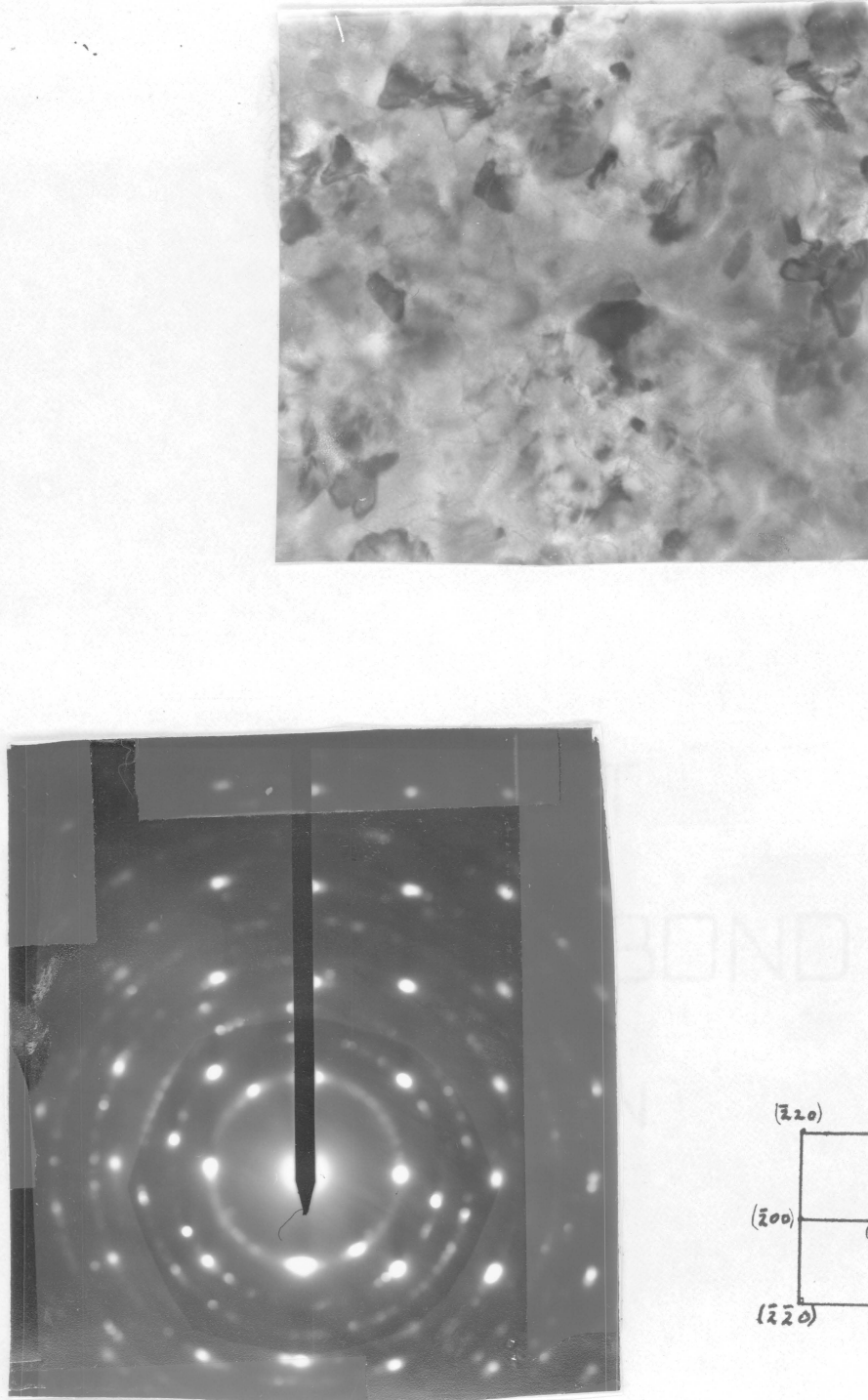


Figure 14. Bright field image and electron diffraction pattern of an as-deposited bilayer film.: Large bright areas are Al grains in the BEI. ($\times 490000$) EDP [$L = 758.5\text{mm}$ calib,(660min setting)] shows spot pattern from Al superimposed on ring pattern from Mo.(100keV)



Figure 15. Electron diffraction pattern of an as-deposited bilayer film showing double diffraction effect.: Strong diffraction spots from Al have rings from Mo around them. [L = 758.5mm calib.(660mm setting)]

The SEM images of pure Mo, pure Al and the bilayer thin films are presented in Figure 16 on page 81 and figref refid = fig16.. It is clear that the Mo film has an extremely smooth surface finish indicated by both the intensity modulated SED image and the Y-modulated SED image. The Al film has oxide coverage on the surface and as a result, the surface smoothness is not as good as the Mo film. However, when depositing bilayer films under high vacuum, it was expected that the Al layer surface on which the layer of Mo was deposited, would not get oxidized and would instead be smooth. This would ensure a relatively sharp interface which was observed using the AES analysis to be about 200 Å thick. The Mo oxide film that might form over the Mo surface upon exposure to atmosphere appears to be thin and featureless. It could be that this Mo-oxide layer is amorphous.

5.1.2 Analysis of Annealed Bilayer Thin Films

The films were annealed as indicated in section 4.2. As a result of annealing at 300 °C, there was considerable amount of interdiffusion as observed with the AES analysis. The results of AES composition-depth profiling of the annealed specimens are given in Figure 18 on page 84 through Figure 29 on page 95. It is clear from the profile for sample annealed at 300°C that there is only inter-mixing and no intermetallic compound formation which if present in detectable amounts would show up as a discontinuity in the composition-depth profile. Since the equilibrium diagram shows extremely low solid solubilities at both ends the significant amount of interdiffusion without compound formation could be due to non-equilibrium meta-stable solid solubility and/or Ar ion-beam mixing effects and/or formation of intermetallics with volume fraction below detectable limits. The X-ray diffraction pattern of a 6000 Å Mo on Al annealed at 300°C for 3 hours is presented in Figure 30 on page 96. The pattern confirms the absence of intermetallic compounds.

Annealing at 350°C resulted in compound formation which showed up as a discontinuity in the profile at about 8 atomic % Mo concentration and also inside the Al layer.

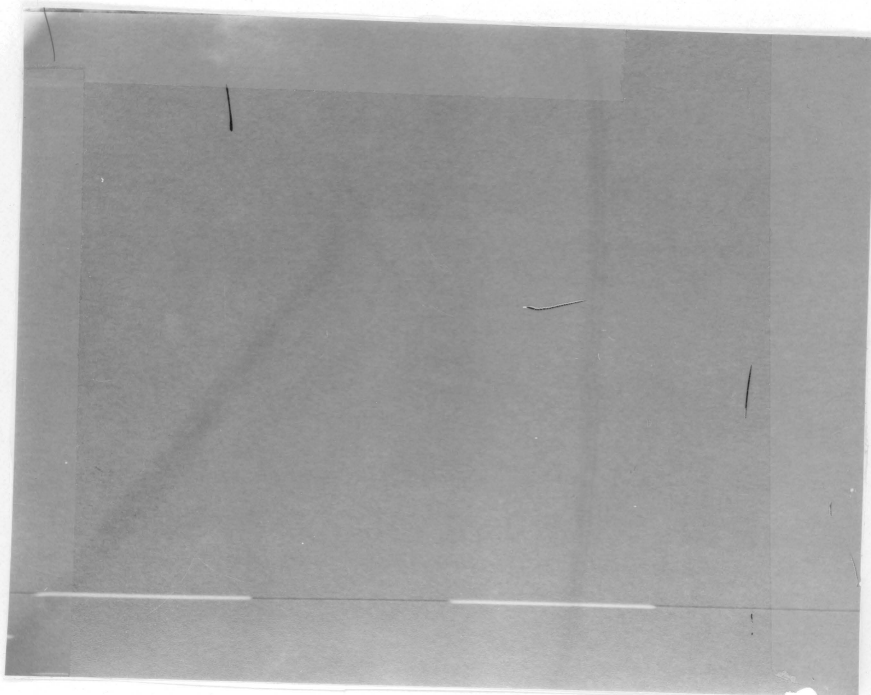
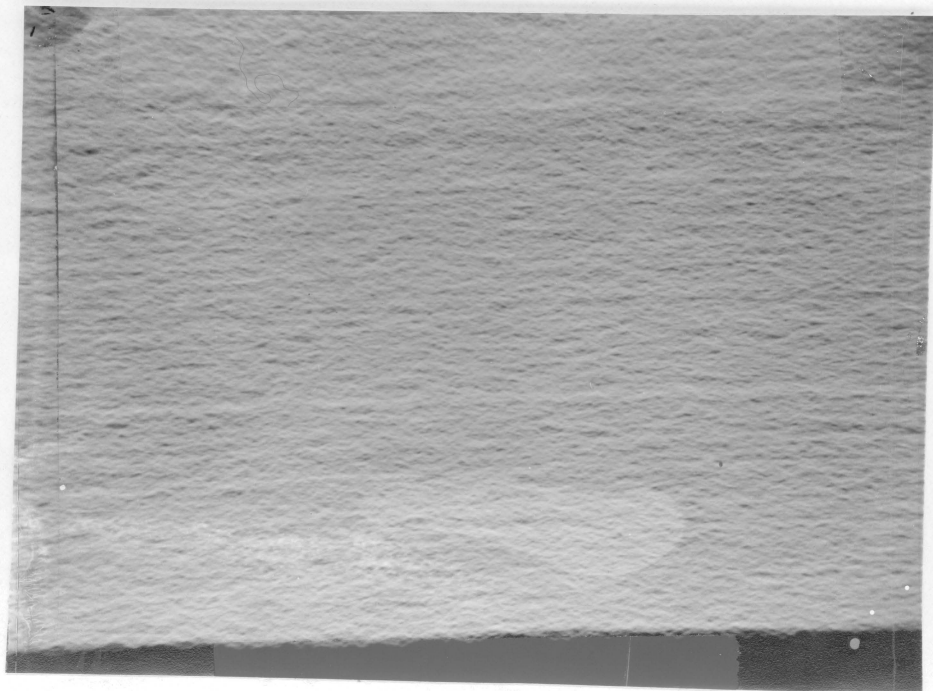


Figure 16. Surface topography of a pure Mo film: SEM image with SED. Top - Intensity modulated; bottom - Y-modulated. [$\times 50000$; $0.5\mu\text{m}$ marker]

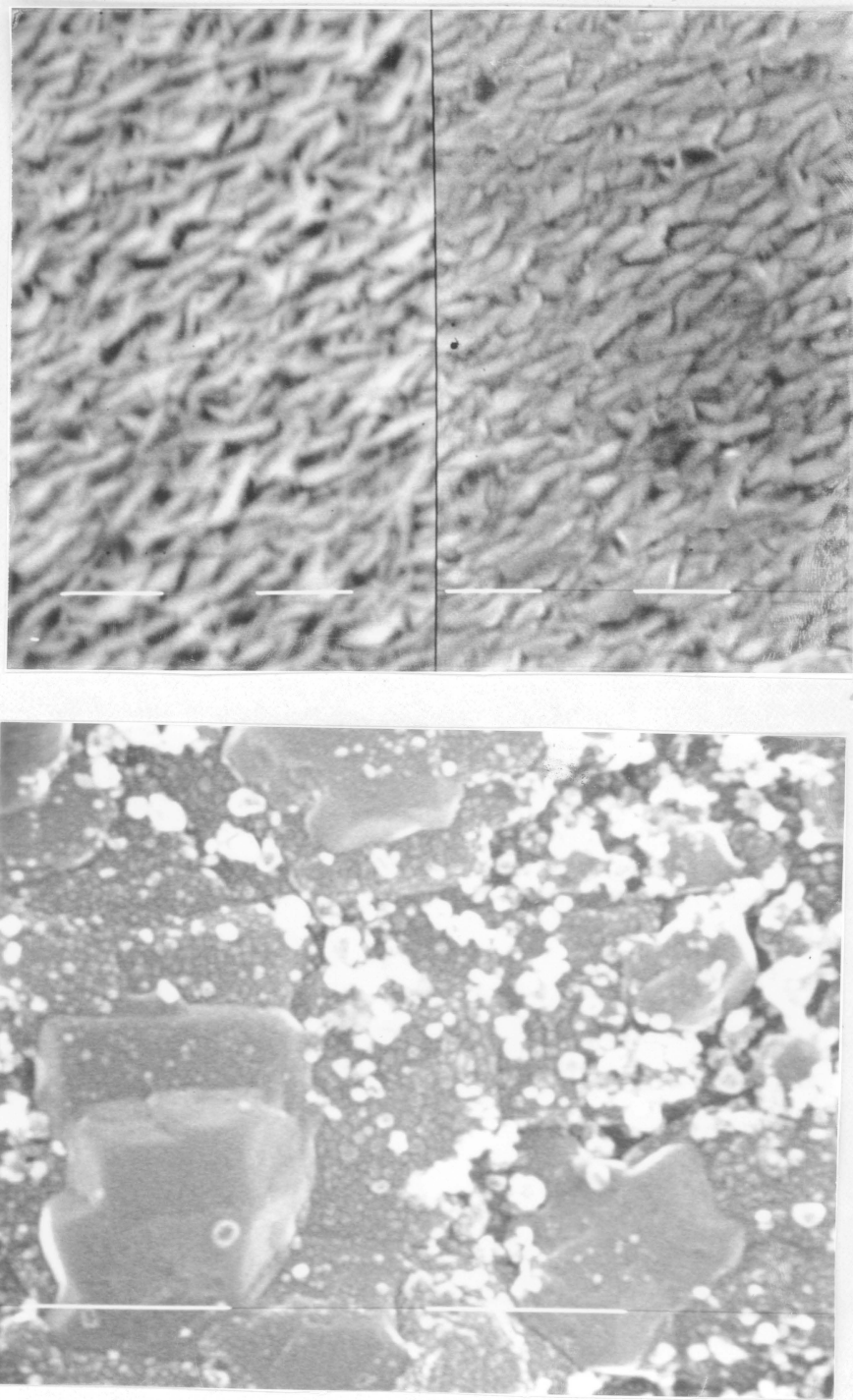


Figure 17. Surface topography of a pure Al and Mo/Al as-deposited bilayer films.: SEM image with SED. Top - Pure Al film; bottom - Mo/Al bilayer film .[$\times 50000$; $0.5\mu\text{m}$ marker]

The intermetallic compound corresponding to this discontinuity is Al_{12}Mo . This profile was obtained for a sample annealed for 3 hours. Prolonged annealing upto 64 hours at this temperature did not give any other compound formation. This was confirmed by X-ray diffraction analysis of the annealed sample and by TEM electron diffraction patterns. The X-ray diffraction pattern of this sample is shown in Figure 31 on page 97. Annealing led to grain growth of Al grains and Mo grains as observed by sharpening of the diffraction peaks for Al and Mo.

To monitor compound formations in these films, it was necessary to generate the powder diffraction patterns for all the possible intermetallic compounds that may form below 600°C. These patterns were generated using the computer code POWDERT so long as the crystal structure and the lattice parameter information for a possible compound were available. The diffraction patterns generated were useful in identifying the peaks observed in X-ray diffraction data and in interpreting the electron diffraction data. Part of the generated patterns are presented in Table 8 on page 102 which gives the 2θ , d-spacing and relative intensities of four most prominent reflections of various possible intermetallic compounds. For a sample annealed at 350°C, few weak and broad diffraction peaks appeared at positions corresponding to Al_{12}Mo . This is in agreement with the discontinuity or flat region in the Al side of the corresponding AES composition profile which is at a concentration of ~ 7.7 atomic% Mo.

Annealing at 400°C showed formation of more amount of Al_{12}Mo . This was observed with all three techniques. The AES profile also showed the tendency for formation of a discontinuity near the concentration level of 75 atomic % Mo. This would indicate the formation of the compound AlMo_3 . However, the peaks corresponding to AlMo_3 did not show up in the diffraction pattern obtained from the X-ray sample with thicker Mo layer. This could possibly be due to insufficient amount of compound formed at this temperature to be able to detect with X-rays.

The electron diffraction patterns and bright field images of the TEM samples annealed at temperatures ranging from 300 to 600°C are presented in Figure 36 on page 104 to Figure 41 on page 109. It can be seen from these diffraction patterns that many of the spots in the spot pattern seem to coincide with the rings of the ring pattern. This might be due to the

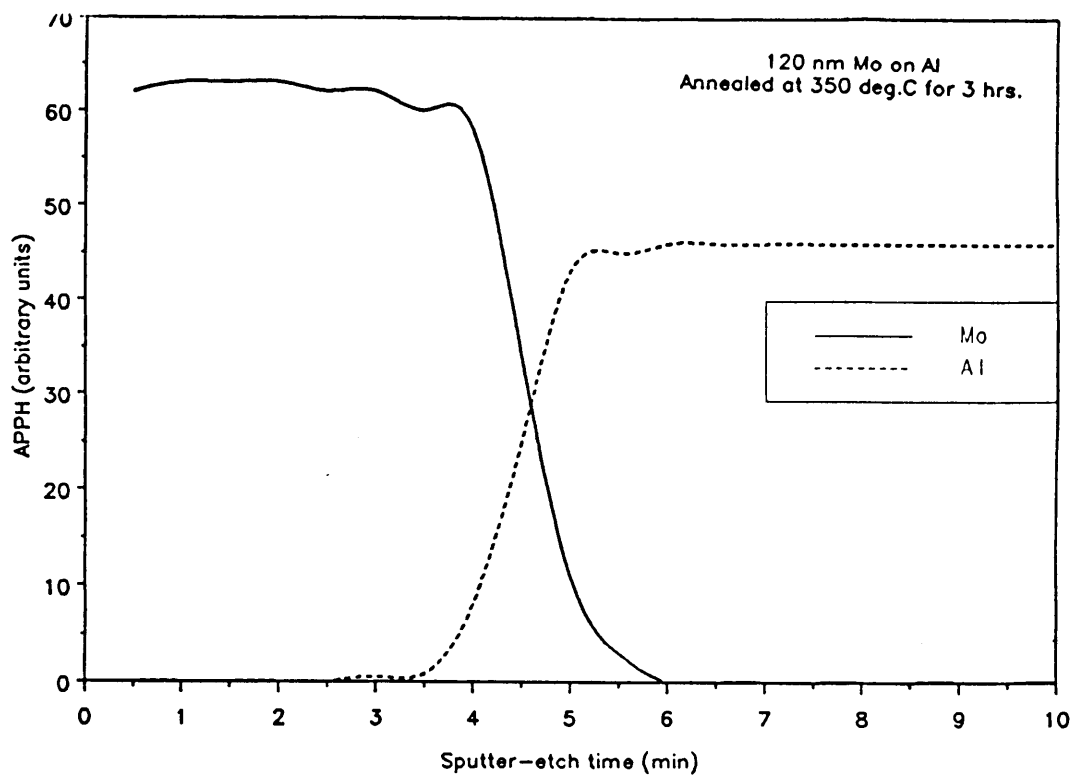


Figure 18. Measured APPH as a function of sputtering time for a bilayer film annealed at 300°C for 3 hours.: $\sim 1200 \text{ \AA}$ Mo layer on Al layer.

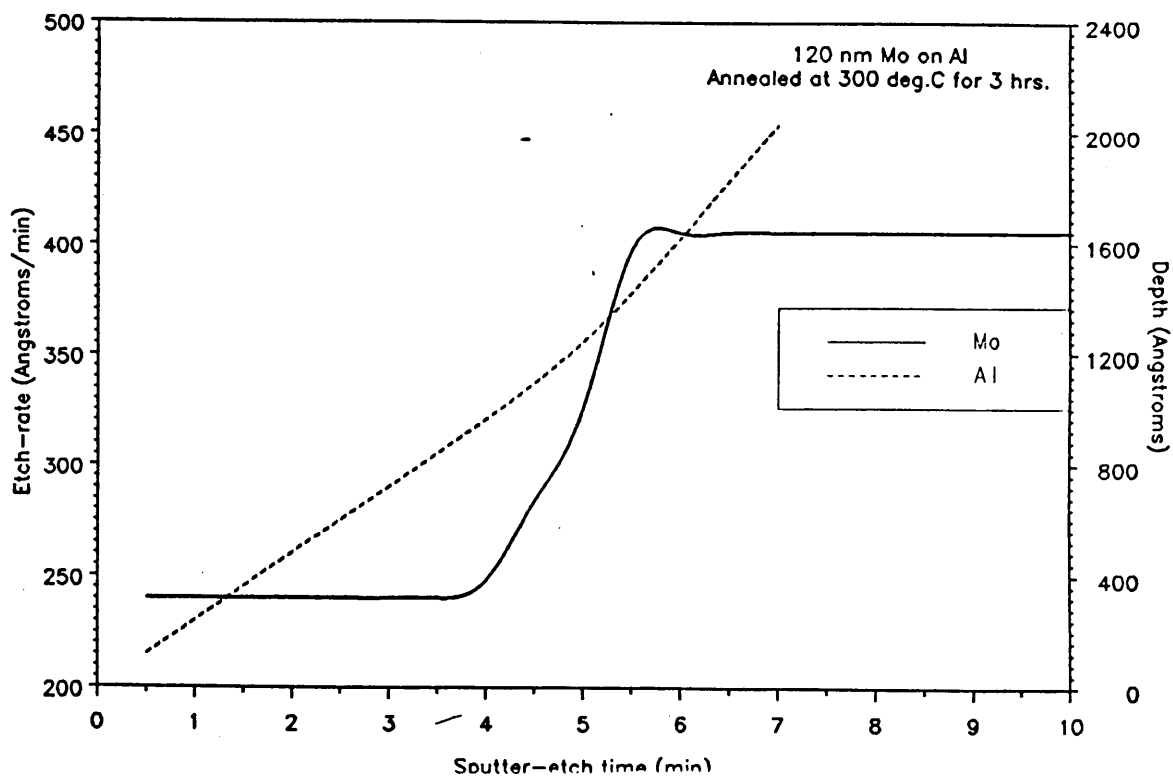


Figure 19. Sputter-etch rate and Sputter depth as functions of time for a bilayer film annealed at 300°C for 3 hours.: ~ 1200 Å Mo layer on Al layer.

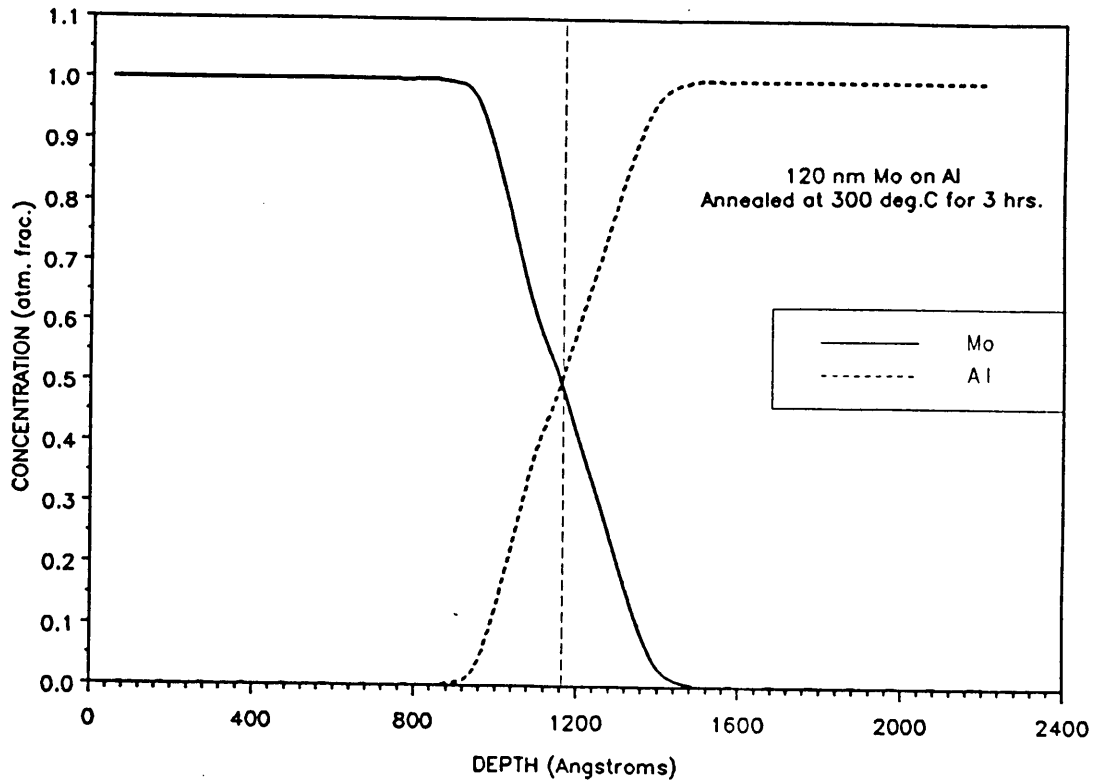


Figure 20. Bulk concentration versus depth profiles of Mo and Al in a bilayer film annealed at 300°C for 3 hours.: ~ 1200 Å Mo layer on Al layer.

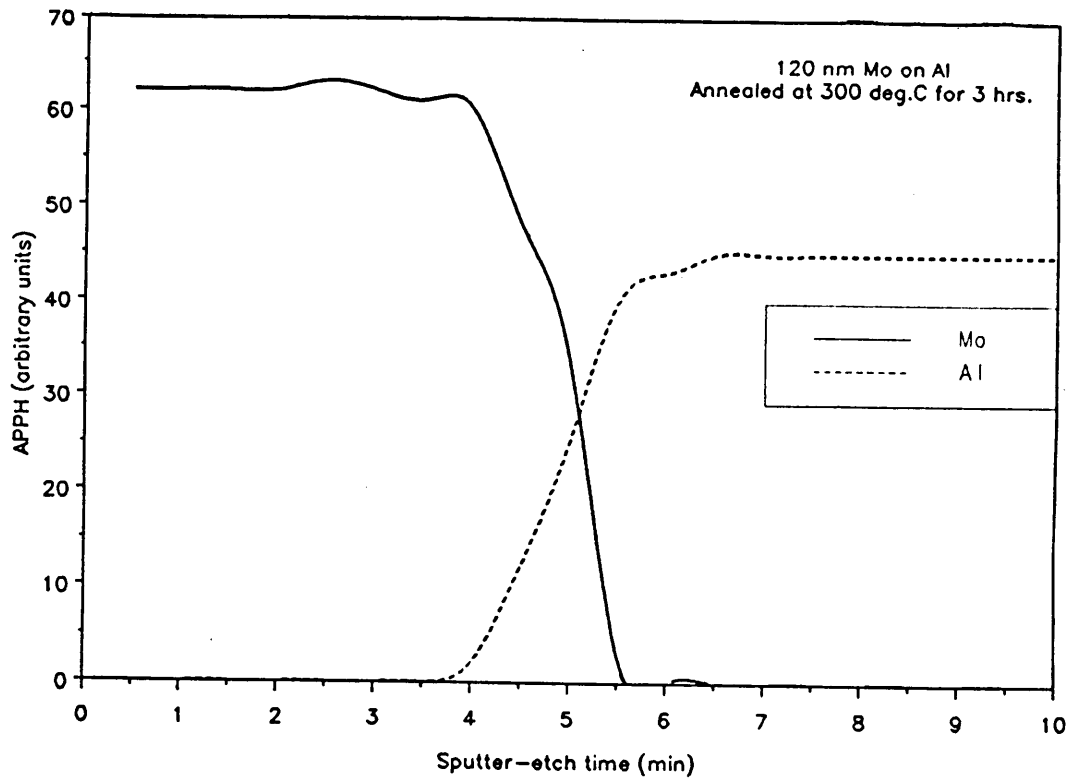


Figure 21. Measured APPH as a function of sputtering time for a bilayer film annealed at 350°C for 3 hours.: ~1200 Å Mo layer on Al layer.

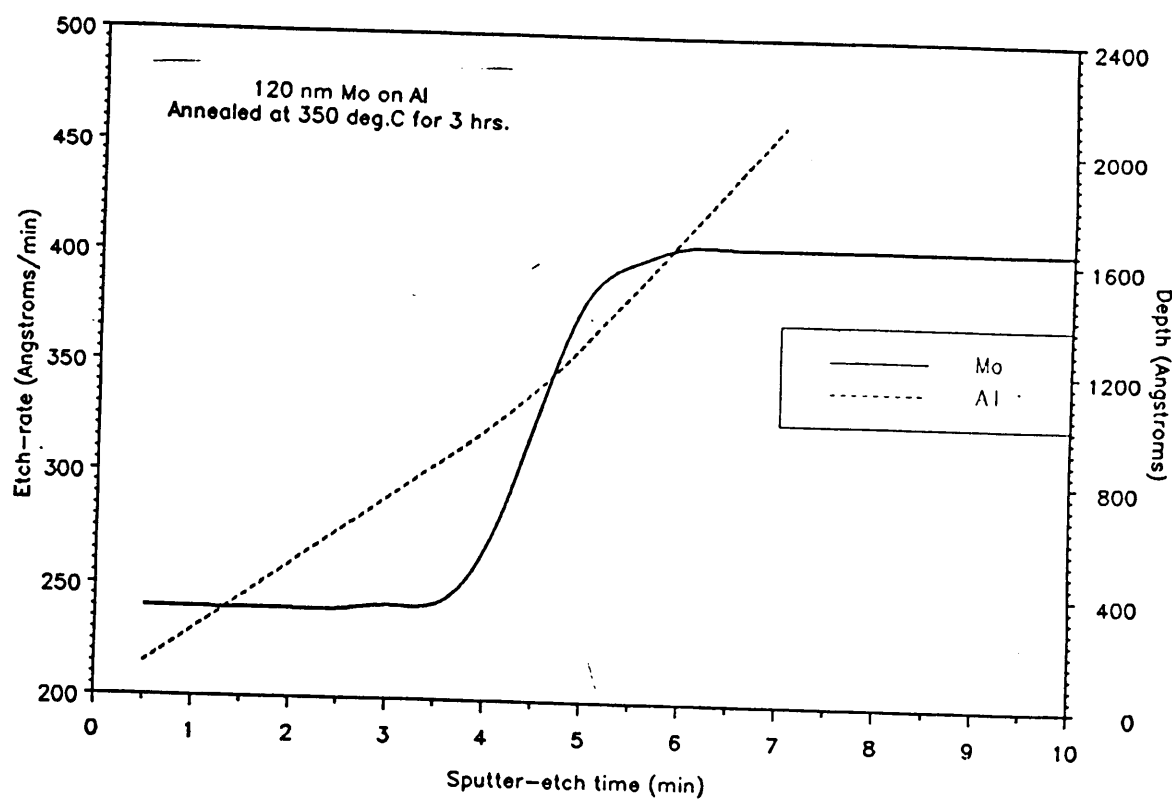


Figure 22. Sputter-etch rate and Sputter depth as functions of time for a bilayer film annealed at 350°C for 3 hours.: ~ 1200 Å Mo layer on Al layer.

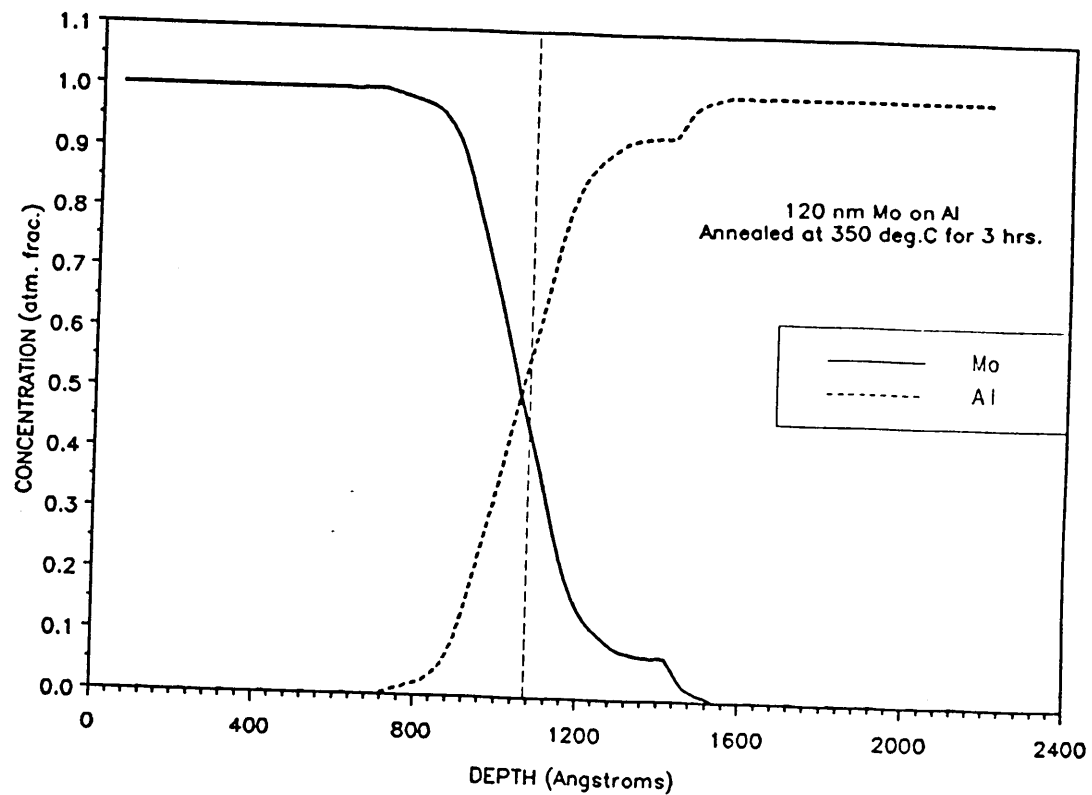


Figure 23. Bulk concentration versus depth profiles of Mo and Al in a bilayer film annealed at 350°C for 3 hours.: $\sim 1200 \text{ \AA}$ Mo layer on Al layer.

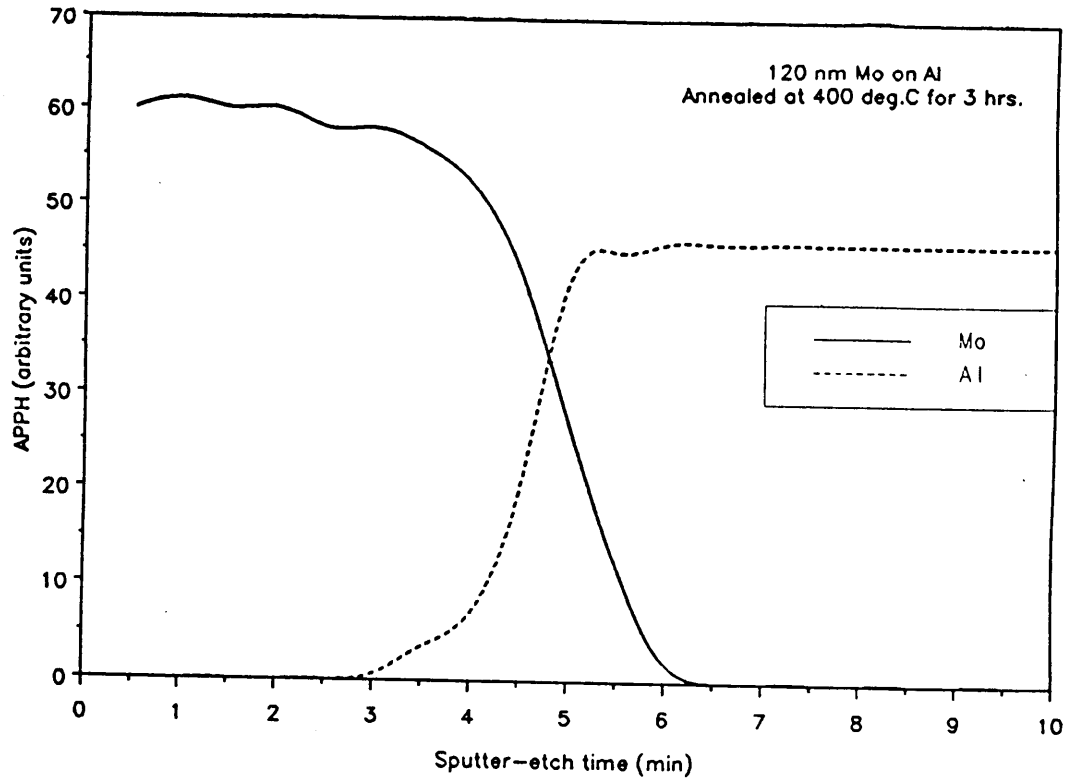


Figure 24. Measured APPH as a function of sputtering time for a bilayer film annealed at 400°C for 3 hours.: $\sim 1200 \text{ \AA}$ Mo layer on Al layer.

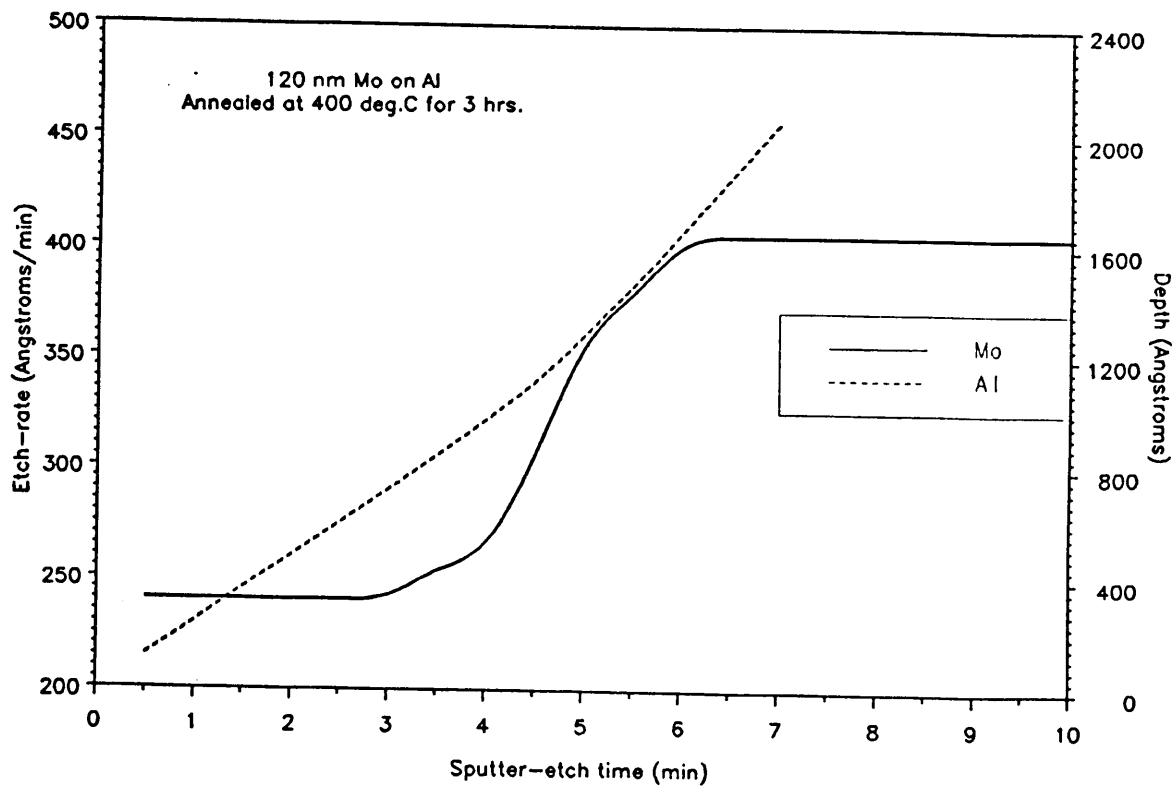


Figure 25. Sputter-etch rate and Sputter depth as functions of time for a bilayer film annealed at 400°C for 3 hours.: ~1200 Å Mo layer on Al layer.

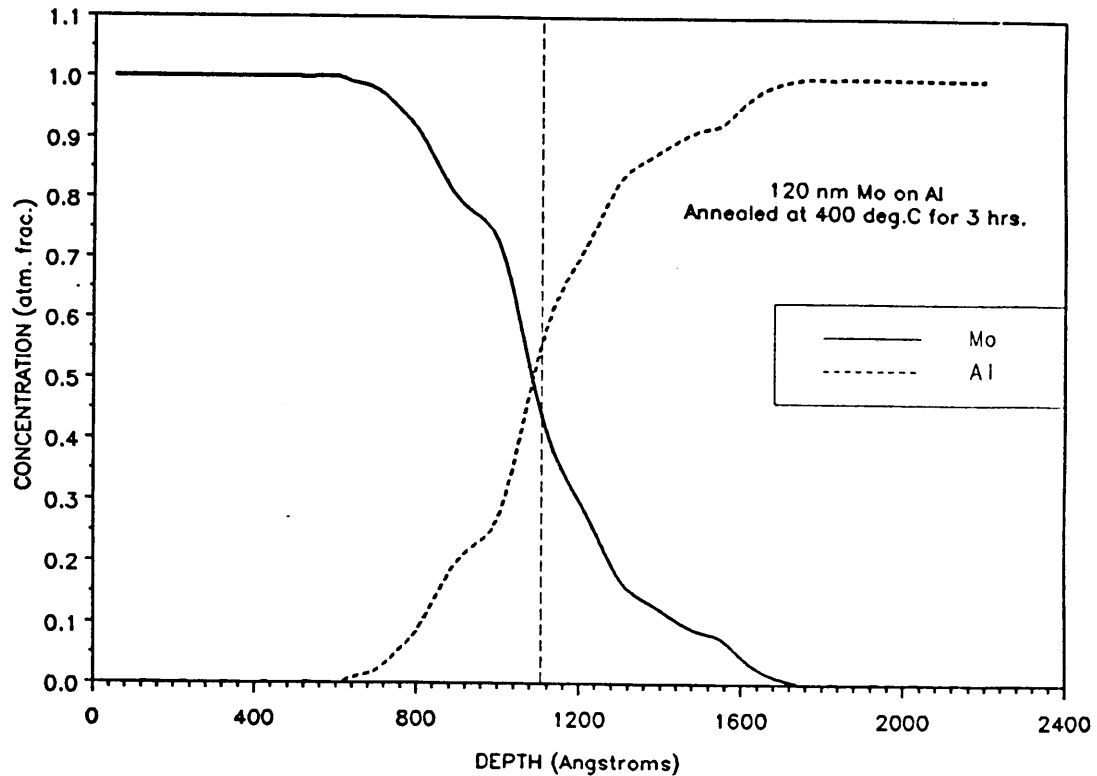


Figure 26. Bulk concentration versus depth profiles of Mo and Al in a bilayer film annealed at 400°C for 3 hours.: $\sim 1200 \text{ \AA}$ Mo layer on Al layer.

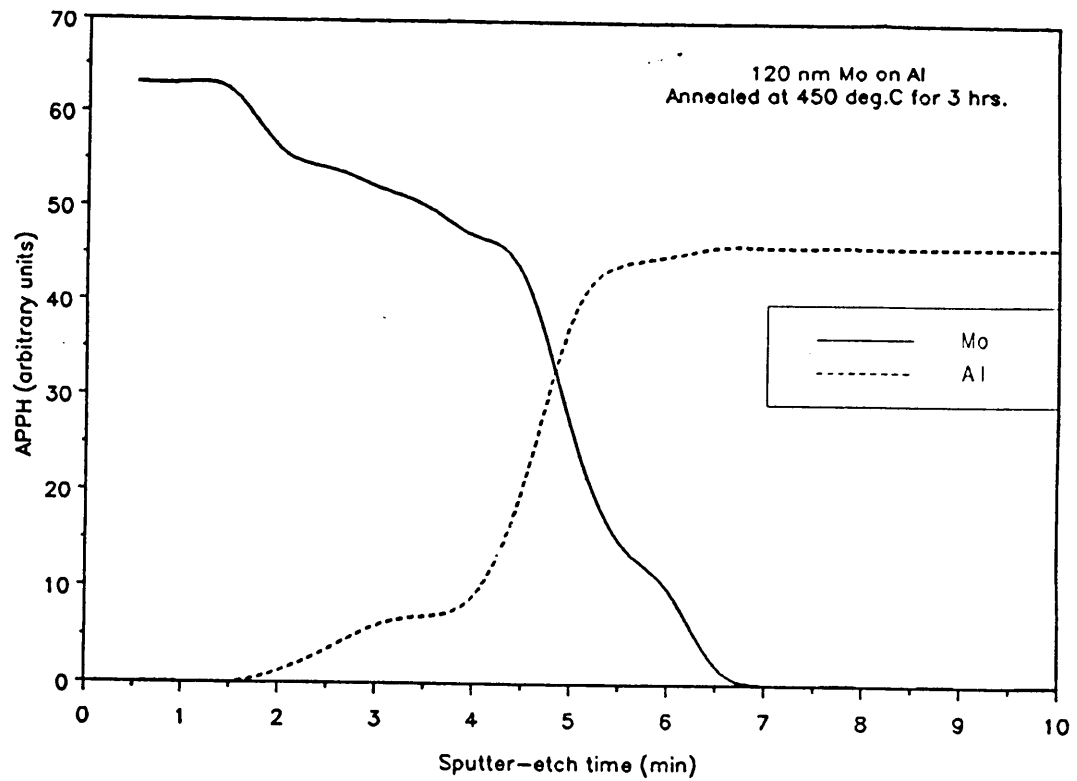


Figure 27. Measured APPH as a function of sputtering time for a bilayer film annealed at 450°C for 3 hours.: $\sim 1200 \text{ \AA}$ Mo layer on Al layer.

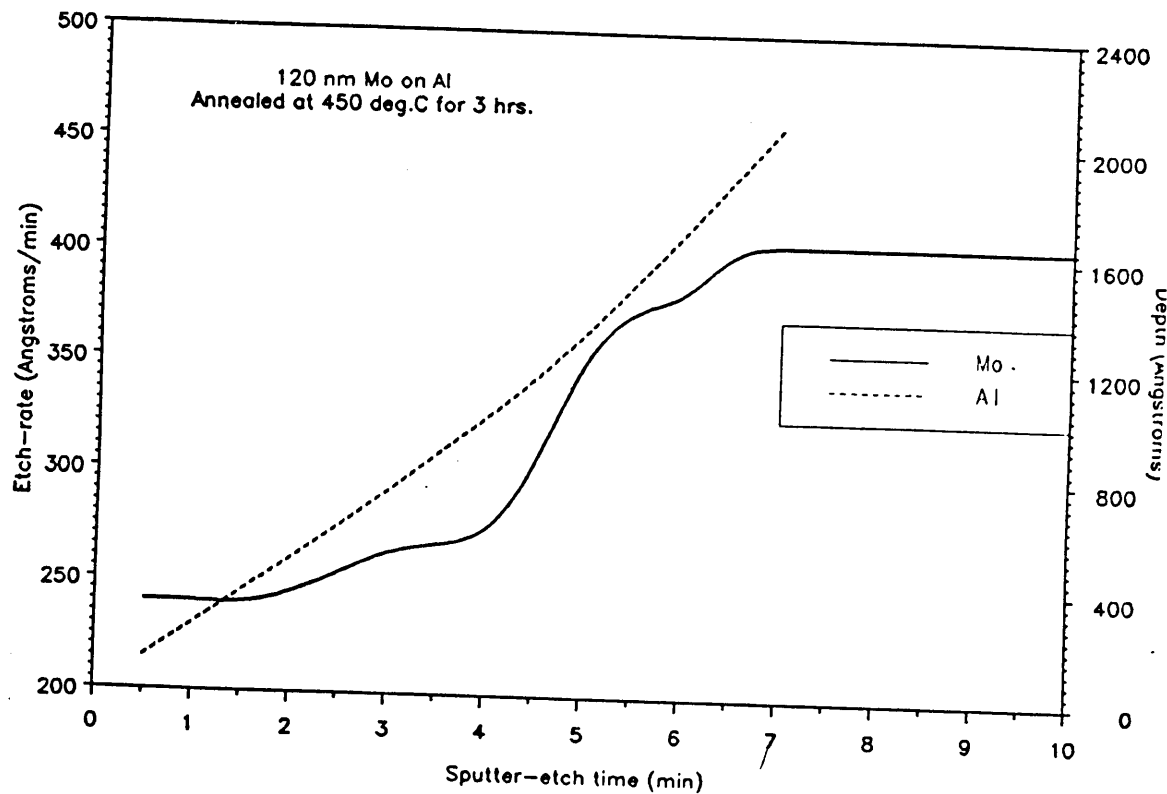


Figure 28. Sputter-etch rate and Sputter depth as functions of time for a bilayer film annealed at 450°C for 3 hours.: ~ 1200 Å Mo layer on Al layer.

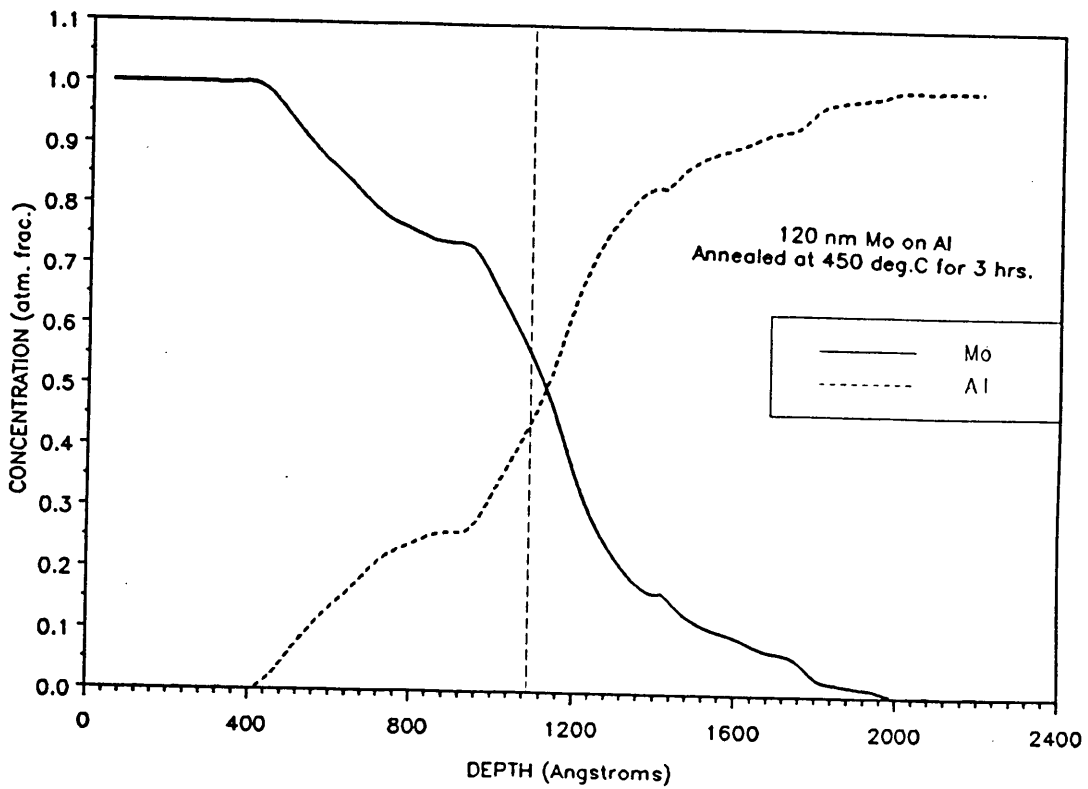


Figure 29. Bulk concentration versus depth profiles of Mo and Al in a bilayer film annealed at 450°C for 3 hours.: $\sim 1200 \text{ \AA}$ Mo layer on Al layer.

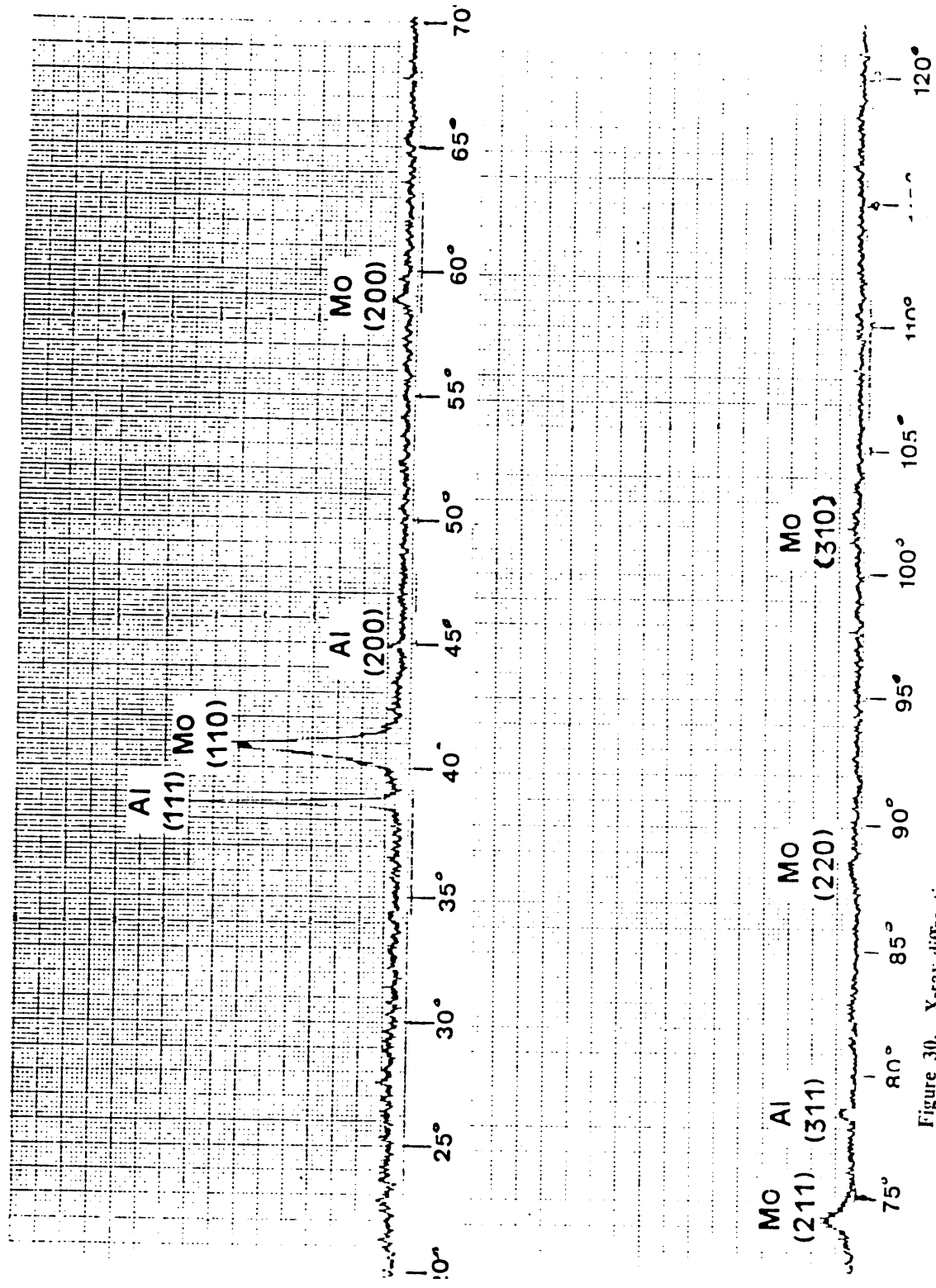


Figure 30. X-ray diffraction pattern (Intensity vs. 2 θ) of a Mo/Al bilayer thin film sample annealed at 300°C for 3 hours.

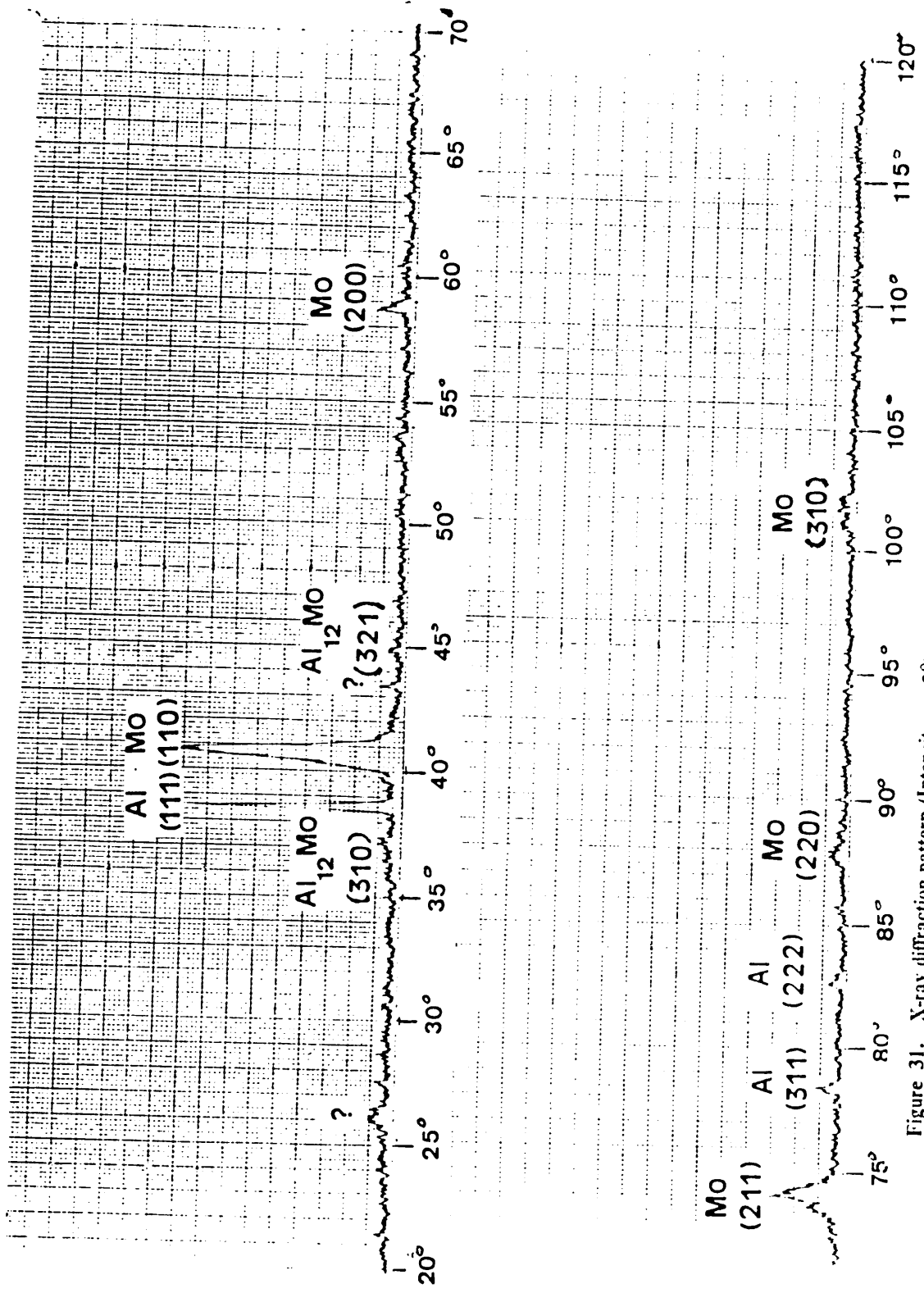


Figure 31. X-ray diffraction pattern (Intensity vs. 20) of a Mo/Al bilayer thin film sample annealed at 350°C for 3 hours.

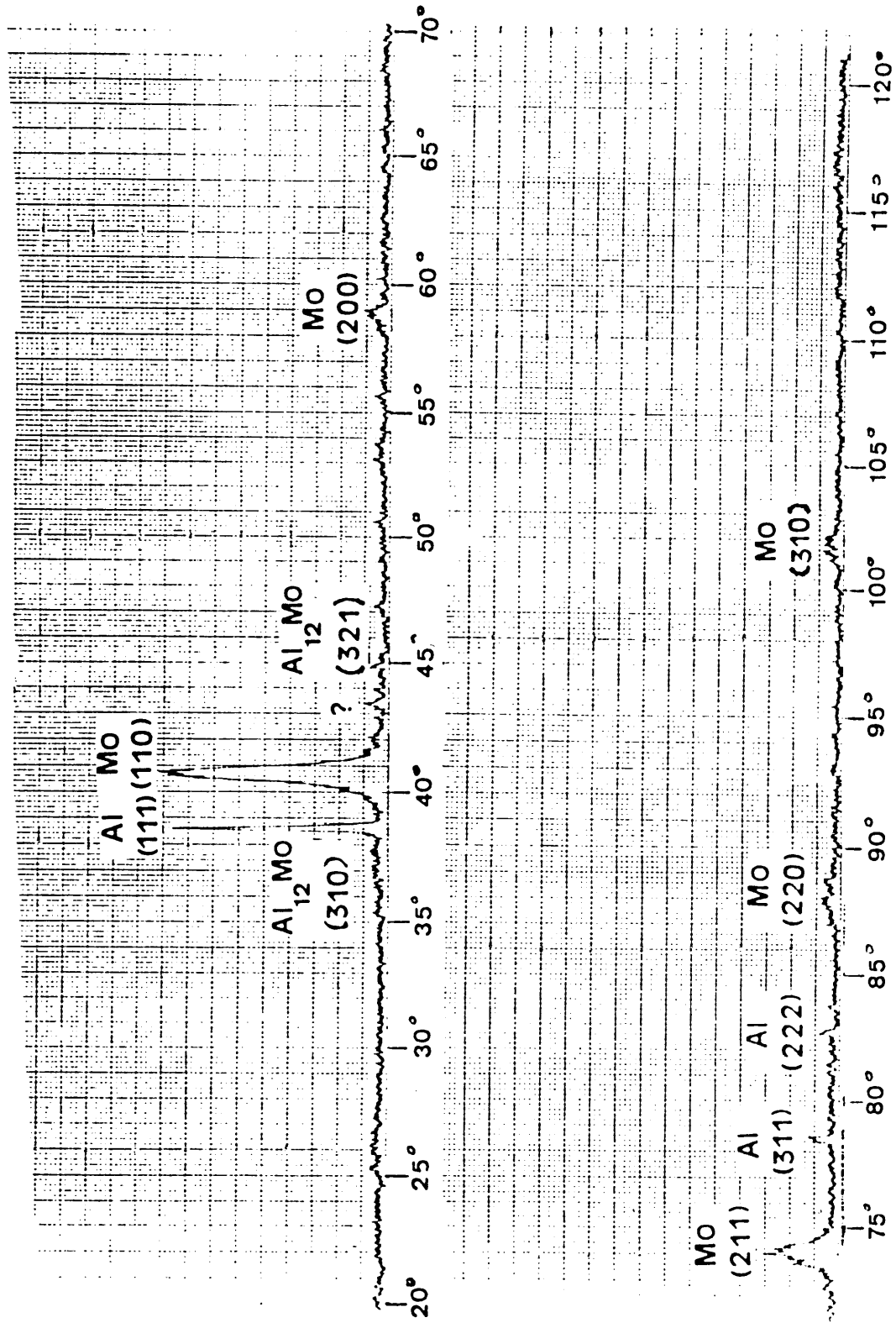


Figure 32. X-ray diffraction pattern (Intensity vs. 20) of a Mo/Al bilayer thin film sample annealed at 400°C for 3 hours.

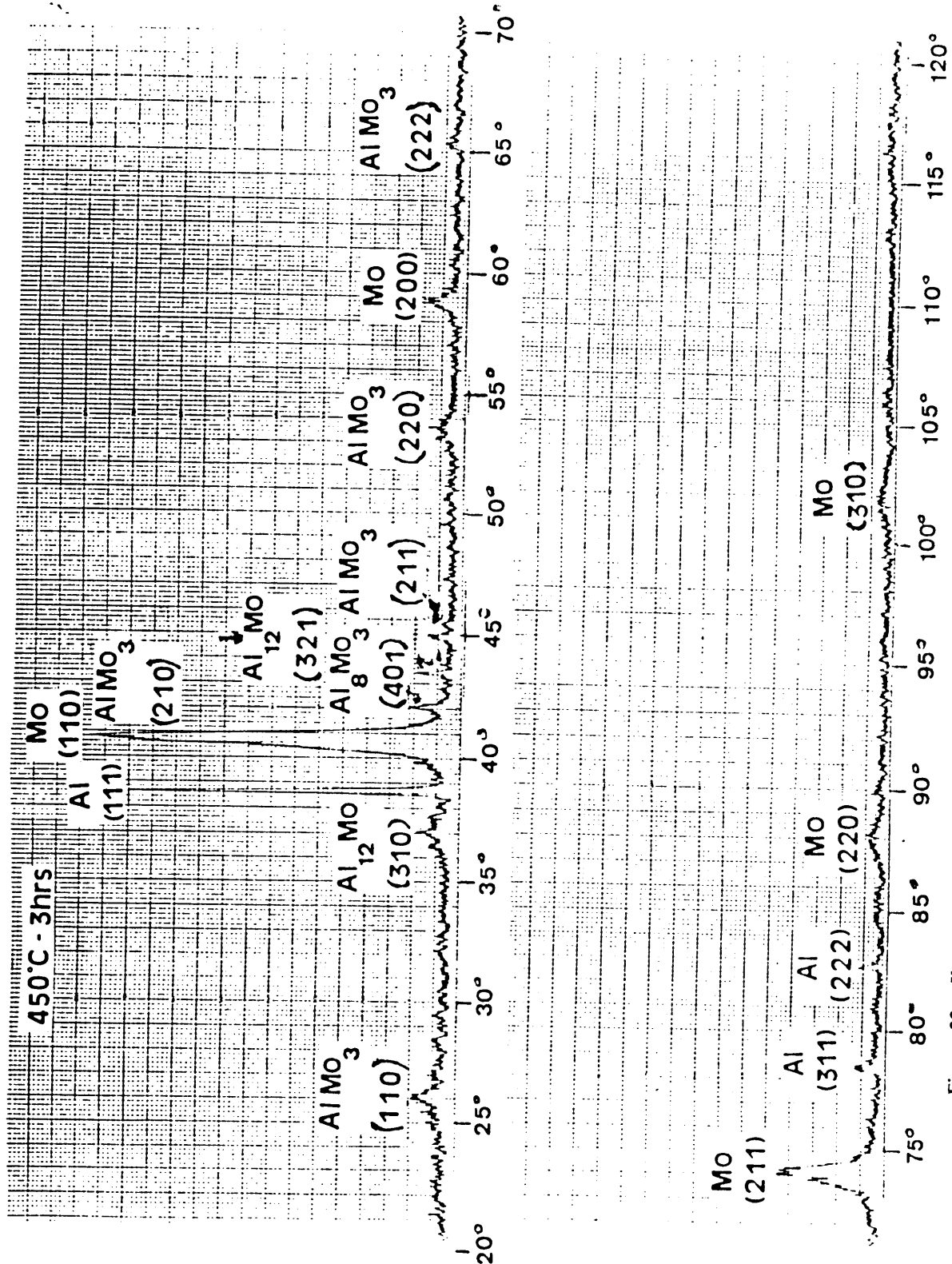


Figure 33. X-ray diffraction pattern (Intensity vs. 2θ) of a Mo/Al bilayer thin film sample annealed at 450°C for 3 hours.

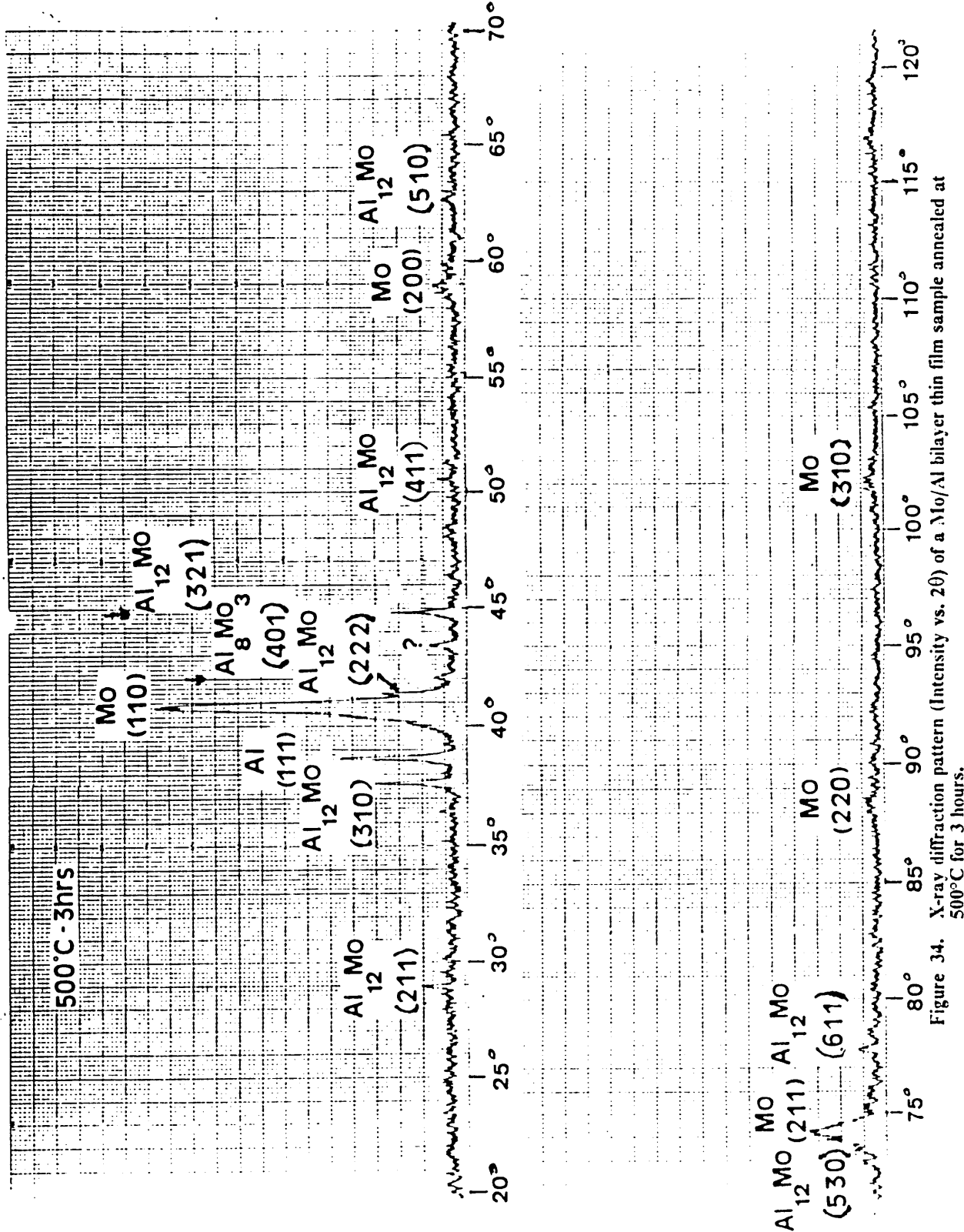


Figure 34. X-ray diffraction pattern (Intensity vs. 20) of a Mo/Al bilayer thin film sample annealed at 500°C for 3 hours.

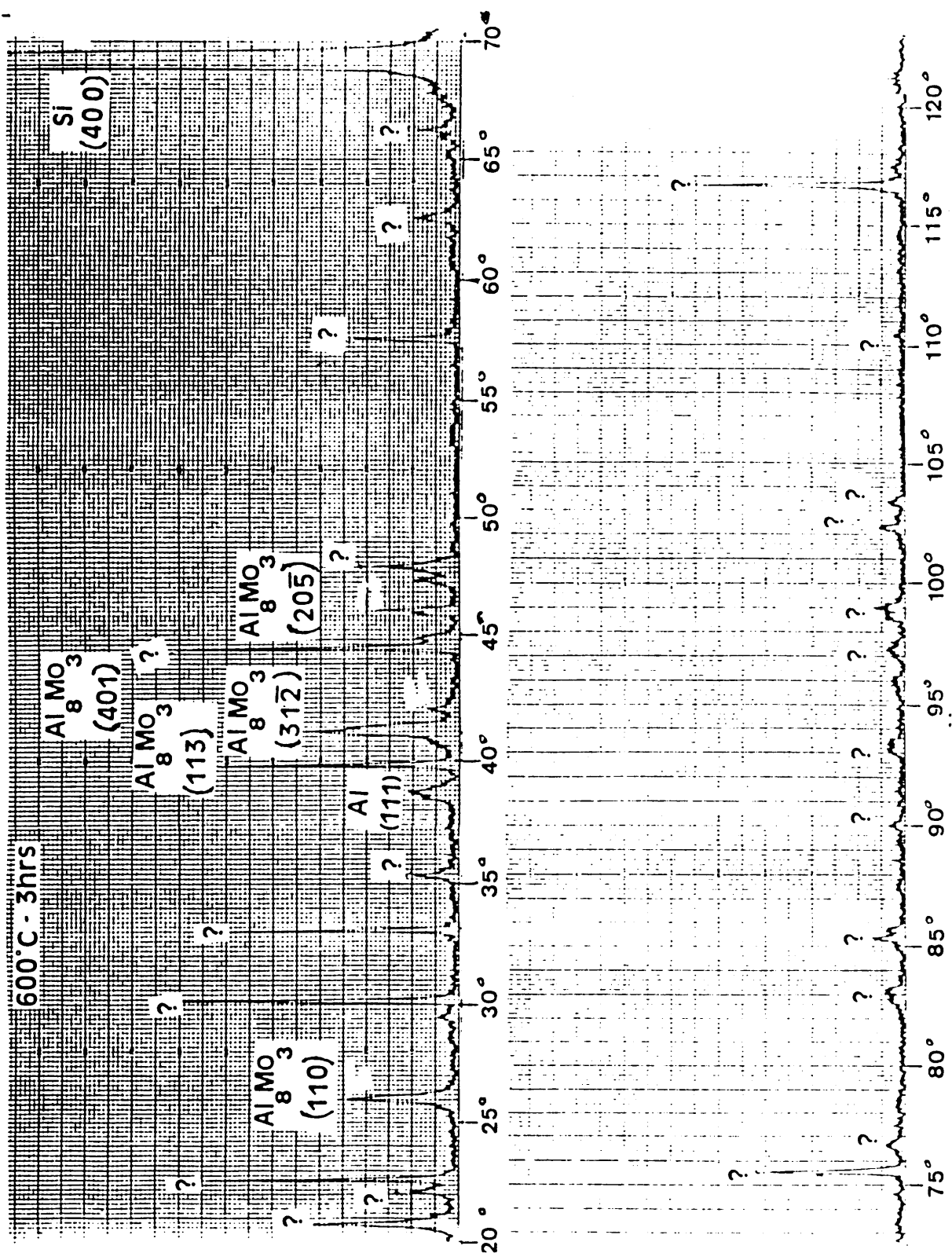


Figure 35. X-ray diffraction pattern (Intensity vs. 2θ) of a Mo/Al bilayer thin film sample annealed at 600°C for 3 hours.

Table 8. Diffraction data for intermetallics in Al-Mo.

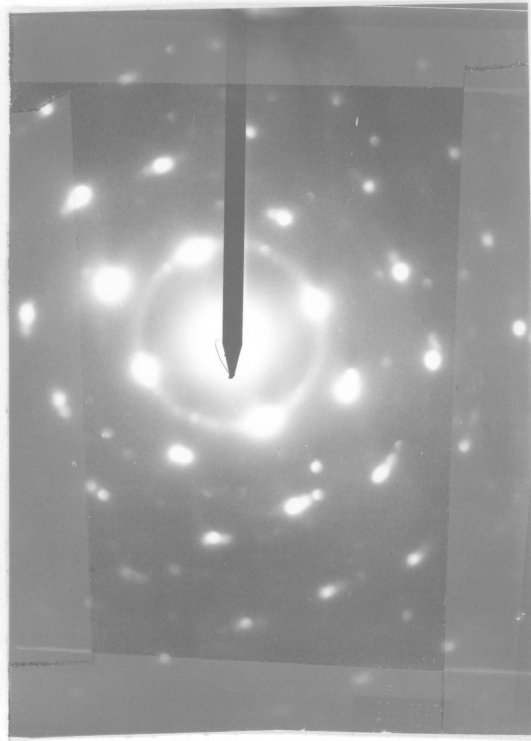
Four most prominent reflections and the observed reflections at different annealing temperatures [Cu-K_α radiation].

Compound	(hkl)	d-spacing	2θ	Rel.Inten.	2θ	Anneal.
		(Å)	(deg.)	(%)	(deg.)	Temp.
	(calc.)	(calc.)	(calc.)	(calc.)	(expt.)	(°C)
Al ₁₂ Mo	(310)	2.3975	37.482	100.0	37.60	≥ 350
	(321)	2.0262	44.686	93.5	44.78	
	(110)	5.3609	16.522	74.6	16.67	
	(222)	2.1886	41.212	47.5	41.35	
Al ₅ Mo	(112)	2.137	42.26	100.0		
	(101)	3.816	23.29	71.0		
	(110)	2.445	36.73	28.0		
	(004)	2.200	40.99	27.0		
Al ₄ Mo	(241)	2.1789	41.404	100.0		
	(042)	2.2226	40.555	95.5		
	(130)	3.8921	22.829	76.5		
	(111)	3.9344	22.581	71.4		
Al ₈ Mo ₃	(113)	2.2798	39.494	100.0	39.82	≥ 600
	(312)	2.2284	40.445	99.3	40.97	
	(401)	2.1199	42.612	42.8	42.23	
	(110)	3.3750	26.385	40.0	26.04	
AlMo ₃	(210)	2.2137	40.725	100.0	40.89	≥ 450
	(211)	2.0208	44.812	31.3	45.42	
	(520)	0.9192	113.86	29.0	113.2 ?	
	(110)	3.5002	25.426	22.4	25.93	

tendency for epitaxial growth of metallic grains and the grains of intermetallic compounds. If the interfaces tend to be coherent at the area of contact of these grains, lattice distortion and associated coherency strains could be expected to be present. The TEM sample contains layers that are ultra-thin and it is generally found that for ultra-thin coatings the deposit tends to form coherent interface with the substrate layer.

Uniquely indexing the rings of a ring pattern becomes difficult for patterns obtained from samples annealed at higher temperatures where several phases can possibly coexist and may lead to overlapping of very closely spaced rings that are difficult to resolve. This makes the identification of phases using conventional electron diffraction techniques difficult. Convergent beam techniques and operation of the TEM in the nanoprobe mode instead of the microprobe mode may be helpful in obtaining unambiguous diffraction information from very small single phase regions in the sample. Electron diffraction patterns obtained at temperatures above 450°C are too complicated to be analysed completely. Further different regions gave different complicated patterns which called for a very detailed examination with the TEM beyond the scope of the present work. Only the most commonly observed patterns are presented here.

Samples annealed at 450°C showed a somewhat different microstructure as can be seen from the TEM micrograph. The Mo grains had grown larger and few. The electron diffraction pattern and the X-ray diffraction pattern confirm the formation of AlMo₃ compound and the growth of Al₁₂Mo. AES profile also showed a clear discontinuity at approximately 75 atomic % Mo. Samples annealed at temperatures higher than 450°C were not analysed by AES. Diffraction techniques showed the formation of larger amounts of Al₁₂Mo and some Al₈Mo₃ but no detectable AlMo₃ for a sample annealed at 500°C for 3 hours. X-ray diffraction spectra of a sample annealed at 600°C for 3 hours showed peaks corresponding to Al₈Mo₃ and some more reflections that could not be identified. These unidentifiable reflections did not match with the simulated powder diffraction patterns for the several intermetallics. These peaks could be due to the compound Al₆Mo for which no lattice parameter data or structural data was available or due to the formation of some new unknown compound. There was a single peak at $2\theta = 43.4^\circ$ that could not



ring 1 Mo(110)

ring 2 Mo (200)

Figure 36. Bright field image and electron diffraction pattern of a bilayer film annealed at 300°C for 3 hours.: BFI. ($\times 490000$) EDP [$L = 758.5\text{mm}$ calib.(660mm setting)]



ring 1 Al_{12}Mo (211)

ring 2 Mo (110)

ring 3 Mo (200)

Figure 37. Bright field image and electron diffraction pattern of a bilayer film annealed at 350°C for 3 hours.: BFI. ($\times 490000$) EDP [$L = 758.5\text{mm}$ calib.(660mm setting)]

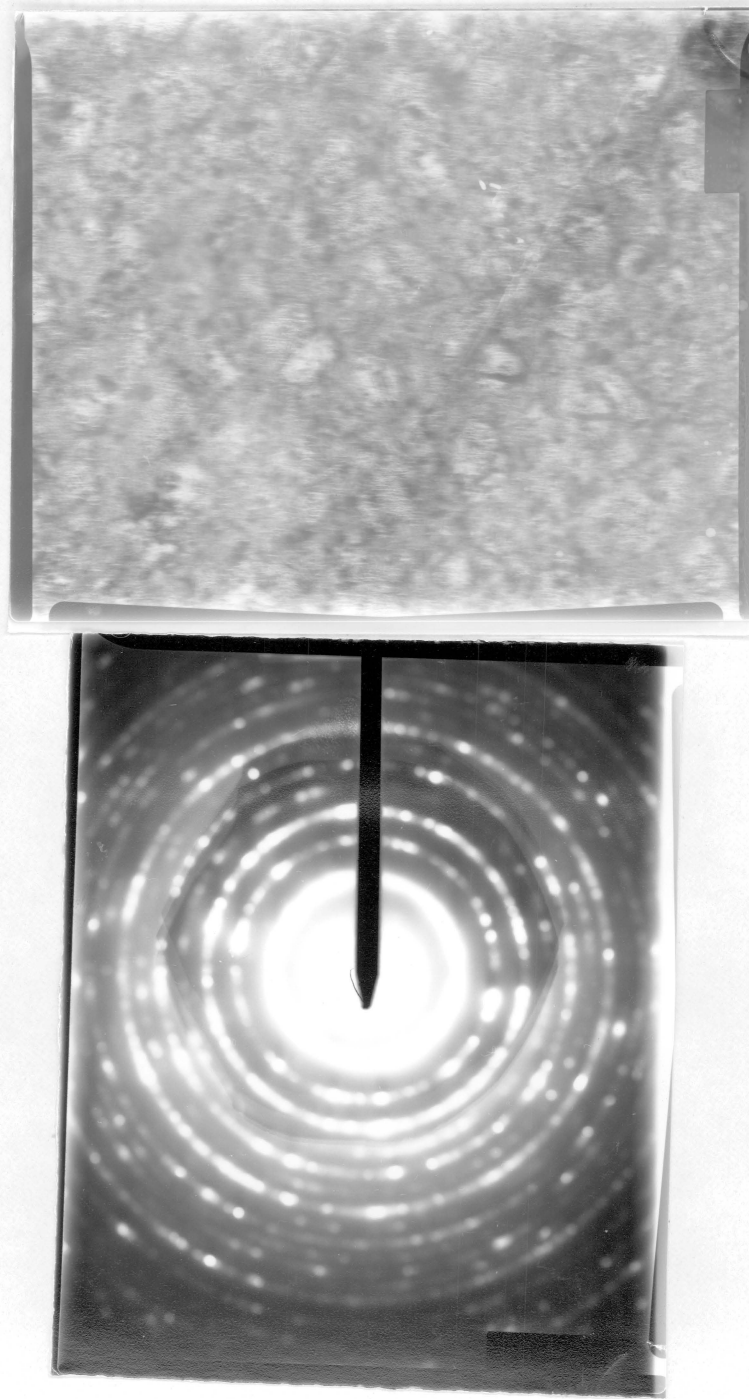
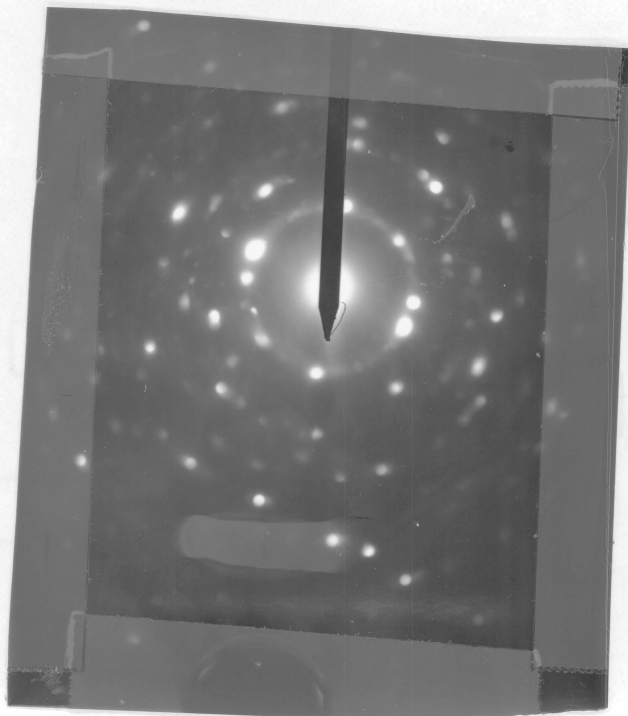
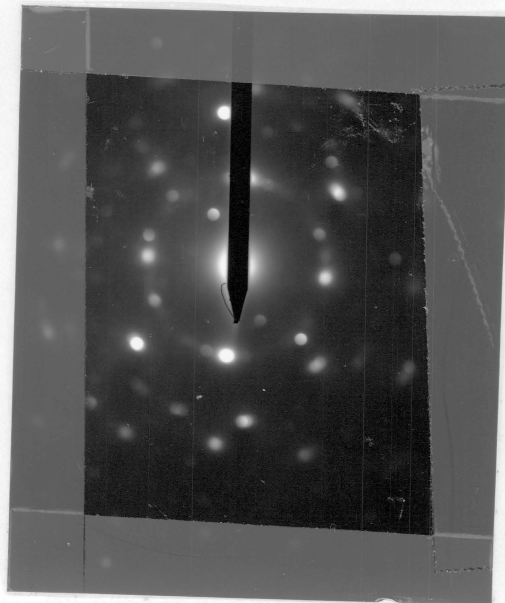


Figure 38. Bright field image and electron diffraction pattern of a bilayer film annealed at 400°C for 3 hours.: BFI. ($\times 490000$) EDP [$L = 758.5\text{mm}$ calib.(660mm setting)]



ring 1 Mo (110)
ring 2 Mo (200)

Figure 39. Bright field image and electron diffraction pattern of a bilayer film annealed at 450°C for 3 hours.: BFI. ($\times 490000$) EDP [$L = 758.5\text{mm}$ calib.(660mm setting)]



ring 1 Al_{12}Mo (211)
ring 2 Mo (110)
ring 3 Mo (200)

Figure 40. Bright field image and electron diffraction pattern of a bilayer film annealed at 500°C for 3 hours.: BFI. ($\times 490000$) EDP [L = 758.5mm calib.(660mm setting)]

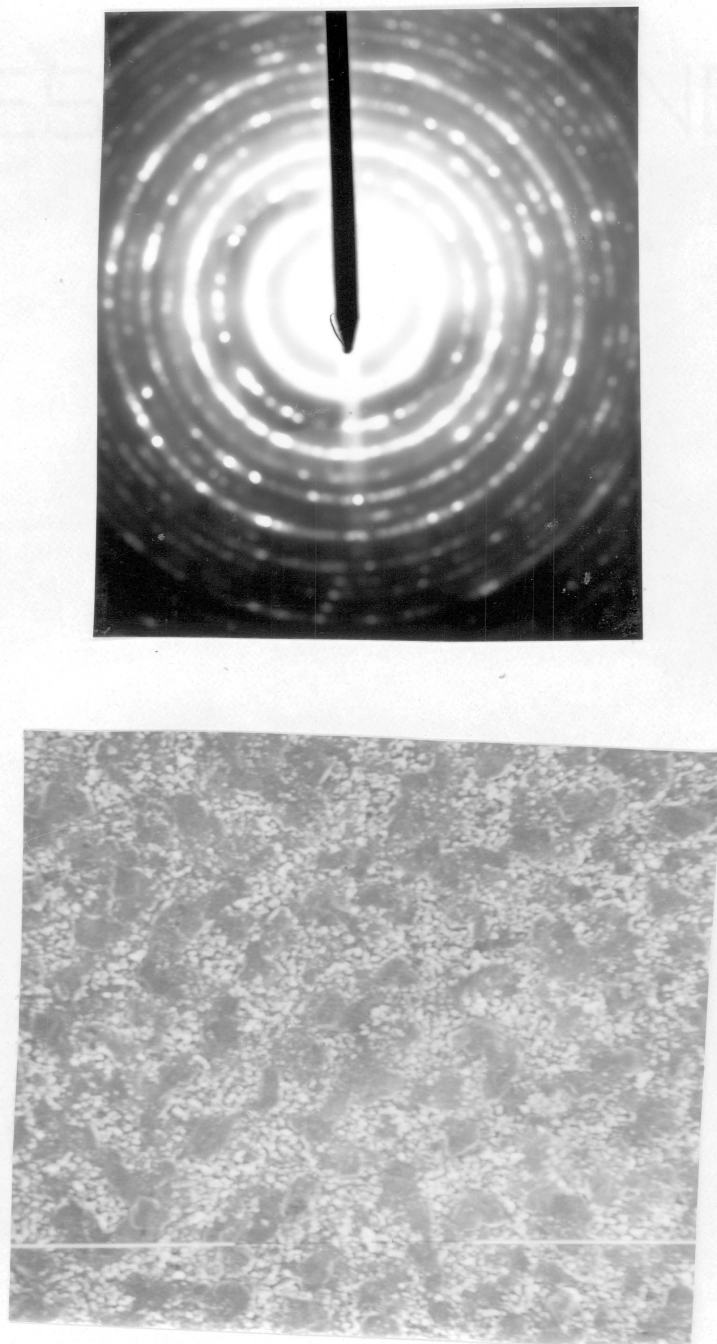
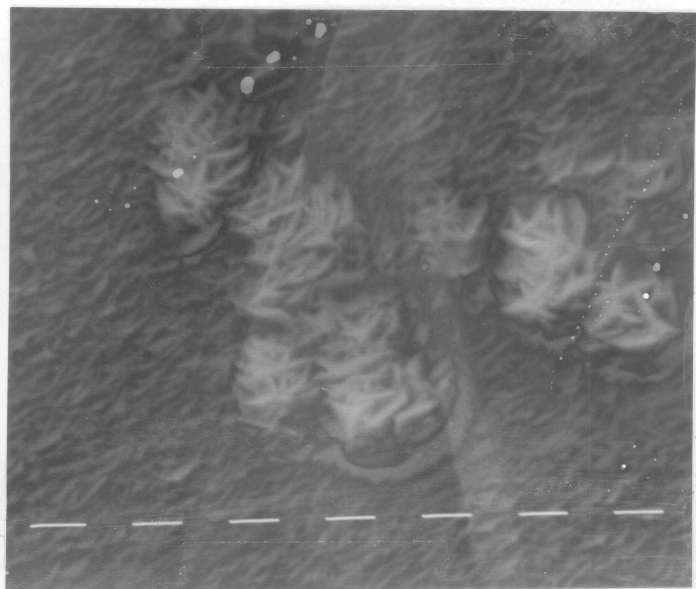


Figure 41. Bright field image and electron diffraction pattern of a bilayer film annealed at 600°C for 3 hours.: BFI. ($\times 490000$) EDP [L = 758.5mm calib.(660mm setting)]

be indexed which started appearing at 350°C and grew in intensity with increasing annealing temperature.

The surfaces of the annealed bilayer samples were examined in the SEM mode of EM420 STEM. The SEM micrographs of the surfaces are presented in Figure 42 on page 111 to Figure 46 on page 115. In most cases the surface was covered with a somewhat discontinuous oxide film with the metal lying beneath the oxide. Since the surface of pure Mo film was completely featureless, it is imagined that as result of the heat treatment, this oxide layer was formed. It is also possible that some of the Al in the lower layer diffused up to the surface through grain boundaries because of its affinity for oxygen. This is evident in the micrograph of the multi-layer sample surface with a 200 Å Mo top layer through which Al from the next layer below seems to have diffused to the surface to get oxidized.

To determine the diffusion coefficients for self-diffusion of Al in Mo and Mo in Al, the AES composition profiles were analyzed first to determine the chemical interdiffusion coefficient D at concentrations of less than or equal to 6 atomic% on both the Al side and the Mo side using the Matano solution for the interdiffusion problem in which the two materials form a semi-infinite diffusion couple with accompanied additional intermetallic phase formations. Matano method can be applied to these single phase regions with a continuous composition profile and a one-dimensional concentration gradient. The interdiffusion coefficients were calculated from the AES composition-depth profiles using Equation 46 in Chapter 3. Graphical integration was done using a sensitive electronic planimeter to fix the Matano interface position and to estimate the integral in Equation 46 for the four different temperatures 300, 350, 400 and 450°C. It was found that for compositions lower than 6 atomic% the interdiffusion coefficient did not depend on concentration. Using Darken's equation (Equation 47), the lattice diffusivities D_{Mo} and D_{Al} were estimated from D measured at 3 atomic% Mo and 3 atomic% Al respectively. The values of D_{Mo} and D_{Al} obtained at the four different temperatures (300, 350, 400 and 450°C) were fit to a straight line to obtain an Arrhenius type relation between the lattice diffusivity and temperature for Mo and



=
Figure 42. Surface topography of a Mo/Al bilayer film: SEM image with SED. [$\times 50000$; $0.5\mu\text{m}$ marker]

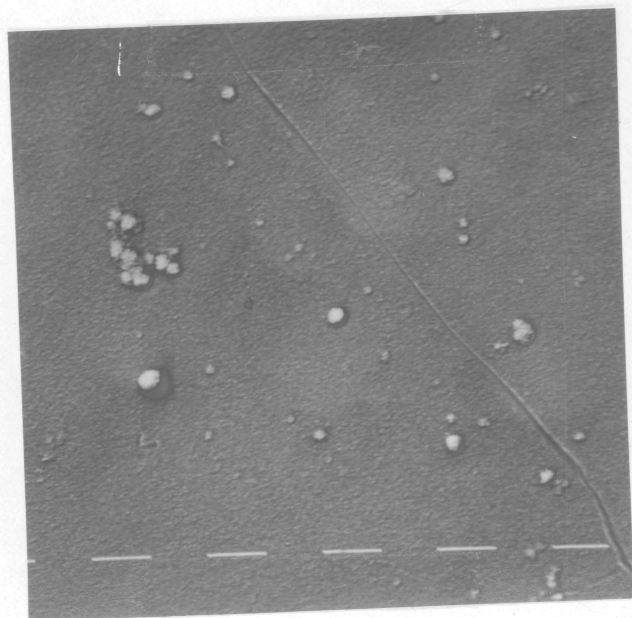


Figure 43. Surface topography of a Mo/Al bilayer film: SEM image with SED. [$\times 50000$; $0.5\mu\text{m}$ marker]

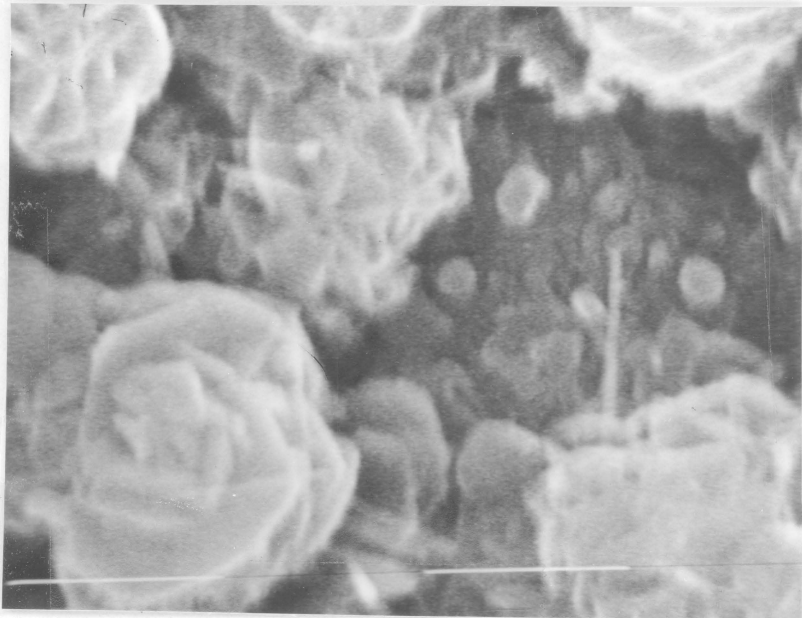


Figure 44. Surface topography of a Mo/Al bilayer film: SEM image with SED. [$\times 50000$; $0.5\mu\text{m}$ marker]

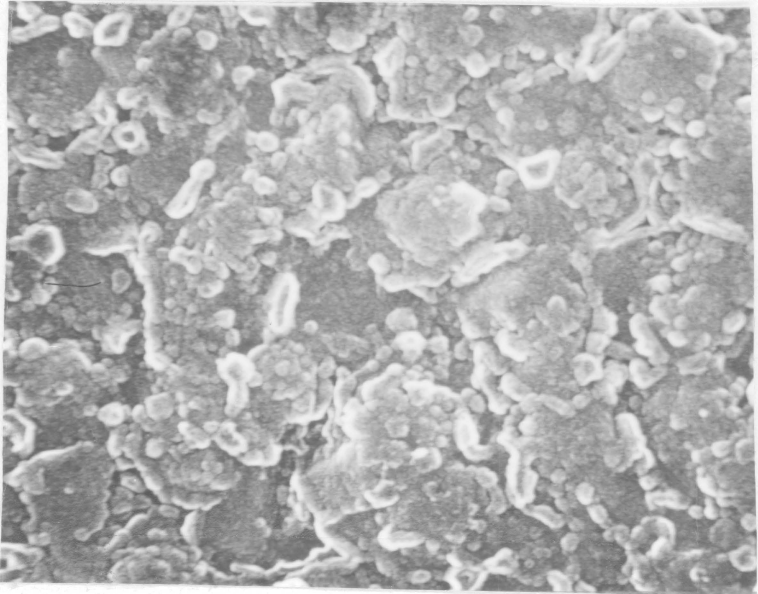


Figure 45. Surface topography of a Mo/Al bilayer film: SEM image with SED. [$\times 50000$; $0.5\mu\text{m}$ marker]

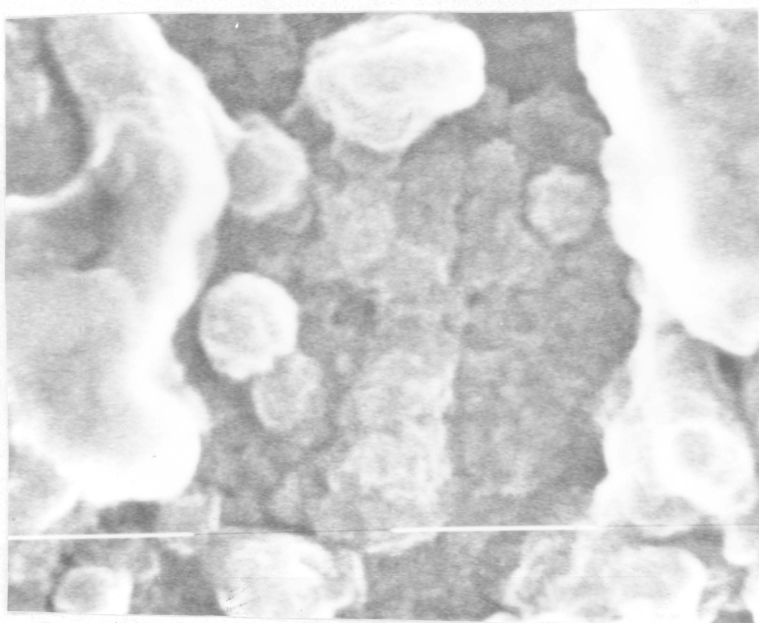


Figure 46. Surface topography of a Mo/Al bilayer film: SEM image with SED. [$\times 50000$; $0.5\mu\text{m}$ marker]

Al. The plots of D_{Mo} versus $(1000/T)$ and D_{Al} versus $(1000/T)$ are presented in Figure 47 on page 117 and Figure 48 on page 118 respectively. Though the fit for Mo appears to be reasonably good, data for Al diffusivity appears scattered. This could be due to the finer grain size of Mo compared with Al layer. The figure for Mo lattice diffusivity also contains the Arrhenius type relations obtained for Mo diffusion in Al by two different independent investigations reported in the literature. One of the studies [31] involved bulk diffusion studies with 0.2 to 0.3 weight% Mo in Al alloy sandwiched between pure Al. This study was carried out at temperatures close to the melting point of Al (625 to 655°C) and the samples were analysed by ESMA technique. The other investigation was on the tracer diffusivity of Mo in polycrystalline Al in the temperature range of 400 to 600°C [62]. The values of D_0 , the pre-exponential factor and Q , the activation energy for diffusion from the present and the other two investigations are tabulated in Table 9 on page 119.

The activation energy obtained in the present investigation is comparable but slightly lower than the one obtained for tracer diffusion but is much lower than the value reported for bulk impurity diffusion in alloys. This may be explained by the fact that bulk diffusion studied by Chi [31] at temperatures close to the melting point of Al combined with the ESMA technique measures the diffusion of Mo in Al in conditions under which the dominating mechanism of diffusion is pure volume diffusion which has a much higher activation energy than diffusion involving short-circuit paths such as grain boundary, dislocation pipes etc. The large concentrations of such short-circuit paths exist in thin films especially in the type of fine-grained thin films used in the present investigation. Also the lower temperature range used in the present study leads one to expect diffusion through short-circuit paths to be the predominant mechanism.

The low Q value obtained in the present investigation is closer to the one obtained for tracer diffusion in polycrystalline Al in a similar temperature range because the conditions under which the diffusion process was studied are somewhat similar with probably short-circuit diffusion dominating over volume diffusion. The still lower value of Q can be related to the relative abundance of short-circuit paths in the microcrystalline bilayer thin films compared to a normal polycrystalline specimen.

LATTICE DIFFUSIVITY OF Mo IN Al

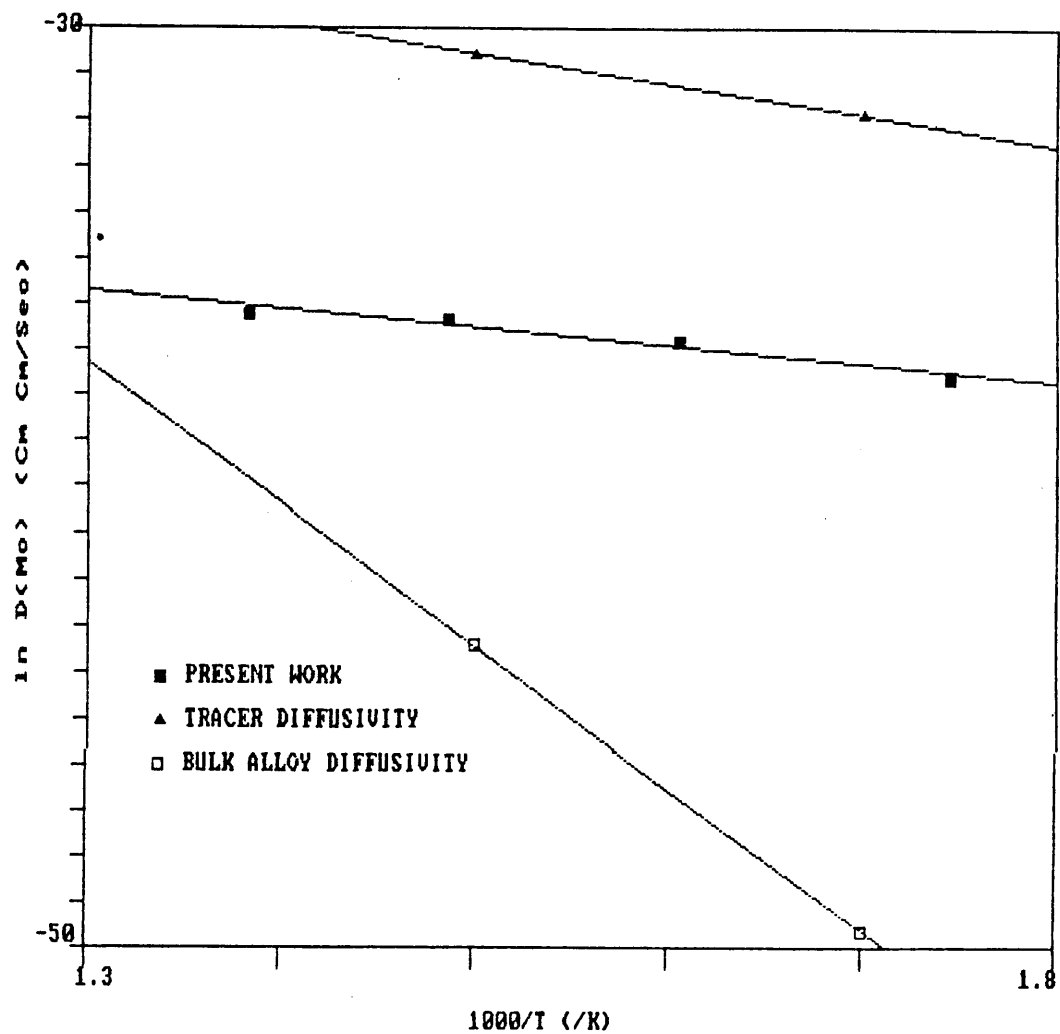


Figure 47. $\ln(D_{Mo})$ as a function of $(1000/T)$

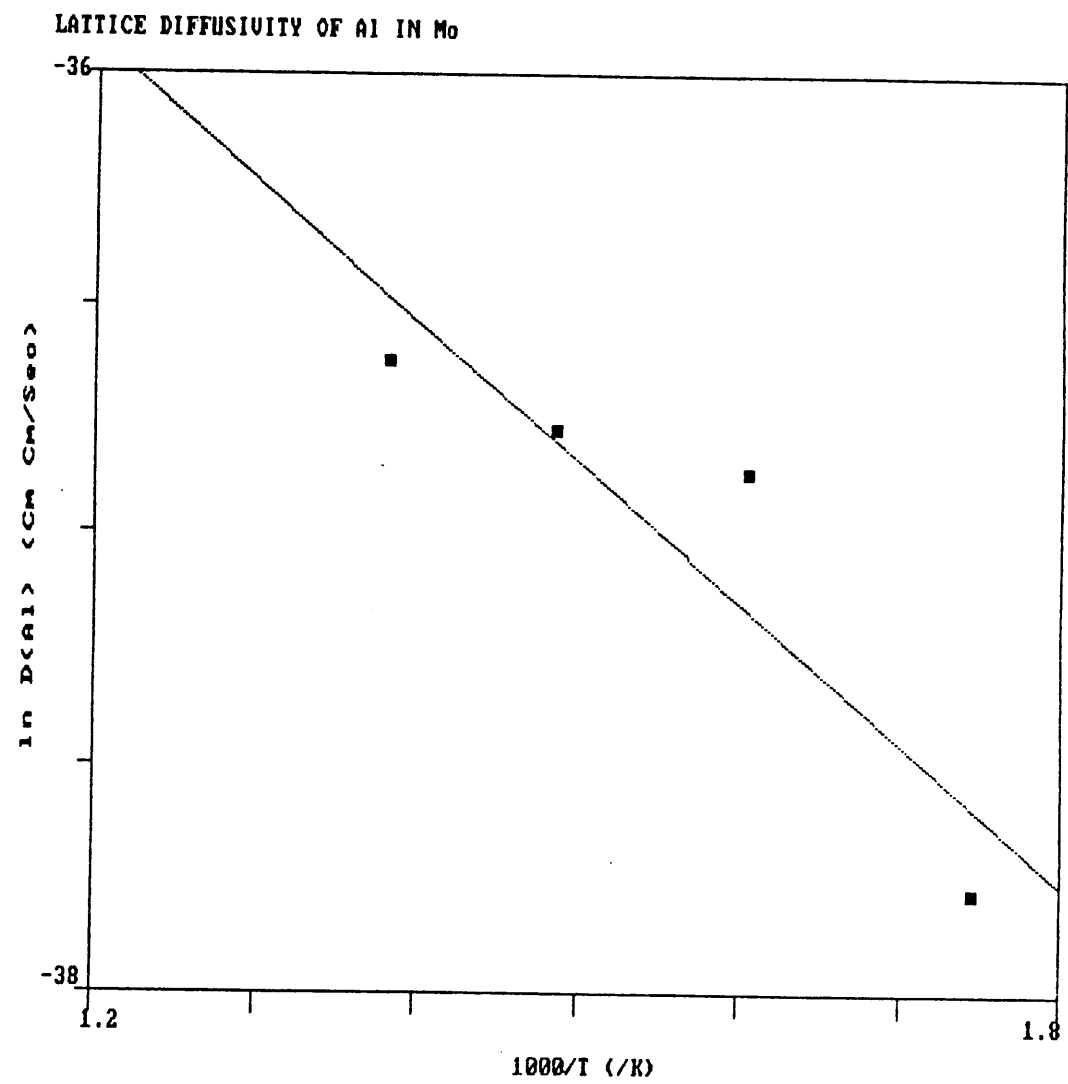


Figure 48. $\ln(D_{Al})$ as a function of $(1000/T)$

Table 9. D₀ and Q values for diffusion of Mo into Al.

Source	D ₀ cm ² /sec	Q kcal./mole
Tracer Diffusivity [Ref.62]	1.04×10^{-9}	13.1
Bulk Diffusion [Ref.31].	18^{+46}_{-8}	60 ± 4
Present Study [Thin film]	5.56×10^{-14}	7.958

A comparison of the actual values of diffusion coefficients obtained all three investigations shows that the results of the present study are one order of magnitude higher than

bulk alloy measurements of Chi [31] and two orders of magnitude lower than the tracer diffusivity values. These differences are the result of the very low D_0 value obtained in the present investigation. This low value may be the result of the analysis technique used in the present study; i.e., the use of AES sputter profiling method. The accuracies of the diffusion coefficient and other rate constants measured in the present investigation depend on the validity of the assumptions made for deriving the Equations 4-6 of Chapter 3 and also on possible experimental errors. In Equation 6, the alloy or compound sputter-etch rate was related to the experimentally measured rates for pure metals neglecting any alloying effects. It could be that the compounds sputter at a very different rate compared to metals because of structural and chemical environment differences. If this is so, the error introduced in the sputtering rate would reflect finally in the value obtained for the pre-exponential factor D_0 but should have no effect on the calculated value of activation energy Q . Since quite a few intermetallics were observed upon annealing, it is possible that the estimated depth-time relation for the sputtering process is not followed faithfully. So, the differences in D_0 values could result from measurement errors, but could also arise from the different specimen-preparation conditions.

5.2 *Results for Mo/Al Multilayers*

First, the Mo/Al multilayers were deposited with no substrate bias being applied. The expected layer thicknesses of each Mo and Al layer were to be 200 Å and 60 Å respectively for two different sets of samples. The first sample was to be examined by RBS and AES methods because of the larger layer thickness which brings the possible satellite X-ray peaks too close to the main reflection for investigation with X-rays. The second sample is not suitable for either RBS or AES composition profiling because of the limited depth resolutions of these techniques but is ideally suited for x-ray diffraction investigation through analysis of super-lattice satellite re-

flections and low-angle reflections around the main beam (000) reflection. Results of RBS analysis of the 200 Å layer thickness multilayer film is presented in Figure 49 on page 122 and Table 10 on page 123. The results show that the film has poor layering characteristics with no sharp interfaces. Though no bias was used, it is possible that the Al layers deposited in islands with a lot of discontinuities and pores as has been observed in the case of deposition of pure Al films. Even if the Mo layers deposit uniformly on the lower Al layer the poor structure of the bottom-most Al layer and the subsequent ones would add up and result in very poor interface quality. Also, since a conventional diode source was used for deposition, substrate and growing film are not decoupled from the plasma but are subjected to bombardment of energetic particles which would further deteriorate the interface quality.

Figure 50 on page 124 and figref refid=fig48. show simulated x-ray diffraction peak positions with relative intensities without any broadening arising from ideal multilayers of layer thickness 200 Å and 60 Å examined with Cr-K α radiation. X-ray diffraction investigation of the 60 Å layer thickness multilayer sample showed no satellite peaks at all around any of the higher order peaks. Couple of weak reflections were observed in the low-angle region which indicated presence of composition modulations in the film but the peaks were very asymmetric and the 2θ positions did not correspond to the expected positions for the 60 Å multilayer structure. It is necessary to have a coherent modulation whose repeat wavelength does not vary more than 10% from the mean value, to be able to observe satellite peaks and multilayer diffraction effects from a multilayer. The low angle peaks however are sensitive only to the chemical or structure factor modulation on a broader scale may still appear even if the interface quality is very poor. This was the case with the multilayer films deposited during the present investigation of layered films.

Attempts to deposit multilayer films with the substrate bias being applied to improve the quality of Al layers did not result in better interface quality. This was due to the ion-beam mixing effect at the surface of the growing layers caused by the bombardment of energetic Ar ions due to the negative bias at the substrate. The multilayer film deposited in this way was analysed for composition profile by AES technique. The profile in Figure 52 on page 127 shows that except for the top-most Mo layer on which no layer is subsequently deposited , all the lower layers

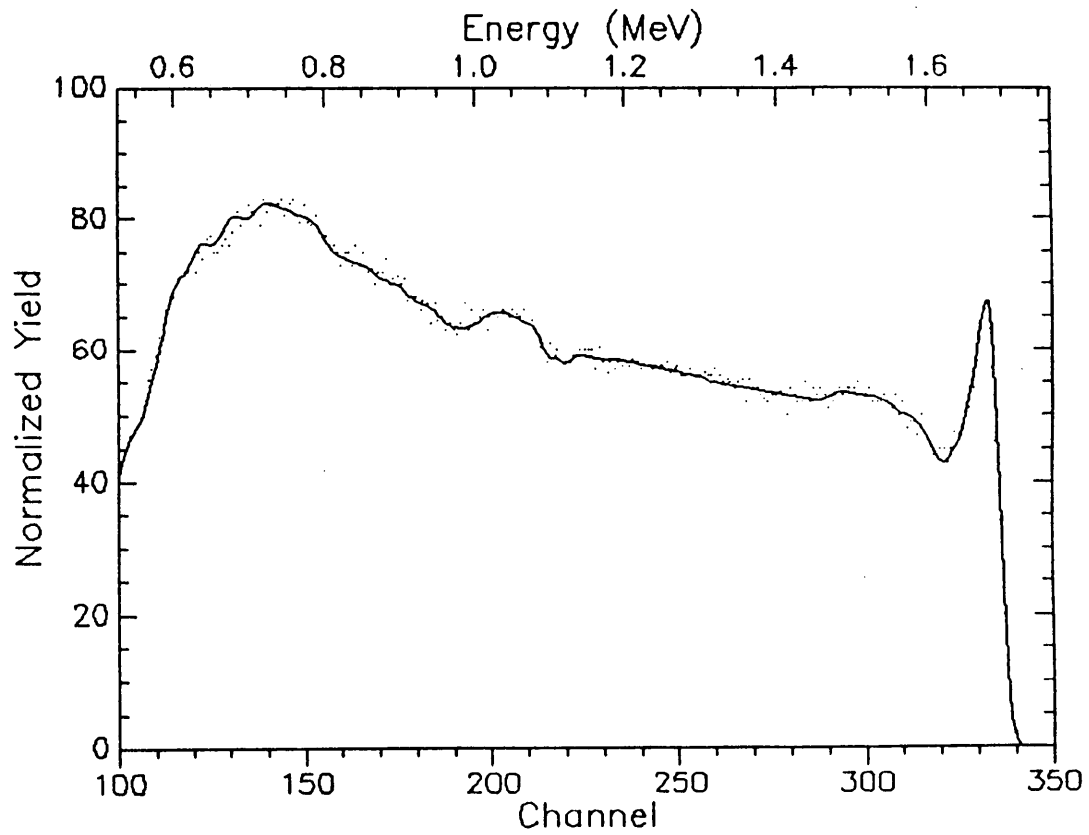


Figure 49. Experimental and simulated RBS spectra for a Mo/Al multilayer.: Expected layer thickness was $\sim 200 \text{ \AA}$ for Mo and Al.

Table 10. Simulated composition-depth profile information for a Mo/Al multilayer.

Expected layer thickness was $\sim 200 \text{ \AA}$ for Mo and Al.

Current File:	[GIRIDHAR.GIRI]M0AL.FBS:1			
Identifier:	Mo/Al multilayer film (as deposited).			
Date:	July 8 1986			
2.000 MeV	1.50 uCoulombs			
Channel Energy Constants:	4.9577 30.1282			
Correction Factor:	1.0000			
Angles (Theta, Phi, Omega):	-25.0000 15.0000 8.080			
Livetime text:				
Channel number of first data point:	103.0			
Number of data points:	254			
Detector FWHM:	15.0 keV Beam: He+			
RMS Beam current:	0.0 nA Geometry: IBM			
Thickness	Sublayers	Composition	.	.
40.00 A	auto	Al	0.700	Mo
170.00 A	auto	Al	0.200	Mo
100.00 A	auto	Al	0.450	Mo
80.00 A	auto	Al	0.550	Mo
150.00 A	auto	Al	0.600	Mo
250.00 A	auto	Al	0.667	Mo
300.00 A	auto	Al	0.700	Mo
200.00 A	auto	Al	0.660	Mo
500.00 A	auto	Al	0.630	Mo
1000.00 A	auto	Al	0.610	Mo
2000.00 A	auto	Al	0.630	Mo
1500.00 A	auto	Al	0.625	Mo
650.00 A	auto	Al	0.630	Mo
600.00 A	auto	Al	0.665	Mo
800.00 A	auto	Al	0.680	Mo
600.00 A	auto	Al	0.700	Mo
500.00 A	auto	Al	0.685	Mo
500.00 A	auto	Al	0.675	Mo
800.00 A	auto	Al	0.665	Mo
1000.00 A	auto	Al	0.640	Mo
500.00 A	auto	Al	0.670	Mo
500.00 A	auto	Al	0.710	Mo
350.00 A	auto	Al	0.750	Mo
250.00 A	auto	Al	0.800	Mo
250.00 A	auto	Al	0.850	Mo
400.00 A	auto	Al	0.880	Mo
400.00 A	auto	Al	0.920	Mo
45000.00 A	auto	Si	1.000	Mo

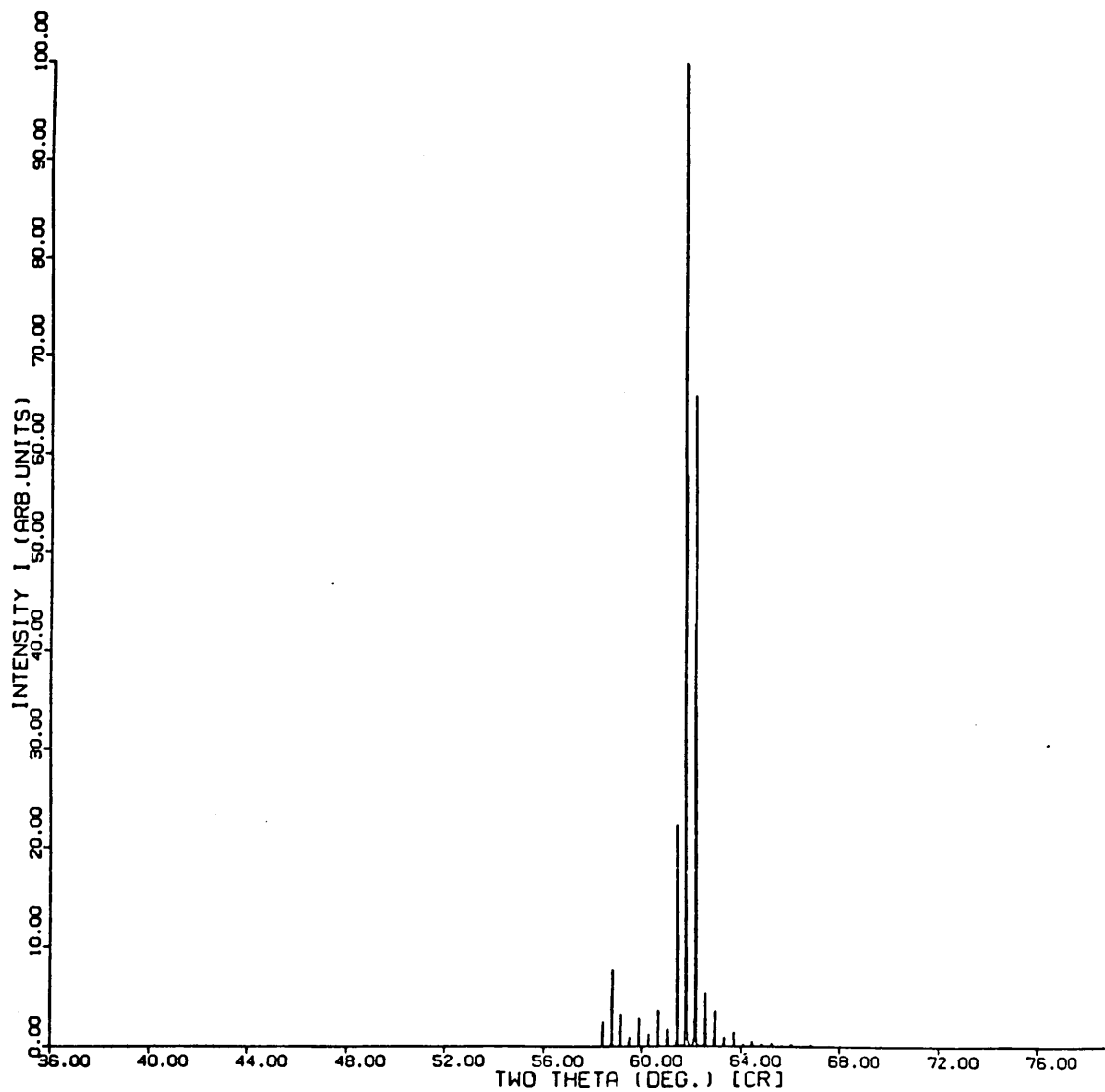


Figure 50. Ideal multilayer X-ray diffraction simulation for a film with modulation wavelength $\lambda \sim 400$ Å

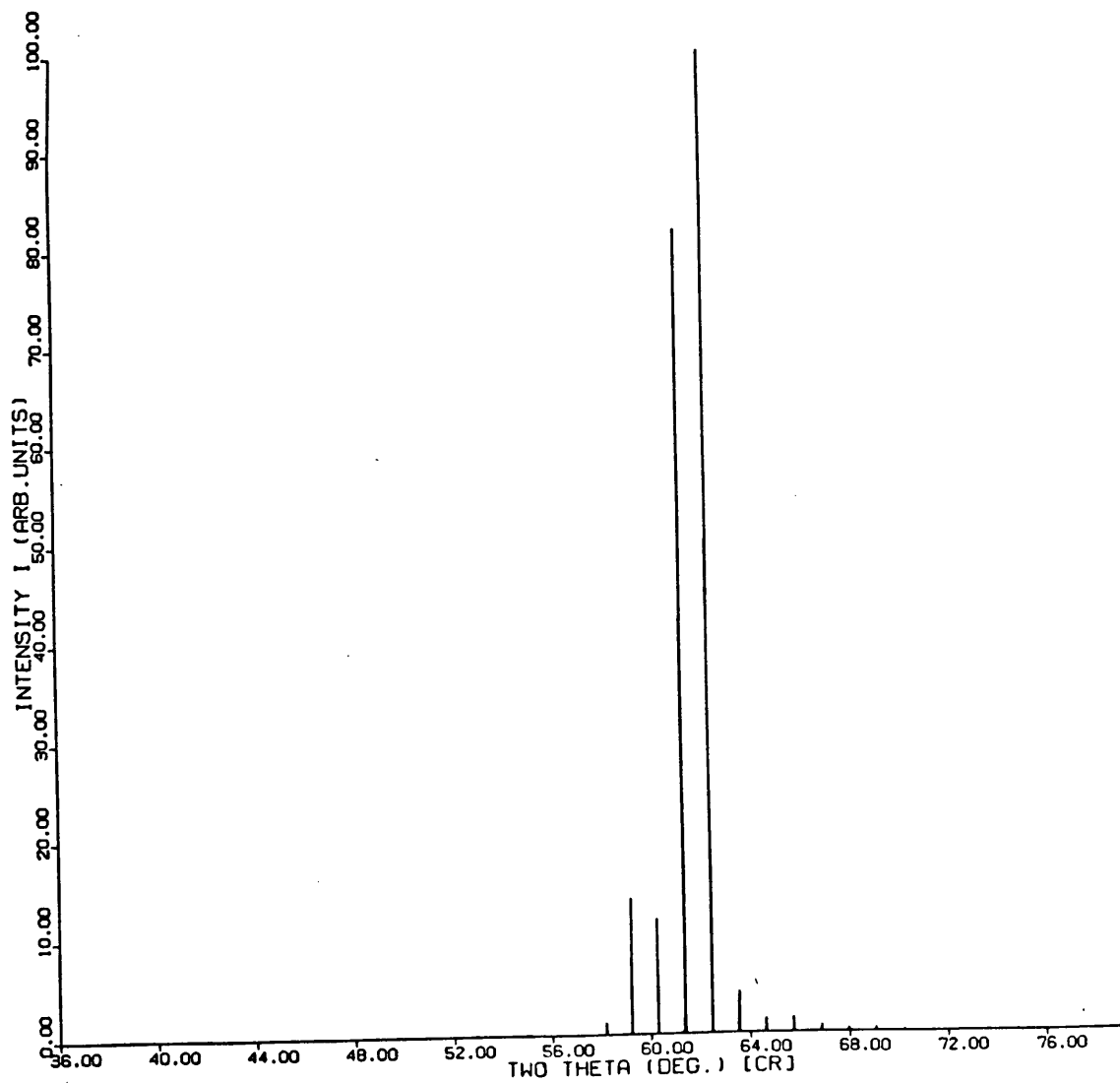


Figure 51. Ideal multilayer X-ray diffraction simulation for a film with modulation wavelength $\lambda \sim 120$ Å

are more or less completely mixed. This indicates that bottom layer gets mixed with the adjacent top layer due to the ion bombardment. it is clear from this investigation that the interface quality can only be improved by decoupling the growing film from the plasma with the use of a magnetron cathode assembly fitted behind the target.

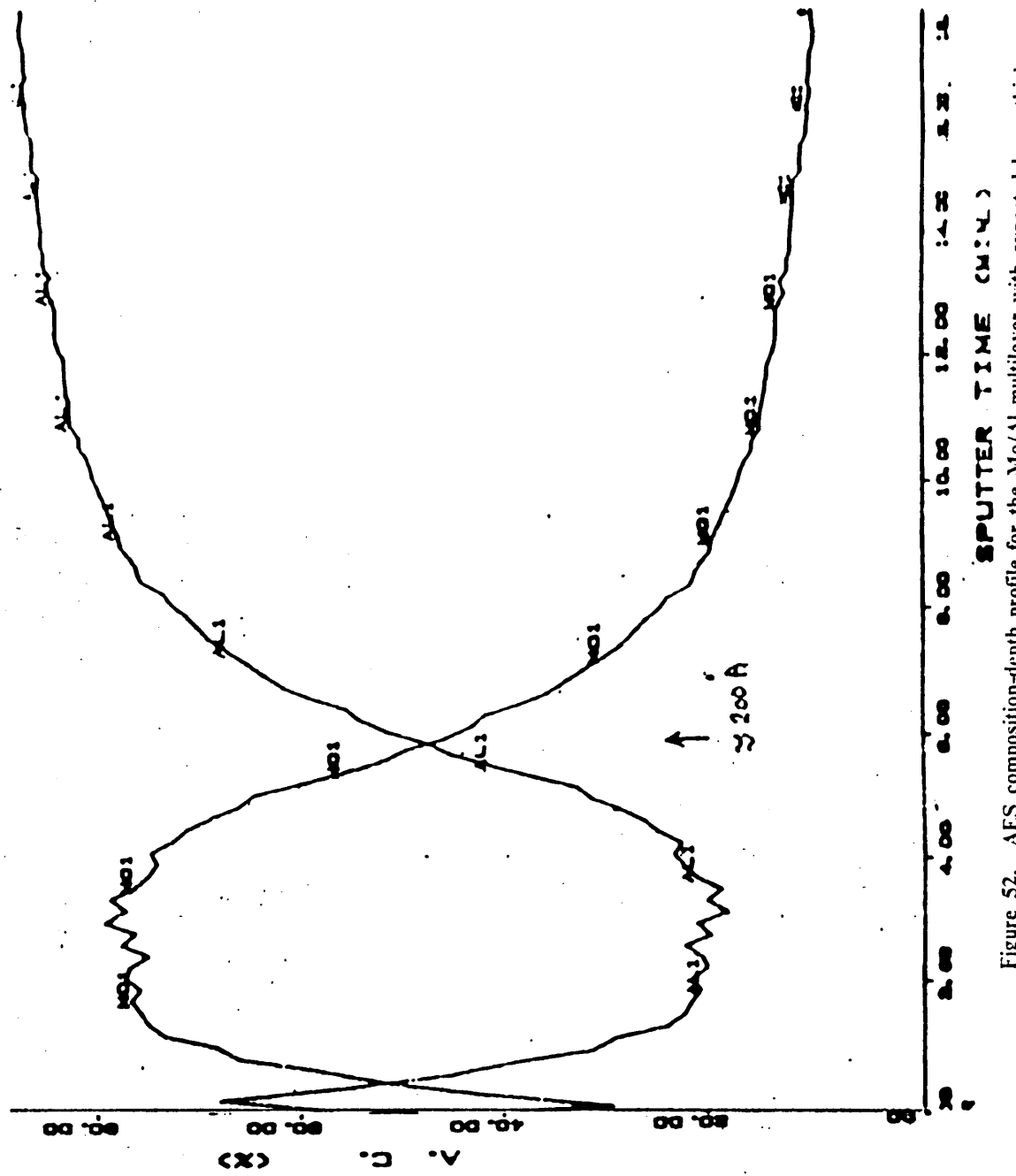


Figure S2. AES composition-depth profile for the Mo/Al multilayer with expected layer thickness of $\sim 200 \text{ \AA}$ of Mo and Al.

6.0 CONCLUSIONS AND RECOMMENDATIONS FOR FUTURE WORK

The preparation of Molybdenum / Aluminum layered thin films with a conventional diode rf- sputter deposition system was critically examined for the possibility of fabricating bilayer and multilayer thin films of the Mo/Al binary system. The interdiffusion and intermetallic compound formation in Molybdenum on Aluminum bilayer thin films were investigated in the temperature range 300-600°C. Auger Electron Spectroscopy, X-ray Diffraction and Scanning Transmission Electron Microscopy techniques were used for analysis of the thin film samples for composition and structural details. The TEM samples seem to be a layer of Al with large grains on which a few large and a large number of fine Mo grains both grown with preferred orientations. From the analysis of electron and X-ray diffraction data obtained for annealed samples, formation of the intermetallic compound Al_{12}Mo was confirmed at temperatures above 300°C. Formation of the compound AlMo_3 was detected beyond 400°C. Formation of Al_8Mo_3 and one other unknown compound was detected above 500°C. The chemical interdiffusion coefficient D was measured at different temperatures as a function of composition. Lattice diffusivities of Mo in Al and Al in Mo were obtained as a function of temperature. The lattice diffusivities were fitted to an Arrhenius type equation to estimate the activation energy for diffusion. The values of acti-

vation energy and pre-exponential factor obtained for Mo diffusion in Al were compared with the values reported in the literature. As a result of the fine grain structure of the films, diffusion is expected to occur through short-circuit paths with lower activation energy. It was concluded that multilayers of good interface quality could not be prepared with the present conventional diode sputtering system and that one needs to upgrade the sputtering system by having magnetron target assemblies fitted to the targets.

Future work can concentrate on the effect of ion-beam mixing of the Mo/Al bilayer samples at various ion fluences and to determine the mechanism of mixing. Formation of passive amorphous protective coatings by ion-beam mixing of layered thin films is a current topic of interest in research and application. An understanding of the mechanisms of mixing and radiation enhanced diffusion in such layered materials is vital for proper process control of the coating formation. Work has been started to model the ion-beam mixing in Mo/Al bilayer films using theoretical calculations. Some preliminary results are presented in appendix B of this thesis. The Mo/Al bilayer films are currently being experimentally investigated for ion-beam mixing characteristics. It would prove useful to compare the results of ion-beam mixing with the results of the present investigation to bring out the differences between ion-beam mixing and thermal diffusion mechanisms.

If the sputtering system is converted to a magnetron system, good quality multilayers of Mo/Al can be deposited. These films have important and novel properties and are easily examined with X-ray diffraction techniques. Recently multilayer thin films are being used for preparing surface alloyed coating because of a higher mixing efficiency than bilayer films. It would be instructive and useful to the effects of ion-beam mixing of multilayers and compare the results with the mixing of bilayers.

REFERENCES

1. S. P. Murarka, Ann. Rev. Mater. Sci. **13**, 117 (1983).
2. J. K. Howard, J. Appl., Phys. **49**, 4083 (1978).
3. I. K. Schuller, Phys. Rev. Lett. **44**, 1597 (1980).
4. M. R. Khan et. al., Phys. Rev. **B27**, 7186 (1983).
5. D. B. McWhan et. al., J. Appl. Phys. **54**, 3886 (1983).
6. W. P. Lowe and T. H. Geballe, Phys. Rev. **B29**, 4961 (1984).
7. T. R. Werner et. al., Phys. Rev. **B26**, 2224 (1982).
8. A. F. Jankowski and T. Tsakalakos, J. Appl. Phys. **57**, 1835 (1985).
9. T. W. Barbee Jr. and J. H. Underwood, Opt. Commun. **48**, 161 (1983).
10. H. S. Chen, Rep. Prog. Phys. **43**, 353 (1980).
11. G. S. Anderson et. al., J. Appl. Phys. **10**, 2991 (1962).
12. W. D. Westwood, Prog. Surf. Sci. **7**, 71 (1976).
13. J. L. Vossen and J. J. Cuomo. In 'Thin Film Processes', (J. L. Vossen and W. Kern eds.), Academic Press Inc., New York (1978).
14. H. A. Huggins and M. Gurvitch, J. Vac. Sci. Tech. **A1**, 77 (1983).
15. T. W. Barbee Jr. In 'Synthetic Modulated Structures', (L. L. Chang and B. C. Giessen eds.), Academic Press Inc., Orlando, Florida (1985).
16. T. W. Barbee Jr. and D. L. Keith. In 'Synthesis and Properties of Metastable Phases' (E. S. Machlin and T. J. Rowland eds.), AIME, New York.

17. J. A. Thornton and A. S. Penfold. In 'Thin Film Processes', (J. L. Vossen and W. Kern eds.), p.77, Academic Press Inc., New York (1978).
18. A. H. Eltoukhy and J. E. Greene, *J. Appl. Phys.* **50**, 505 (1979).
19. L. Brewer and R. H. Lamoreaux, *Bull. Alloy Phase Diagrams.* **1**, 2 (1980). Also in 'Binary Alloy Phase Diagrams', (T. B. Massalski ed.), vol.1. ASM (1986).
20. K. Kamei, T. Ninomiyo, and S. Terauchi, *Technol. Rep. Kansai Univ., Osaka.* **13**, 93 (1972).
21. M. Hansen, 'Constitution of Binary Alloys', McGraw Hill, New York. p.115 (1958).
22. Swanson and Tatge, *NBS Circular 539*, vol. 1, 11 (1953).
23. L. K. Walford, *Acta Cryst.* **17**, 57 (1964).
24. J. A. Leake, *Acta Cryst.* **17**, 918 (1964).
25. M. Potzschke and K. Schubert, *Z. Metallk.* **53**, 548 (1962).
26. J. B. Forsyth and G. Gran, *Acta Cryst.* **15**, 100 (1962).
27. K. Schubert et. al., *Naturwissenschaften.* **49**, 57 (1962).
28. E. A. Wood et al., *Acta Cryst.* **11**, 604 (1958).
29. Swanson and Tatge, in X-ray Powder Data File, ASTM, Philadelphia (1960).
30. R. W. Balluffi and J. M. Blakely, *Thin Solid Films.* **25**, 363 (1975).
31. Nguyen van Chi, *Neue Huette.* **23(4)**, 147 (1978).
32. J. Rexer, *Z. Metallk.* **62(11)**, 844 (1971).
33. M. Kitada and N. Shimizu, *J. Mater. Sci.* **19**, 1339 (1984).
34. M. B. Chamberlain, *J. Vac. Sci. Technol.* **16(2)**, 339 (1979).
35. W. P. Lowe et. al., *Phys. Rev. B* **24**, 6193 (1981).
36. D. Briggs and M. P. Seah, 'Practical Surface Analysis by Auger and X-ray Photoelectron Spectroscopy', Wiley & Sons, New York (1983).
37. A. Joshi et. al. In 'Methods of Surface Analysis' (A. W. Czanderna ed.), Elsevier, Amsterdam, p.159 (1975).
38. G. K. Wehner. In 'Methods of Surface Analysis' (A. W. Czanderna ed.), Elsevier, Amsterdam. p.5 (1975).
39. J. W. Coburn and E. Kay, *CRC Critical Reviews in Solid State Sciences*, p.561 Sept.(1974).
40. P. Braun et. al., *Adv. Electron. Electron Phys.* **57**, 231 (1981).
41. M. Optiz, Thesis. Technische Universitat, Wien (1979).

42. T. A. Adler, Thesis. VPI&SU. (1978).
43. R. J. Yesensky, Thesis. VPI&SU. (1979).
44. B. E. Warren, 'X-ray Diffraction, Addison - Wesley, Reading (1969) pp. 251-275.
45. C. N. J. Wagner. In 'Local Atomic Arrangements studied by X-ray Diffraction', Gordon and Breach, New York (1966).
46. T. M. Smith and C. R. Houska, Dept. of Materials Engg. VPI&SU. (Report submitted to NSF -report No. VPI-E-81.19) (1980).
47. J. Unnam et. al., Dept. of Materials Engg. VPI&SU. Report submitted to NSF. (1976).
48. D. B. McWhan. In 'Synthetic Modulated Structures'. (L. L. Chang and B. C. Giessen eds.), Academic Press Inc. Orlando (1985).
49. R. C. Cammarata and A. L. Greer, J. Non-Cryst. Solids. **61** and **62**, 889 (1984).
50. J. M. Gibson, Scripta Met. **20**, 451 (1986).
51. J. F. Ziegler ed. 'New Uses of Ion Accelerators'. Plenum, New York (1975).
52. P. H. Dionisio et. al., Nucl. Instr. and Meth. **B16**, 345 (1986).
53. P. Roberto, E. J. Savino, and D.Farkas. Materials Engineering Dept., VPI&SU. Unpublished Data.
54. L. R. Doolittle, Nucl. Instr. and Meth. **B9**, 344 (1985)
55. L. R. Doolittle, 'A semi-automatic algorithm for Rutherford Backscattering Analysis', Proc. Ion Beam Analysis Conference (1985).
56. M. B. Chamberlain and S. L. Lehoczky, Thin Solid Films. **45**, 189 (1977).
57. R. Ludeke et. al., Appl. Phys. Lett. **24**, 417 (1974).
58. A. Segmuller and A. E. Blakeslee, Acta Cryst. **6**, 19 (1973).
59. R. Behrisch and B. M. U. Scherzer, Thin Solid Films. **19**, 247 (1973).
60. G. Thomas and M. J. Goringe. 'Transmission Electron Microscopy of Materials ', John Wiley & Sons, New York (1979).
61. W. Jost, 'Diffusion in Solids, Liquids and Gases', Academic Press, New York. p.31 and pp.75-77 (1960).
62. J. Askil ed.,'Radioactive Tracer Diffusion Data for metals , alloys and simple oxides ', (1970).
63. J. P. Biersack and L. G. Haggmark, Nucl. Instr. and Meth. **174**, 257 (1980).
64. M. Rangaswamy, Thesis. VPI&SU (1985).
65. S. M. Myers, Nucl. Instr. and Meth. **168**, 265 (1980).

Appendix A. CHARACTERISTICS OF MAGNETRON SPUTTERING SOURCES

As discussed in section 2.1.3 of Chapter 2, the three important conditions for sputter deposition of layered thin films of ultra-thin ($10\text{-}100\text{\AA}$) layer thickness are [15]

1. Sputter-source-deposition surface decoupling
2. Energy distribution of sputtered atoms
3. Geometry of source substrate configuration.

Though it is possible to optimize the last two factors in the conventional diode sputtering source systems, the first factor of plasma-substrate decoupling is extremely difficult and nearly impossible to achieve with conventional diode sources.

Magnetron sputter sources, in addition to having approximately an order of magnitude higher deposition rate than possible with conventional diode sources, are also capable of experimentally isolating or decoupling the plasma from the deposition surface almost completely. In fact, it is possible with these magnetron sources to completely eliminate the bombardment of the substrate and growing film by almost all energetic particles except for the atoms of the sputtered

material being deposited, atoms of back scattered inert sputtering gas and UV photons. The effect of bombardment of the deposition surface by neutral atoms and photons is generally considered insignificant when compared with the effect of charged particle bombardment in degrading interface character in layered thin films. The higher deposition rates possible with magnetron sputtering sources (typically 10-30 Å/sec) are a direct result of increased ionization and sputtering efficiency of these sources.

The conventional diode sputtering sources of the multi-source rf sputtering system that were used for fabrication of layered thin films in the present work can be converted into a planar magnetron source by the essential addition of an array of permanent magnets behind each target. The array of magnets are arranged in such a way that there is at least one region in front of the target surface where the locus of the magnetic field that lies parallel to the surface is a closed path. This is illustrated for a circular target source in Figure A. The tunnel shaped magnetic field forms the boundary of a region adjacent to the target surface in which the discharge plasma is constrained. The plasma is constrained because of the secondary electron trapping which occurs due to the closed toroidal trajectory of the secondary electrons, caused by the magnetic field perpendicular to the electric field. It is important to note that in order to achieve a useful field beyond the target face, the target must be magnetically saturated. This factor becomes important for sputtering ferromagnetic target materials, in which case special cobalt-rare earth magnets may be used. Normally, ferrite magnets are used for the magnetic array.

Planar magnetron sources are of the high constant current and low voltage type in contrast to the conventional diode sources that are of high constant voltage and low current type. The rf power supplies used for the diode rf sputtering system are also usually suitable for planar magnetron sputtering. Commercial rf sputtering supplies can normally tolerate the occasional arcs and transient high voltage pulses of rf planar magnetron sputtering. The variable components (capacitors or inductors) of the rf impedance matching network need to be adjusted and tuned to compensate for the lower plasma impedance of the planar magnetron sources.

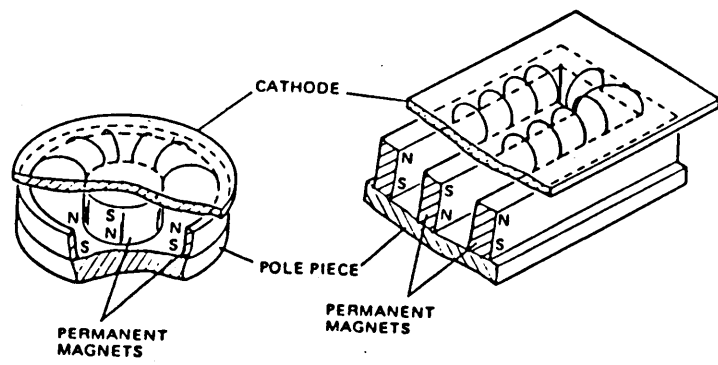


Figure 53. Circular planar magnetron sputtering source: [Ref.: R. K. Waits, In 'Thin Film Process' (J. L. Vossen and W. Kern eds.) p.134 Academic Press Inc. New York (1978).]

Substrate-biasing, if needed, is also easily done just as in the diode source system; rf planar magnetron deposition rate control is achieved in the same manner as in conventional rf sputter deposition.

Planar magnetron sources are usually operated in Argon sputtering gas at a pressure of 1-10 mTorr, which is an order less than the gas pressures used in conventional rf diode sputtering systems. This low pressure operation may help improve the quality of the deposited film by reducing the impurity levels and by increasing the surface mobility of depositing atoms thus preventing island formations. Also sputtering gas pressure has less influence on deposition rate for the planar magnetron sputtering than for the diode sputtering. Magnetron sputtering has at least three times the cathode erosion rate efficiency of conventional diode sputtering. An effect peculiar to magnetron sputtering is the non-uniform erosion of the cathode surface. In planar magnetrons, a few thermalized electrons do escape the electron traps and arrive at the substrate. Neutral atom bombardment of the deposition surface by backscattered neutralized ions and depositing species may lead to higher surface mobility for the deposited atoms. For a given deposition rate, the substrate temperature for planar magnetron sputtering is in general significantly lower than for rf diode sputtering. Shorter target-substrate separation distances are possible which increases deposition rate. Faster deposition decreases the deposition time and hence the operating cost of the sputtering system, such as the cost of the liquid nitrogen required for the cold trap of the vacuum system.

Due to the non-uniform erosion of the target in planar magnetron sputtering, non-uniform coating may take place. This is easily offset by modification of magnet geometry, or by empirically shaped aperture shields (shapers) and by substrate table rotation, moving the substrate past the sources. The targets can be mechanically adjusted from time to time so that non-uniform erosion does not cause very uneven target surface.

The advantages of planar magnetron sources are faster deposition, increased efficiency of operation, possibility of making layered thin films with compositionally abrupt interfaces and ease of conversion from conventional rf diode to rf planar magnetron sputtering sources. These advantages make the recommendation for installation of the magnetron target assemblies in the conventional rf sputter deposition system used for the present work a sound one. It is particularly noted that this conversion is essential if good quality metallic multilayer thin films are to be prepared by sputter deposition.

Appendix B. THEORETICAL CALCULATIONS ON ION-BEAM MIXING OF Mo/Al BILAYERS

The effect of ion-beam mixing of Mo/Al bilayer thin films that were examined for thermal diffusion behavior in the present study was qualitatively assessed using computer simulations. The simulations were carried out for bilayer films with a thick Al bottom layer and a thin Mo top layer. Three different layer thickness values were used for the Mo layer. These thicknesses are 400, 1200 and 4000 Å. First the appropriate energy of the ion-beam that has to be used so as to get the peak of the damage profile as close to the interface as possible. The simulations were done for ion-beam mixing with a high energy Argon ion-beam. The Monte Carlo computer code TRIM was used for obtaining the damage energy distributions for all three bilayer films at different energies. It was found that for the 400 Å Mo on Al film the ion beam energy required was 100 keV for the maximum damage to occur at the Mo/Al interface. For the 1200 Å film the energy was 300 keV and for the 4000 Å film it was 1 MeV. These energy values were used for ion-beam mixing simulation of the respective films treated at different fluence levels.

The process of ion-beam mixing was assumed to be 'diffusion-like' and the resulting diffusion equations were solved by the Cranck-Nicholson finite difference technique. The computer code STEPIMP written implementing this technique [64] was used for obtaining the

composition versus depth profiles that are presented in the following figures. The computer code considers ion-beam processes such as ion collection, sputtering, lattice dilatation, radiation enhanced diffusion and collision-cascade mixing. Processes such as preferential sputtering and radiation-induced segregation were not included in the calculations. The effective interdiffusion coefficients for collisional cascade mixing were calculated from the expression given by Myers [65] which gives at least an estimate of the correct order of magnitude of the diffusivity. This expression is

$$D^x = (1/6) \lambda^2 P \quad (45)$$

where

λ = Root-mean square separation for vacancy-interstitial pair

and the function P is the number of displacements per target atom per unit time given by

$$P(x) = (0.8/2NE_d)(dE/dx)\phi \quad (46)$$

where

ϕ = Ion flux

N = Atomic density of the solid

E_d = Effective threshold displacement energy $\cong 30$ eV

(dE/dx) = Ion energy deposited per unit depth with E in eV and dx in nm

The profiles presented simple diffusion profiles with no discontinuities because the code can not assess the formation of intermetallic compounds.

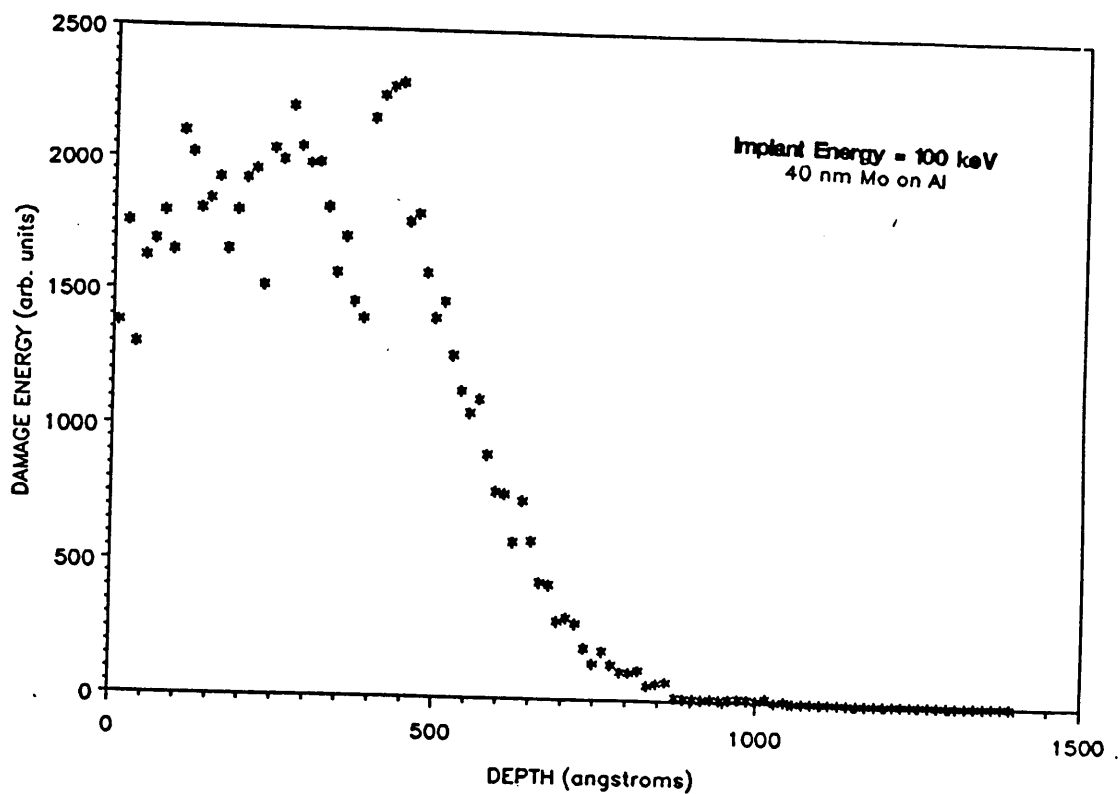


Figure 54. Damage energy profile of sample of a 400 Å Mo layer on Al (sample #1), ion-beam mixed with a 100 keV Ar beam.

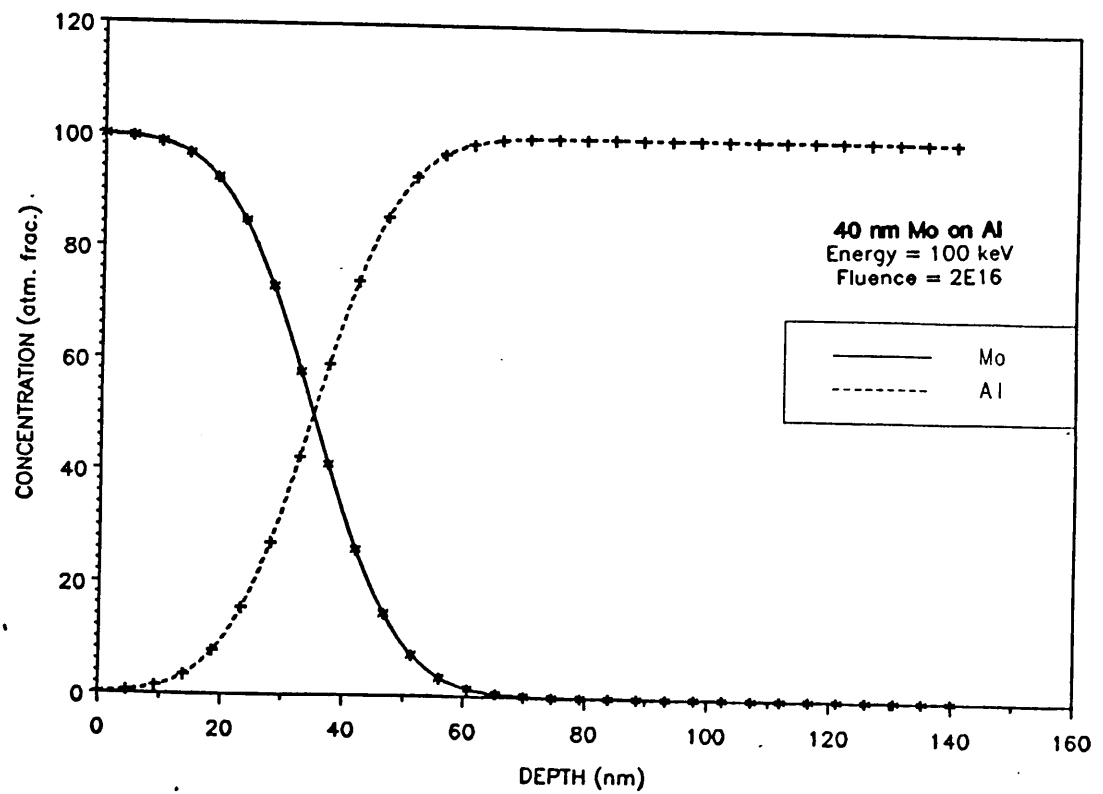


Figure 55. Concentration profile of sample #1 after ion-beam mixing to a dose of 2×10^{16} ions/cm²

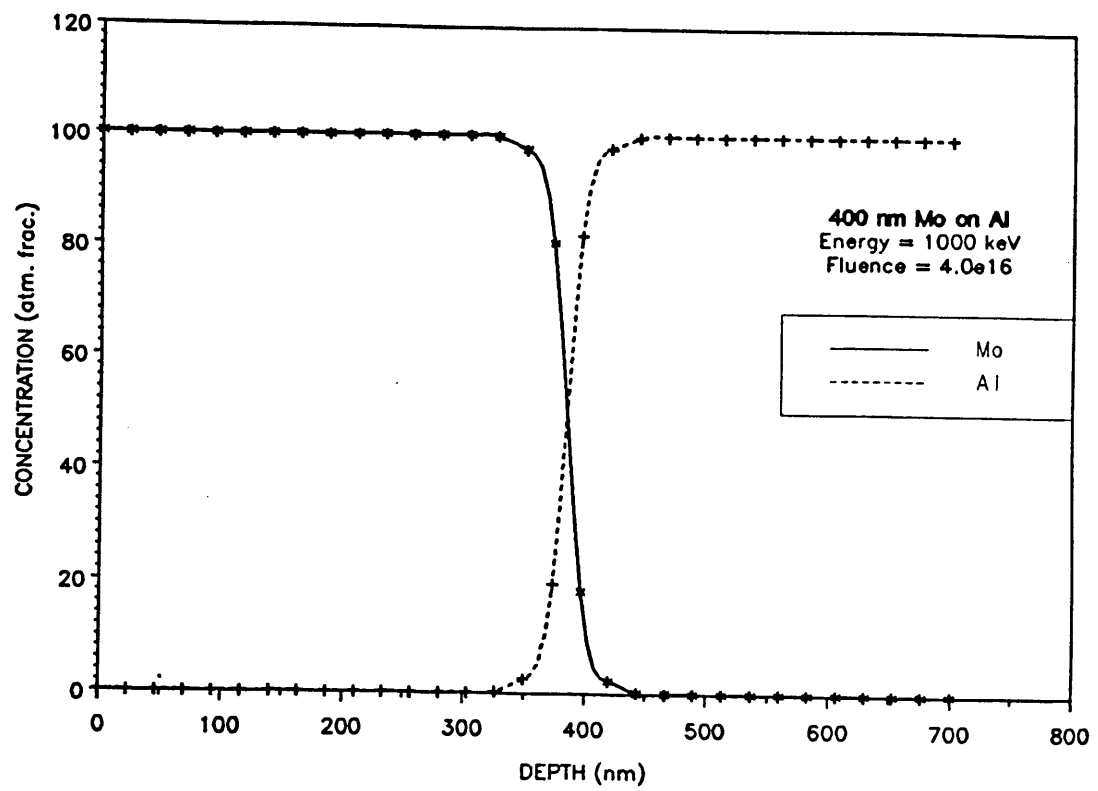


Figure 56. Concentration profile of sample #1 after ion-beam mixing to a dose of 4×10^{16} ions/cm²

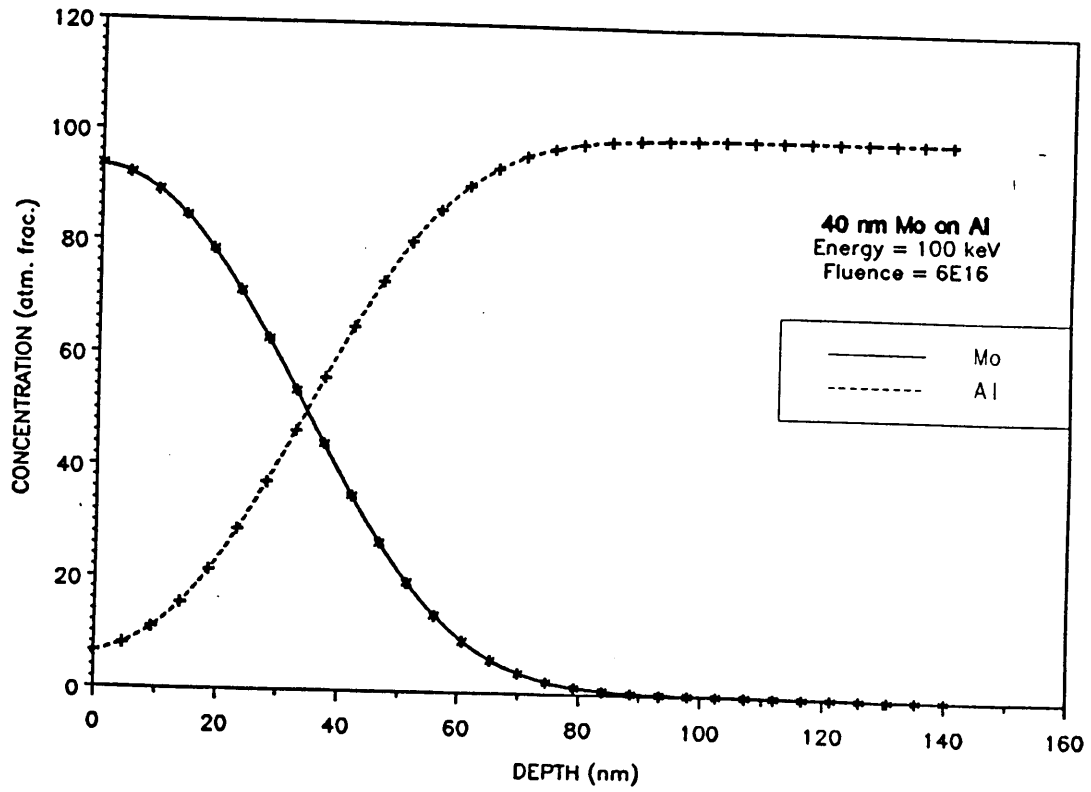


Figure 57. Concentration profile of sample #1 after ion-beam mixing to a dose of 6×10^{16} ions/cm²

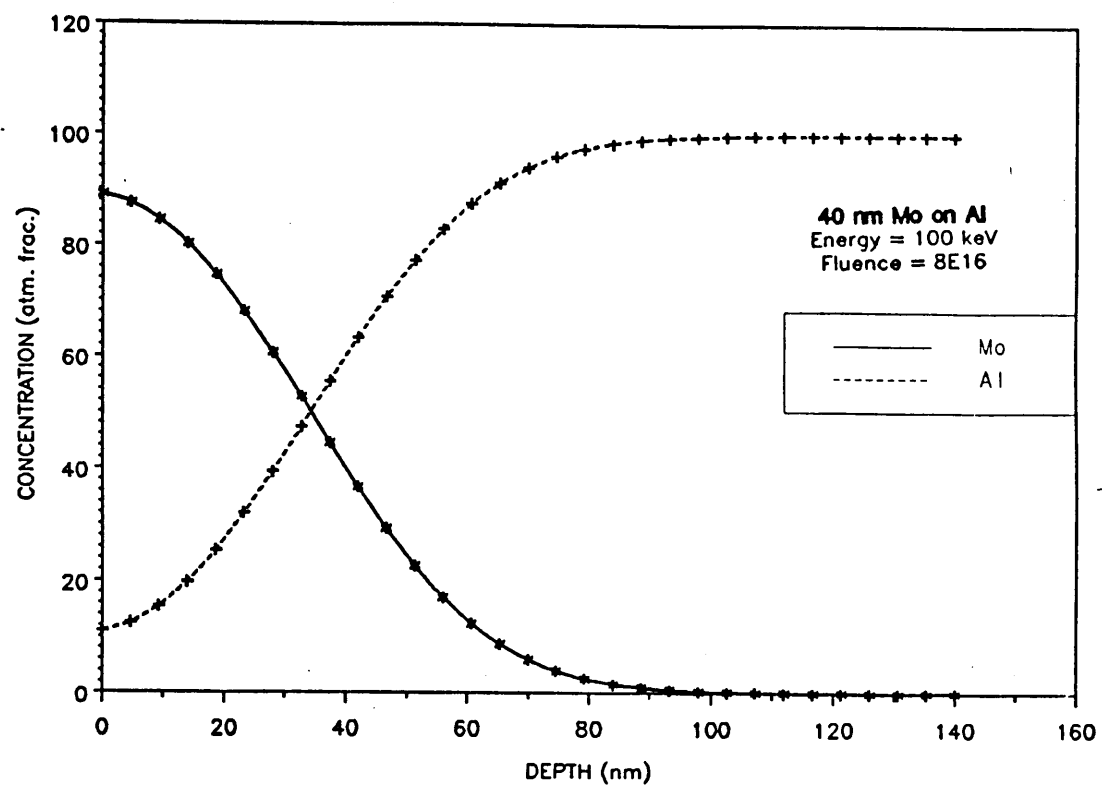


Figure 58. Concentration profile of sample #1 after ion-beam mixing to a dose of 8×10^{16} ions/cm²

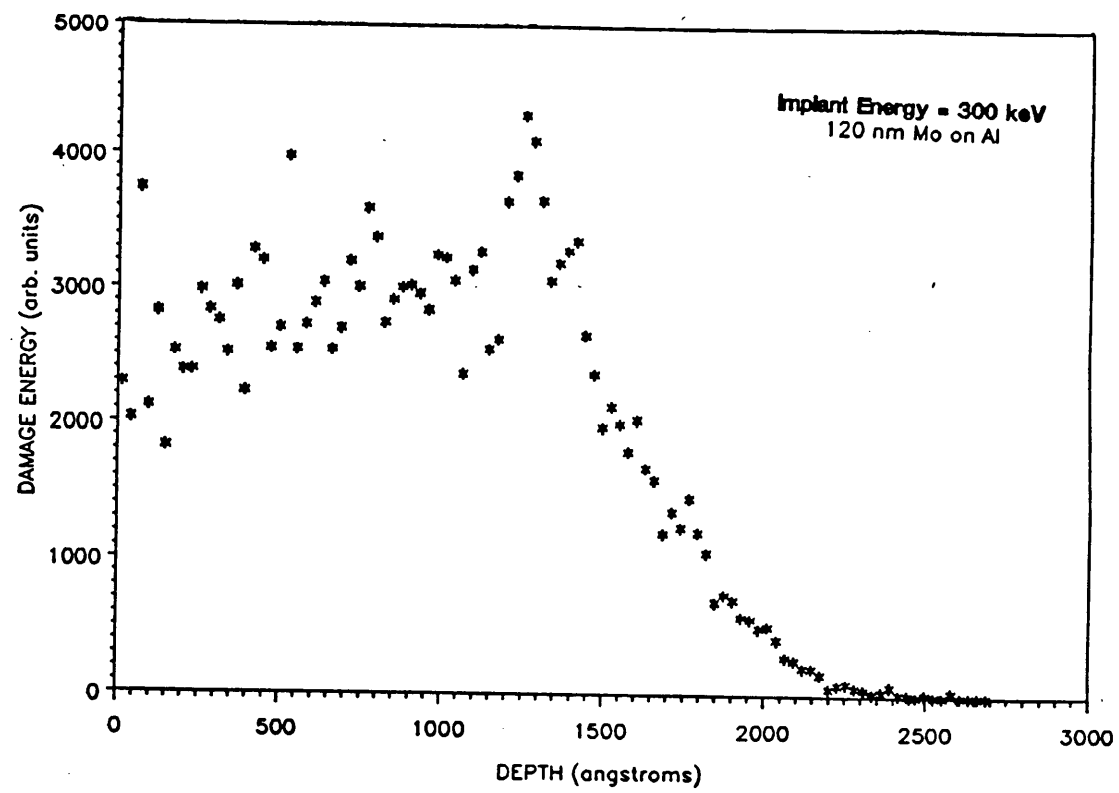


Figure 59. Damage energy profile of a 1200 Å Mo layer on Al (sample #2), ion-beam mixed with a 300 keV Ar beam.

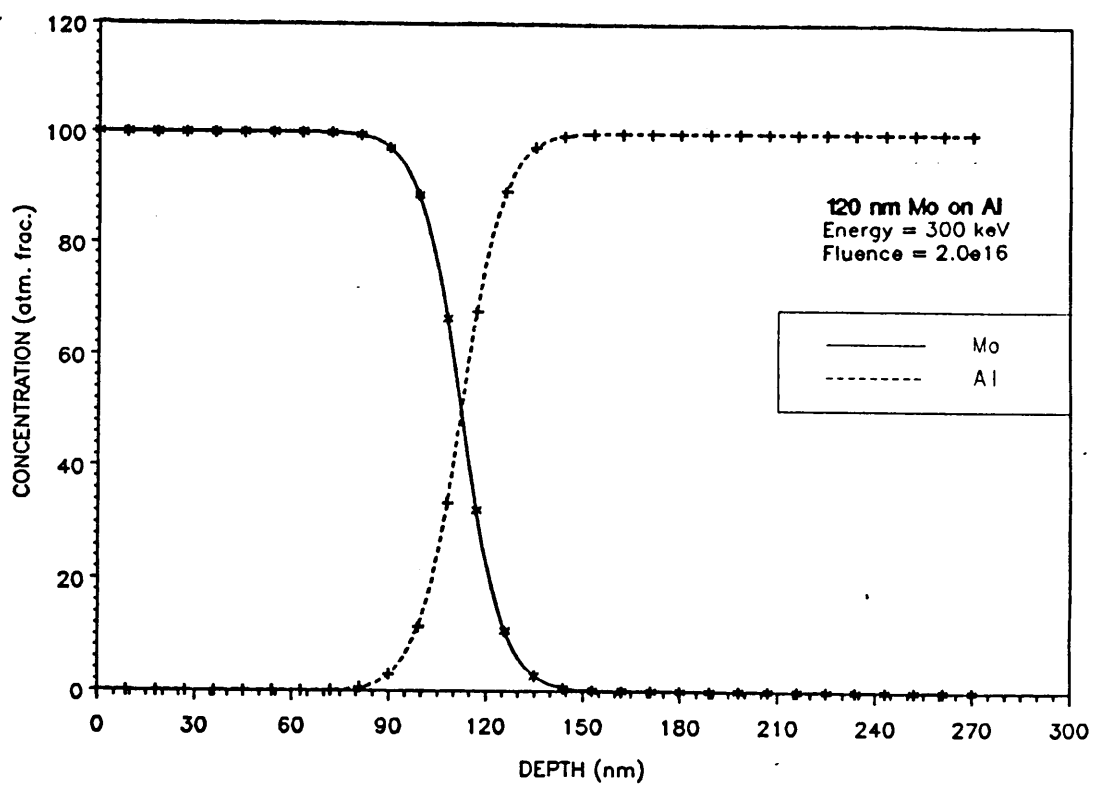


Figure 60. Concentration profile of sample #2 after ion-beam mixing to a dose of 2×10^{16} ions/cm²

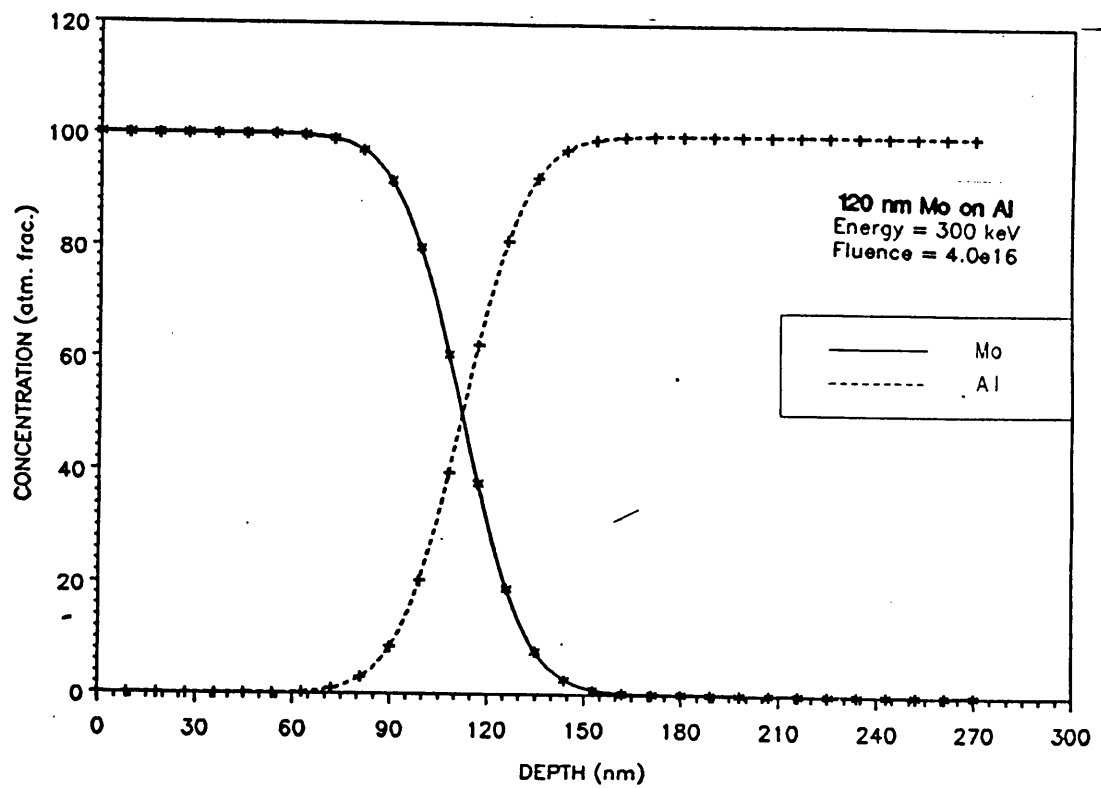


Figure 61. Concentration profile of sample #2 after ion-beam mixing to a dose of 4×10^{16} ions/cm²

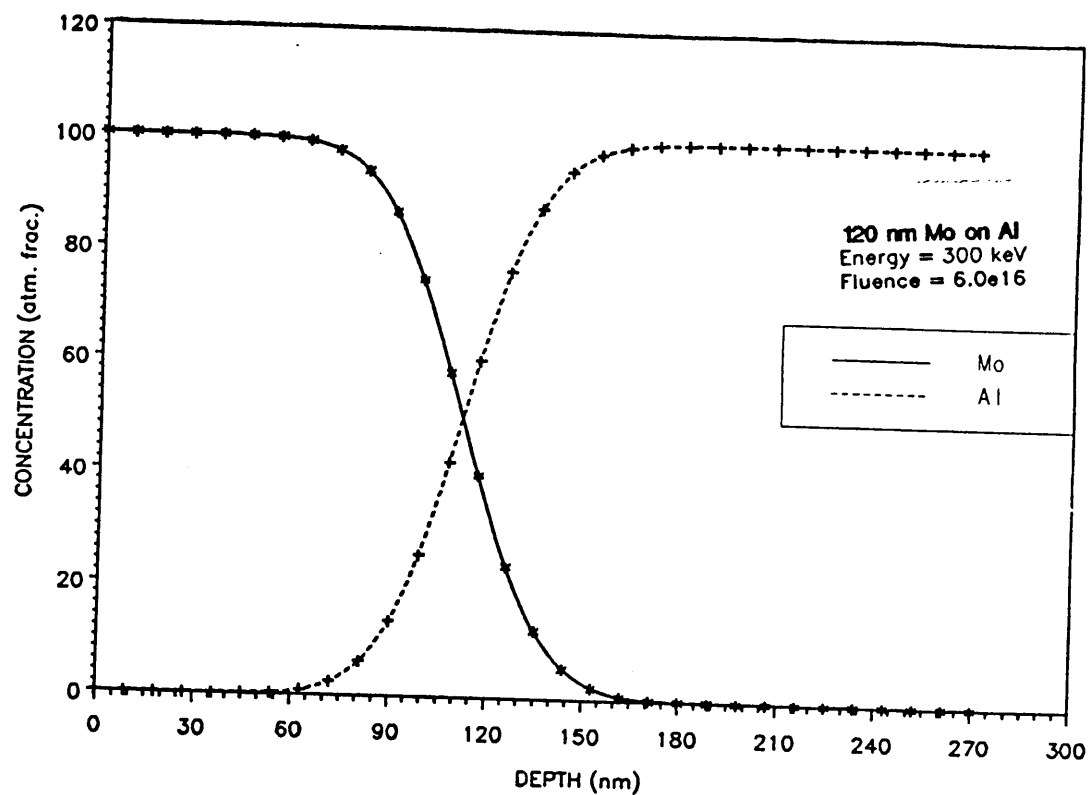


Figure 62. Concentration profile of sample #2 after ion-beam mixing to a dose of 6×10^{16} ions/cm²

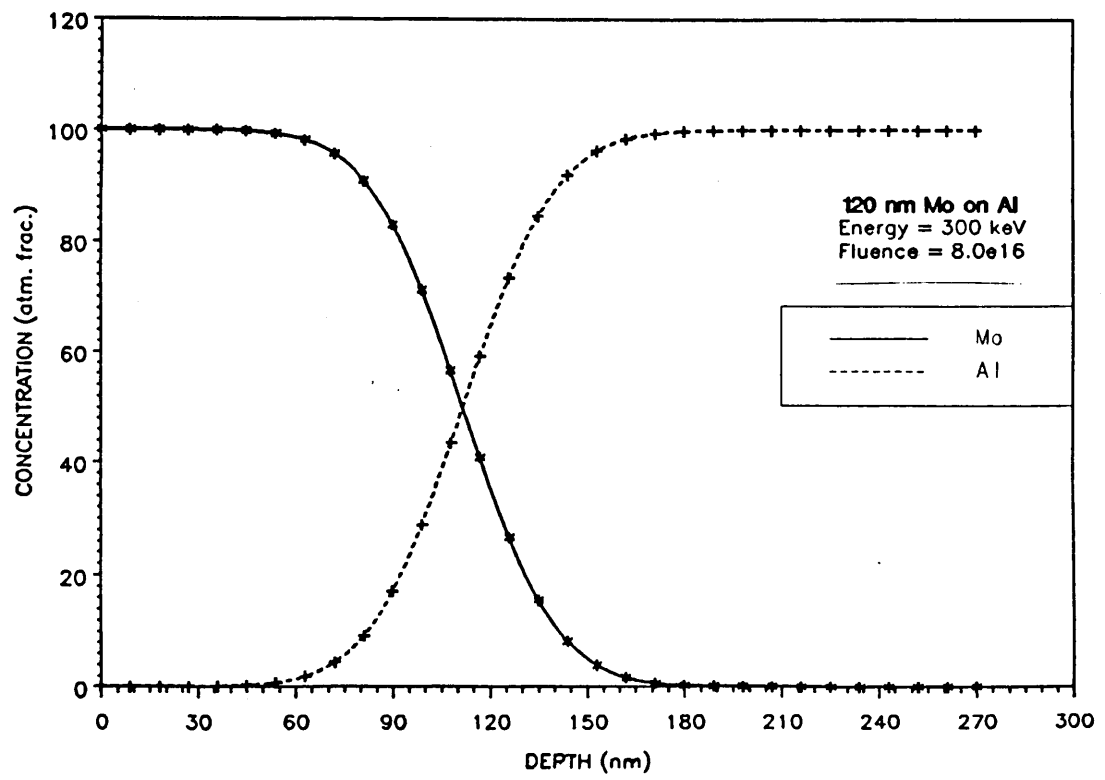


Figure 63. Concentration profile of sample #2 after ion-beam mixing to a dose of 8×10^{16} ions/cm²

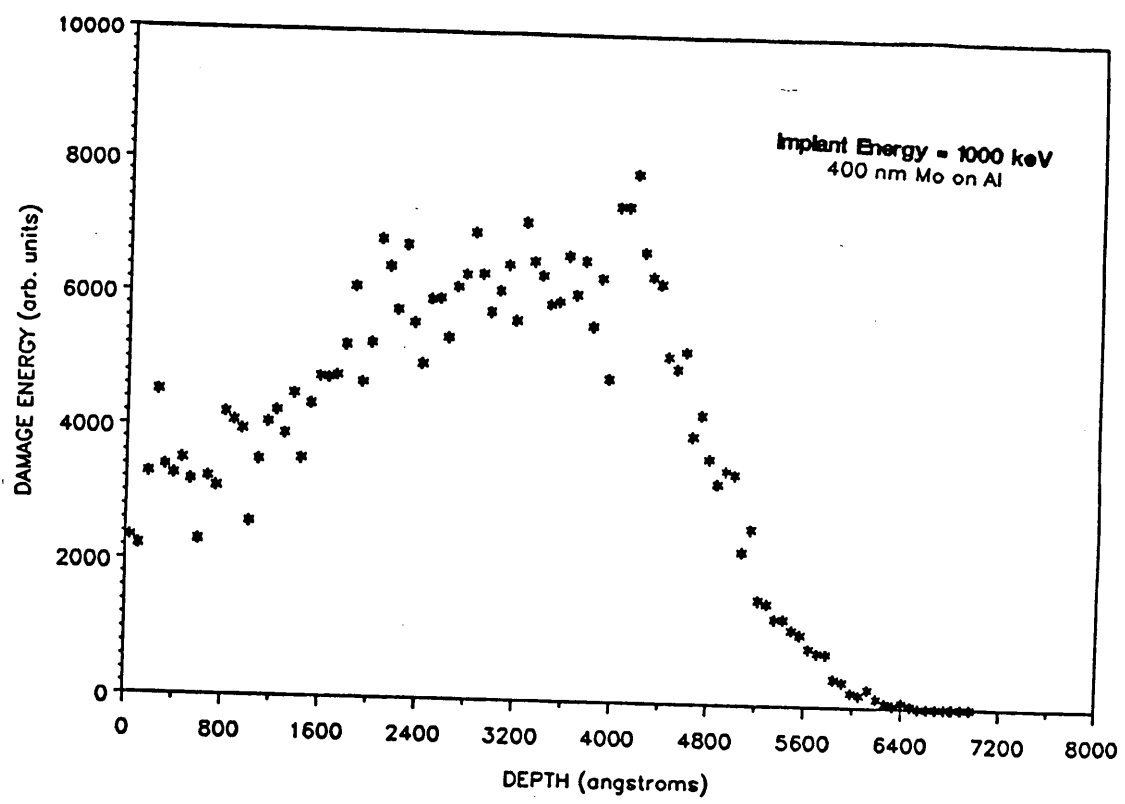


Figure 64. Damage energy profile of a 4000 Å Mo layer on Al (sample #3), ion-beam mixed with a 1 MeV Ar beam.

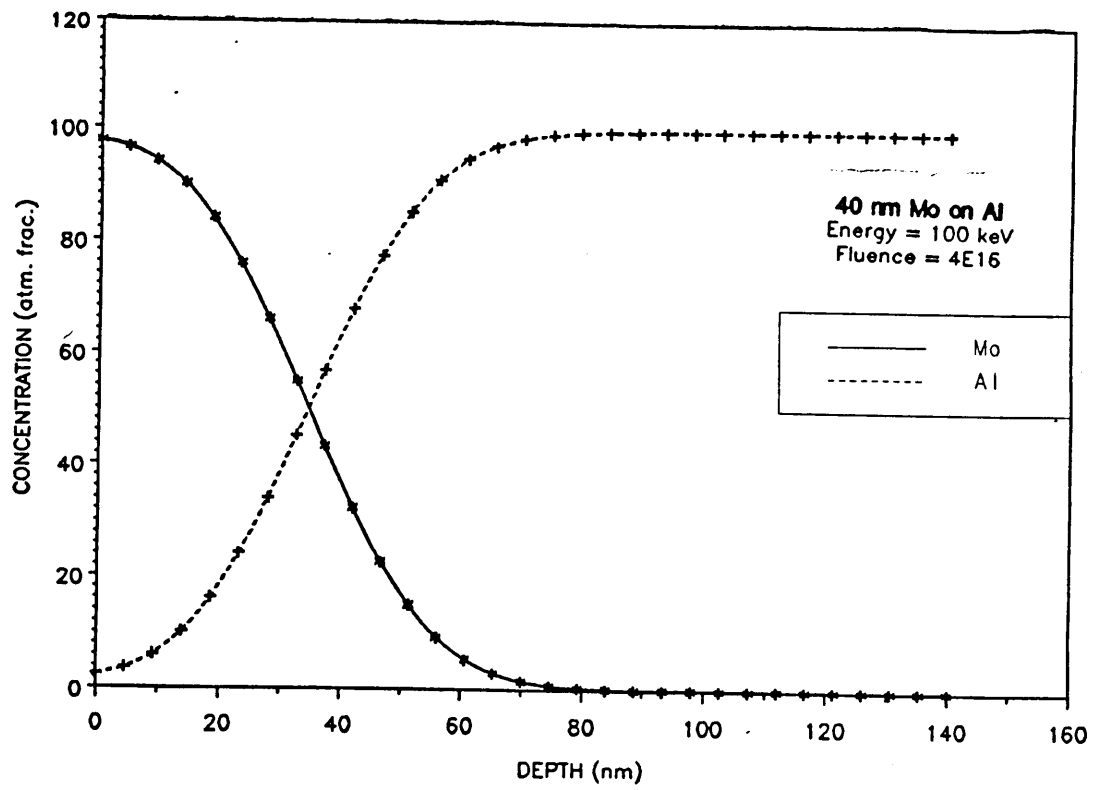


Figure 65. Concentration profile of sample #3 after ion-beam mixing to a dose of 4×10^{16} ions/cm²

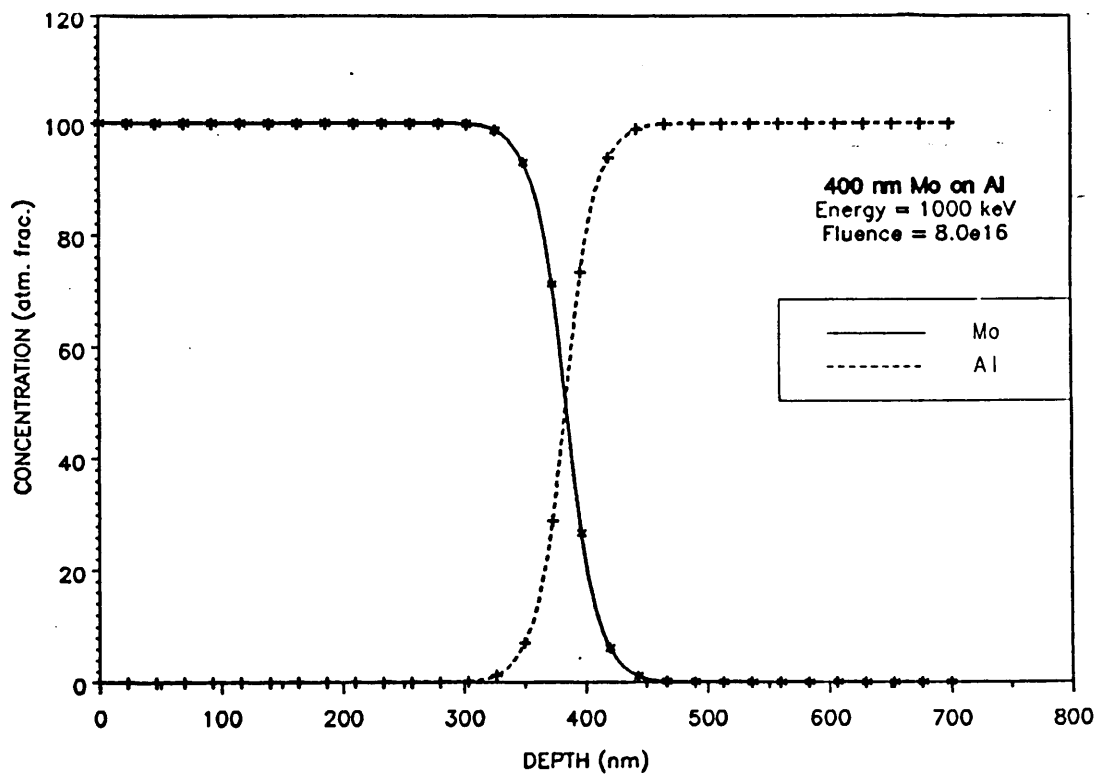


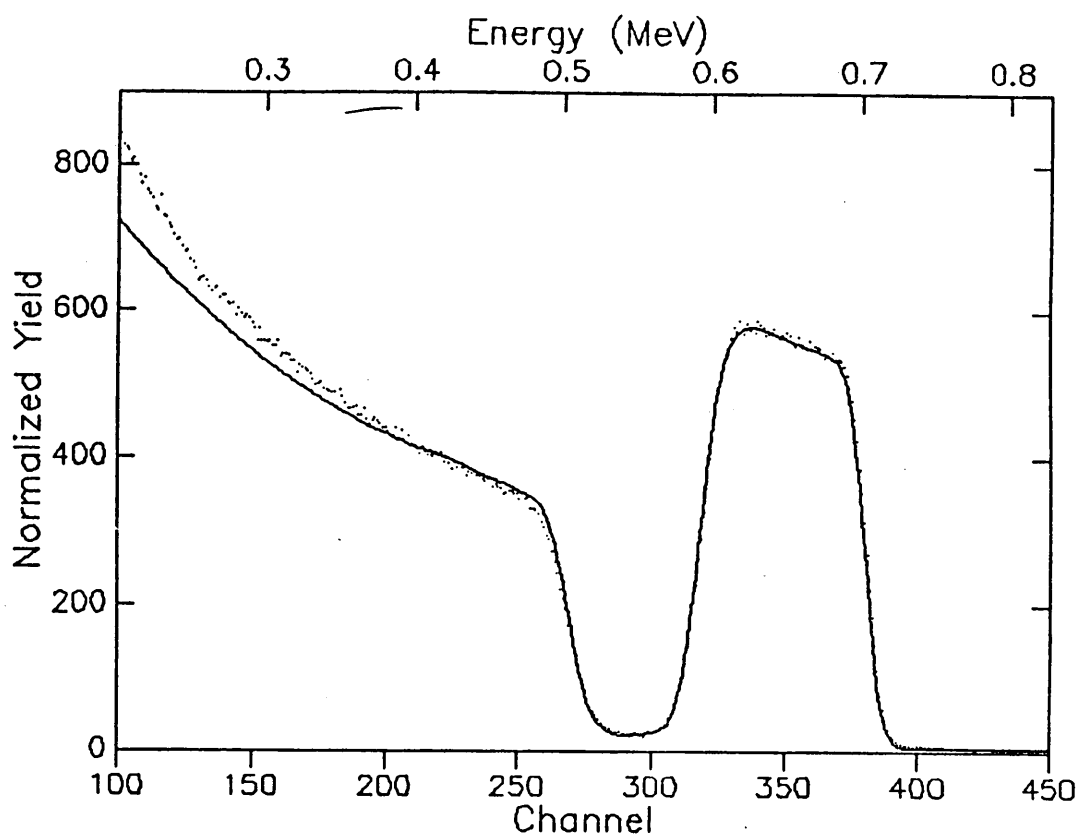
Figure 66. Concentration profile of sample #3 after ion-beam mixing to a dose of 8×10^{16} ions/cm²

Appendix C. RBS ANALYSIS OF ION-BEAM MIXING OF Sn THIN FILM ON Fe SUBSTRATE

Experimental RBS spectrum obtained from a chemical vapor deposited approximately 1100 Å thick Sn thin film on Fe [53] were analysed using the software package RUMP [54, 55] are presented in this appendix. The composition profiles obtained from the various spectra taken of specimen subjected to varying degrees of Ar ion fluences are presented following the experimental RBS spectra. A description of the experimental conditions of RBS analysis and the ion-beam treatment conditions are shown below each spectrum.

The results show that there is considerable loss of Sn from the surface during high temperature ion-beam treatment at high fluences caused by sputtering of the Sn layer. Low temperature ion beam mixing does not indicate as much loss of Sn from the surface as at high temperatures. When the beam energy is increased from 300 to 400 keV, the damage peak lies inside the Fe substrate and the mixing effect is not pronounced. The long tail of Sn obtained for samples subjected to high fluences at 300 keV may be an artefact introduced by curved uneven surface features. A preliminary examination of the surface under low-magnification SEM revealed

microtopographical features on the surface with only partial coverage of the substrates for samples subjected to high fluences. The fluctuations in the composition profiles may also be caused by the topographical features of the sample surface. Scaling of the stopping powers of both Sn and Fe was necessary to get the good fit to experimental data. The poor fit of experimental data to the simulations at lower energies might be caused by inelastic scattering effects, instrumental conditions such as the electronics of the detector and instrumental broadening due to slit scattering background level increase and other effects. The composition profile specified in terms of layer concentrations are shown below the spectra. With the software package RUMP, it is relatively simple to extract composition profile information from RBS spectra and the technique is also very suitable for analysis of the Mo/Al bilayers and multilayers with layer thickness larger than 100 Å

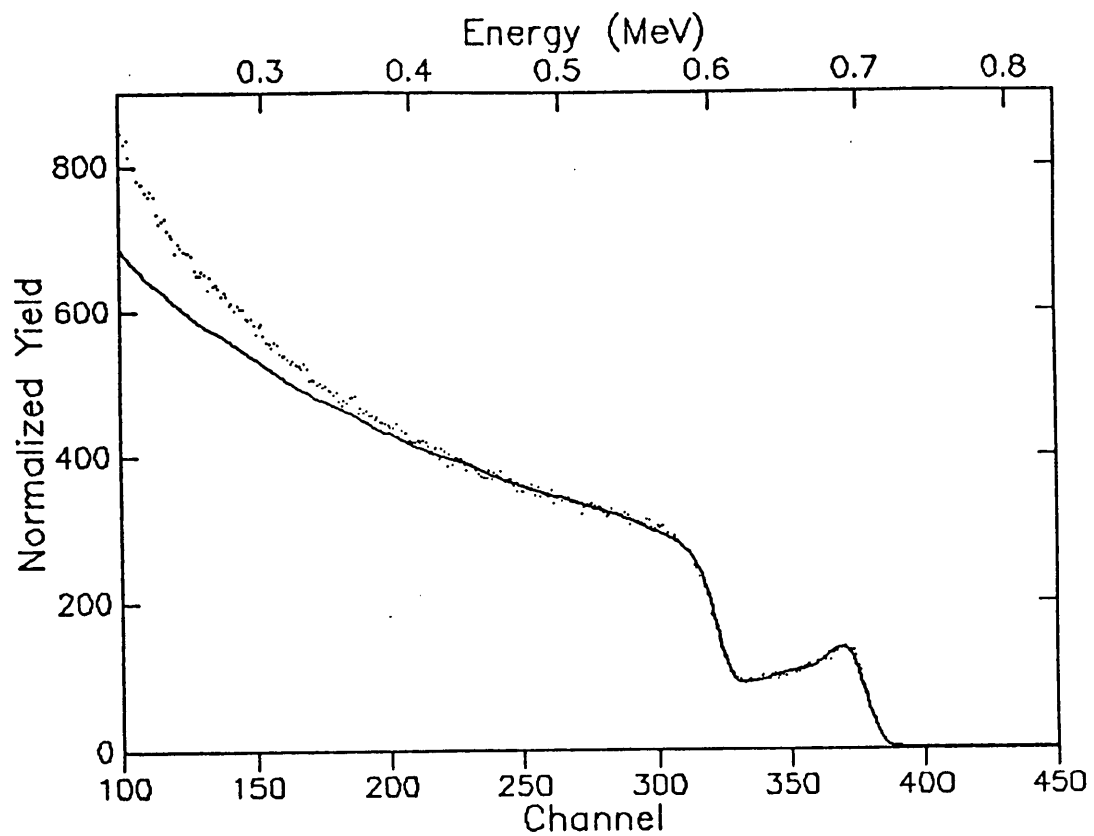


```

Current File: [GIRIDHAR.JAY]ANA5.RBS;1
Identifier: Sn film on Fe [~1200 Å] Unirr. (ana5.rob)
Date: January 26, 1987
0.800 MeV      3.25 uCoulombs
Channel Energy Constants:    1.7854      23.1343
Correction Factor:   1.0000
Angles (Theta, Phi, Omega):   0.0000      20.0000      3.000
Livetime text:
Channel number of first data point:      0.0
Number of data points:      513
Detector FWHM:      20.0 keV      Beam: He+
RMS Beam current:     9.0 nA      Geometry: IBM

```

Figure 67. Experimental and simulated RBS spectra of an as-deposited $\sim 1200 \text{ \AA}$ Sn film on Fe substrate.

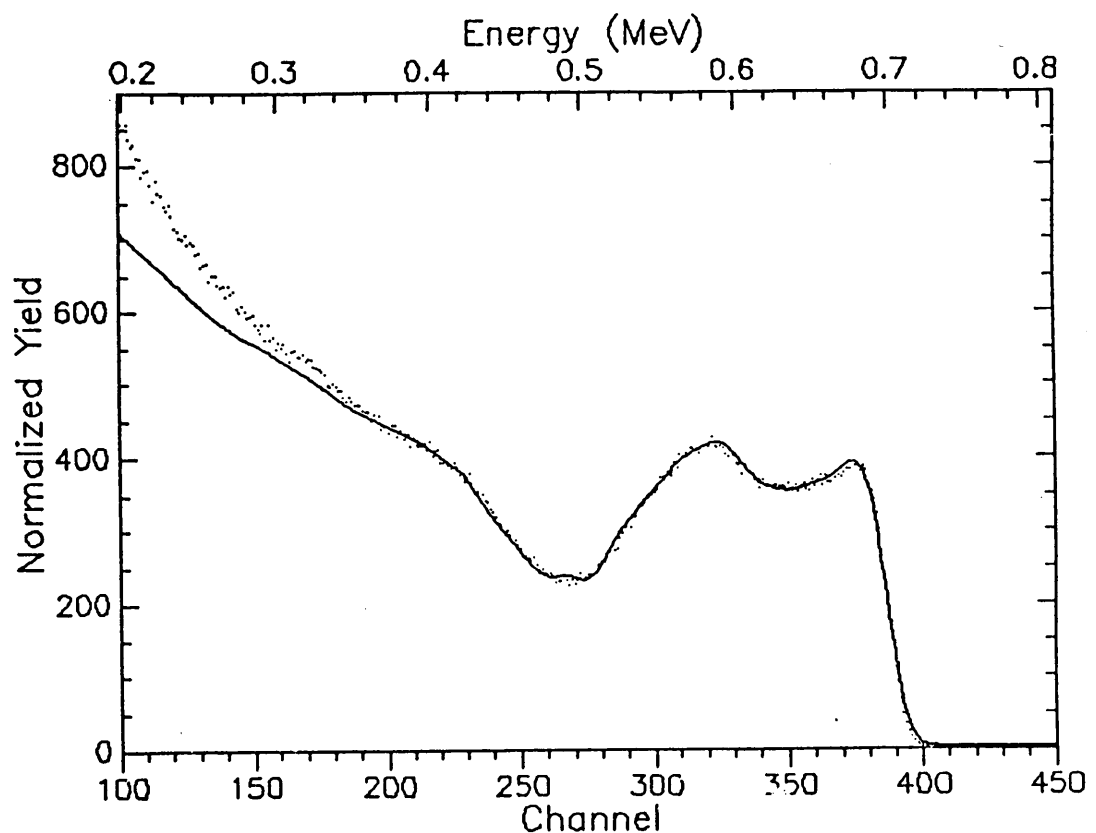


```

Current File: [GIRIDHAR.JAY]ANABB.RBS;1
Identifier: Sn film on Fe [~1200 Å] Irr.(4.E16) 180 C
Date: Feb 03, 1987
0.800 MeV    2.70 uCoulombs
Channel Energy Constants:      1.7966      24.2798
Correction Factor:      1.0000
Angles (Theta, Phi, Omega):   0.0000     20.0000     3.000
Livetime text:
Channel number of first data point:      0.0
Number of data points:      513
Detector FWHM:      20.0 keV      Beam: He+
RMS Beam current:      4.0 nA      Geometry: IBM

```

Figure 68. Experimental and simulated RBS spectra after irradiation at 20°K and fluence of 4×10^{16} ions/cm²

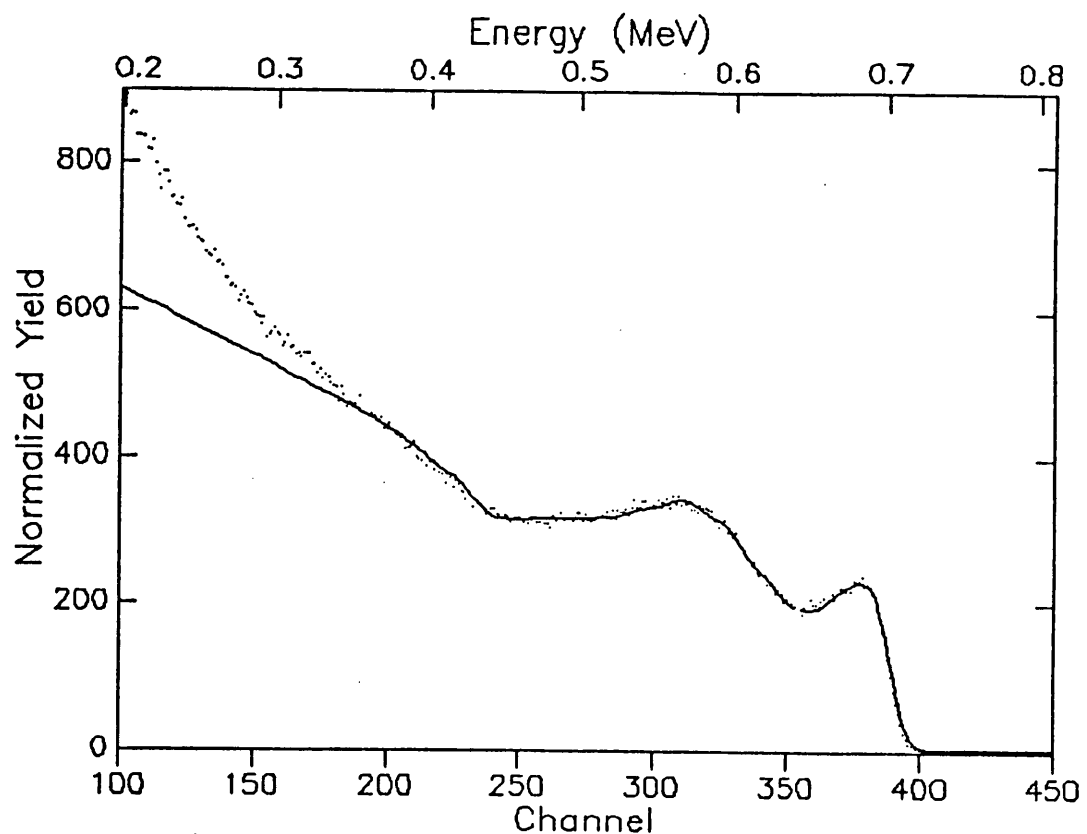


```

Current File: [GIRIDHAR.JAY]ANA56.RBS;1
Identifier: Sn film on Fe [~1200 Å] Irr. {6.E16} (ana5g.rob)
Date: January 28, 1987
0.800 MeV    2.80 uCoulombs
Channel Energy Constants:   1.7475    22.5783
Correction Factor:   1.0000
Angles (Theta, Phi, Omega):   0.0000    21.0000    3.000
Livetime text:
Channel number of first data point:   2.0
Number of data points:  513
Detector FWHM:   20.0 keV      Beam: He+
RMS Beam current:   7.0 nA      Geometry: IBM

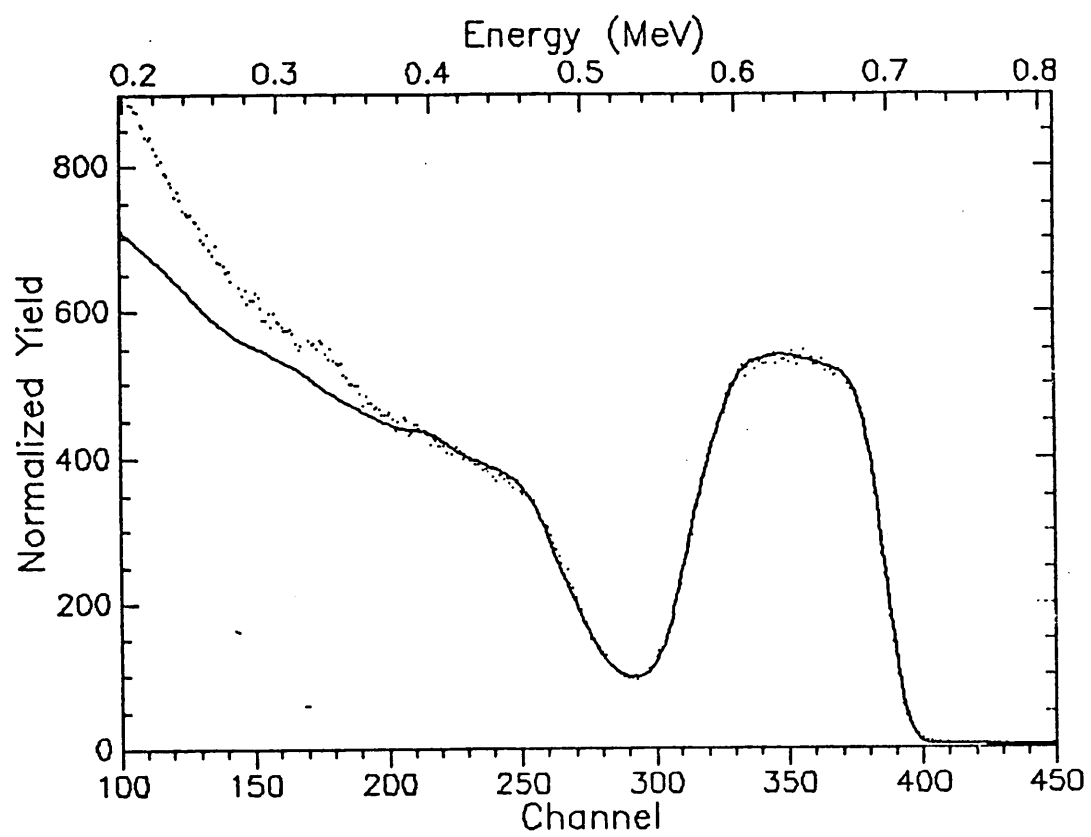
```

Figure 69. Experimental and simulated RBS spectra after irradiation at 20°K and fluence of 6×10^{16} ions/cm².



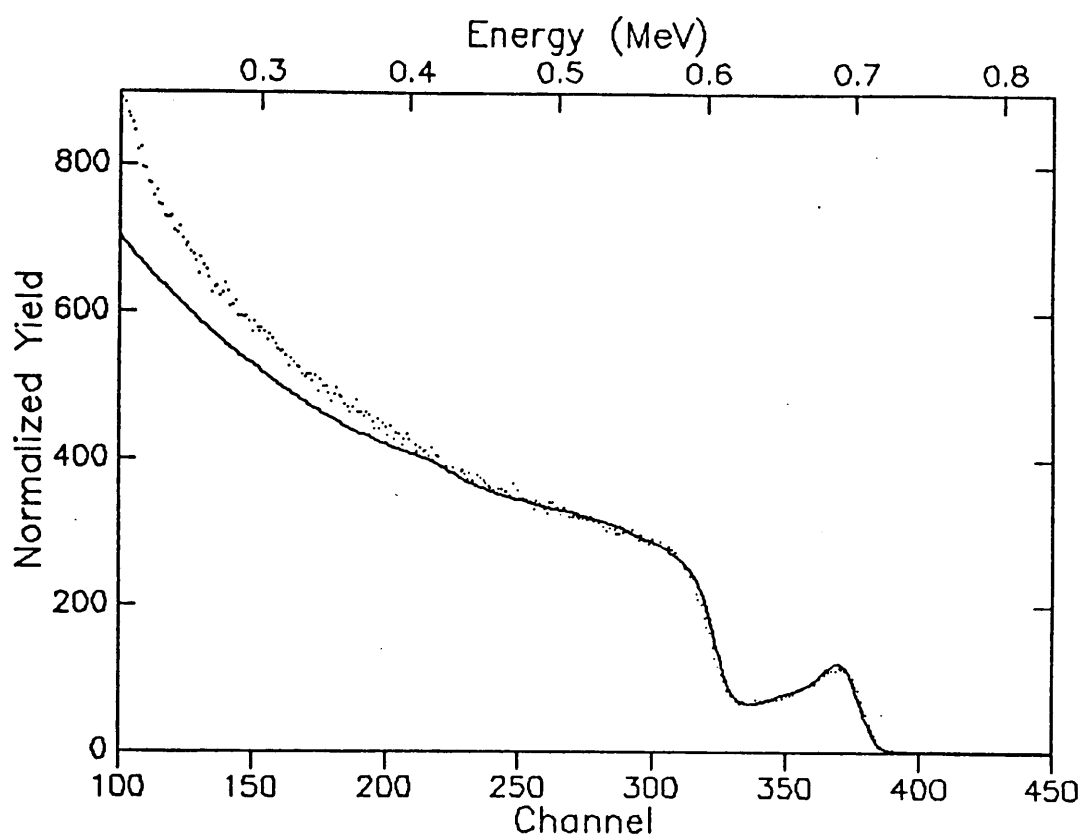
Current File: [GIRIDHAR.JAY]ANASJ.RBS;1
 Identifier: Sn film on Fe [~ 1200 Å] Irr. (8.E16)
 Date: January 29, 1987
 0.800 MeV 2.60 uCoulombs
 Channel Energy Constants: 1.7475 22.5783
 Correction Factor: 1.0000
 Angles (Theta, Phi, Omega): 0.0000 21.0000 3.000
 Livetime text:
 Channel number of first data point: 0.0
 Number of data points: 513
 Detector FWHM: 20.0 keV Beam: He+
 RMS Beam current: 7.0 nA Geometry: IBM

Figure 70. Experimental and simulated RBS spectra after irradiation at 20°K and fluence of 8×10^{16} ions/cm².



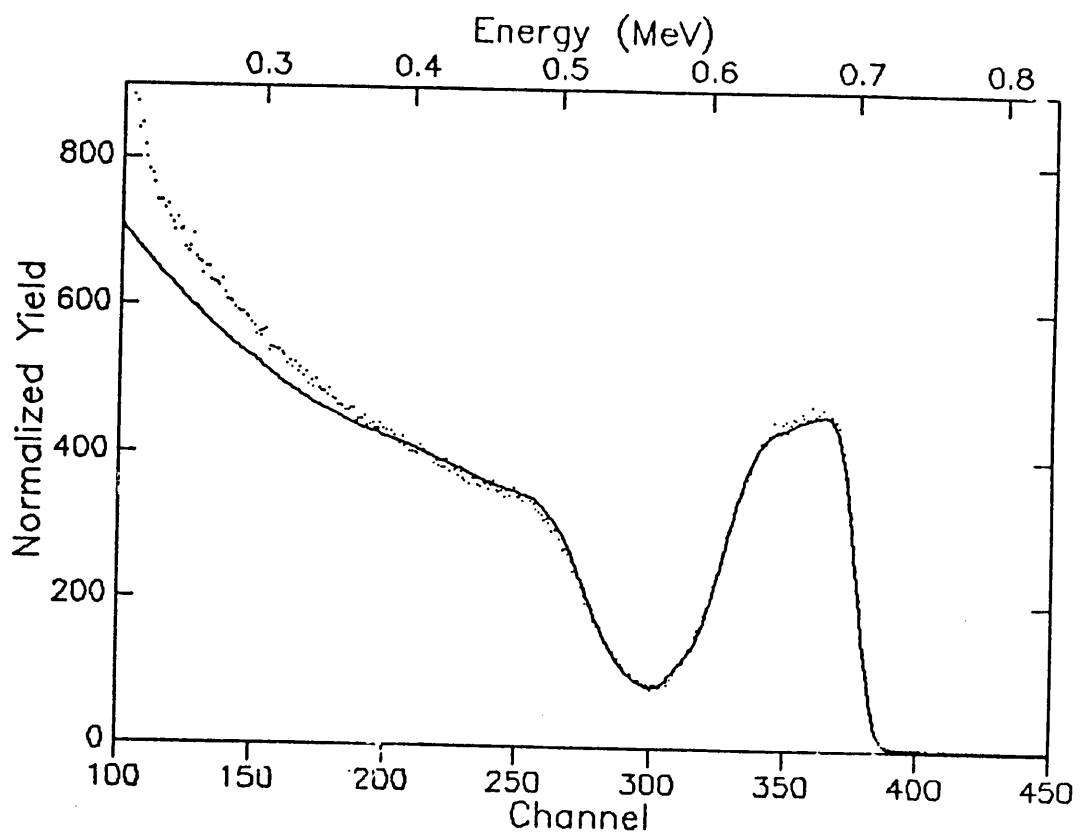
Current File: [GIRIDHAR.JAY]ANASD.RBS;1
 Identifier: Sn film on Fe [~ 1200 Å] Irr. {4.E16}
 Date: Jan 27, 1987
 0.800 MeV 3.25 uCoulombs
 Channel Energy Constants: 1.7475 22.5783
 Correction Factor: 1.0000
 Angles (Theta, Phi, Omega): 0.0000 21.0000 3.000
 Livetime text:
 Channel number of first data point: 10.0
 Number of data points: 513
 Detector FWHM: 20.1 keV Beam: He+
 RMS Beam current: 7.0 nA Geometry: IBM

Figure 71. Experimental and simulated RBS spectra after irradiation at 180°C and fluence of 4×10^{16} ions/cm².



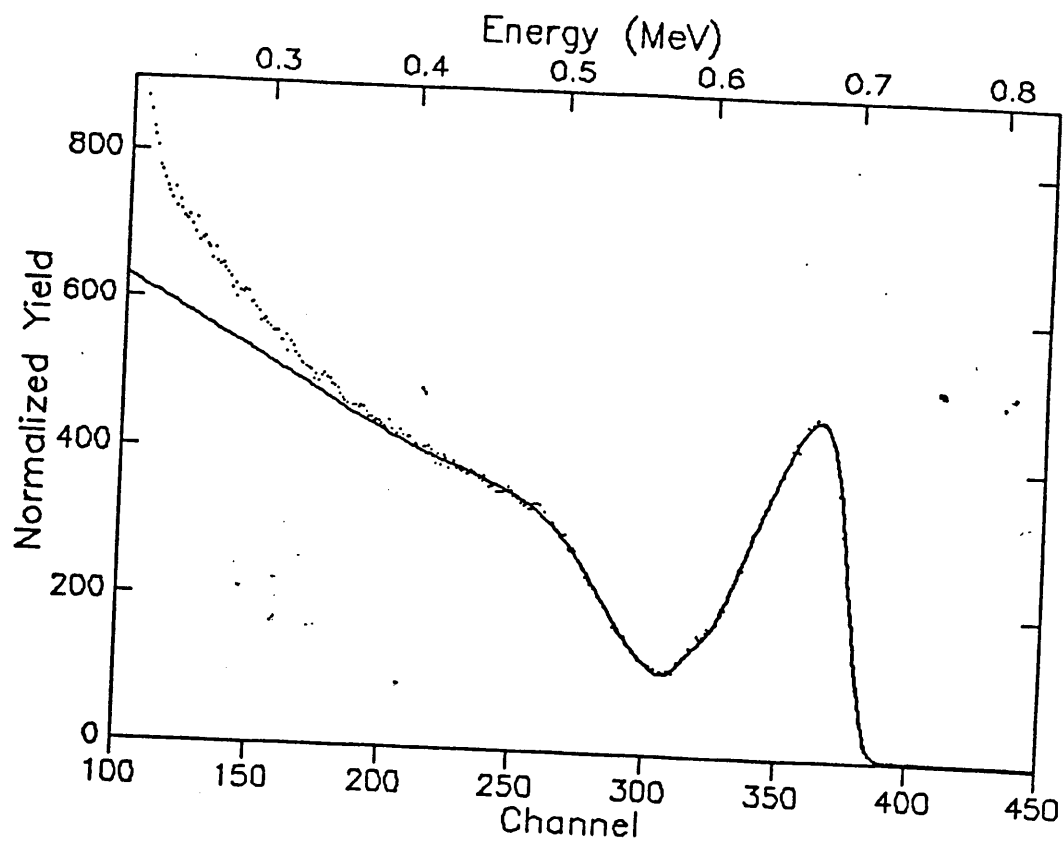
Current File: [GIRIDHAR.JAY]ANA6B.RBS;1
 Identifier: Sn film on Fe [~ 1200 Å] Irr. (8×10^{16}) 180 °C
 Date: Feb 2 , 1987
 0.800 MeV 2.60 uCoulombs
 Channel Energy Constants: 1.7966 24.2798
 Correction Factor: 1.0000
 Angles (Theta, Phi, Omega): 0.0000 20.0000 3.000
 Livetime text:
 Channel number of first data point: 2.0
 Number of data points: 513
 Detector FWHM: 20.0 keV Beam: He+
 RMS Beam current: 4.0 nA Geometry: IBM

Figure 72. Experimental and simulated RBS spectra after irradiation at 180°C and fluence of 8×10^{16} ions/cm².



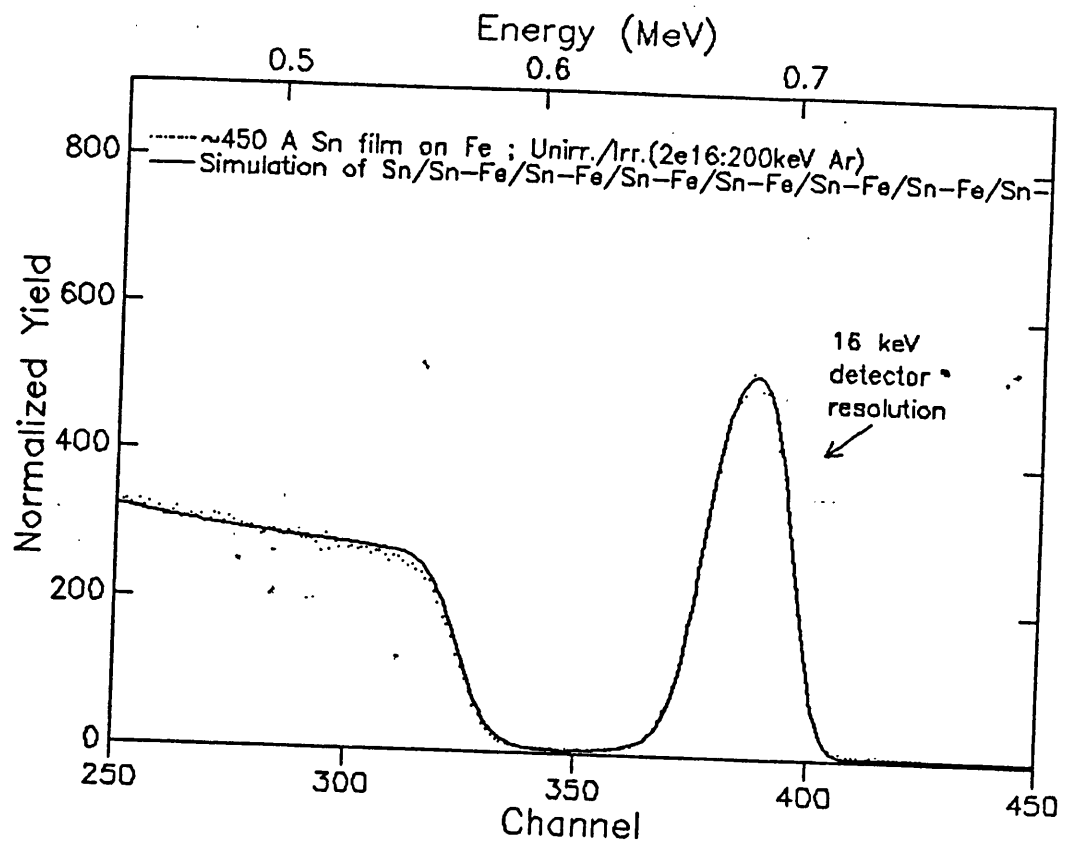
Current File:
 Identifier: Sn film on Fe [~1200 Å] Irr. {6.0E16@400keV Ar}
 Date: Feb 03, 1987
 0.800 MeV 2.55 uCoulombs
 Channel Energy Constants: 1.7966 24.2798
 Correction Factor: 1.0000
 Angles (Theta, Phi, Omega): 0.0000 20.0000 3.000
 Livetime text:
 Channel number of first data point: 0.0
 Number of data points: 513
 Detector FWHM: 20.0 keV Beam: He+
 RMS Beam current: 4.0 nA Geometry: IBM

Figure 73. Experimental and simulated RBS spectra after irradiation with 400keV Ar and fluence of 6×10^{16} ions/cm².



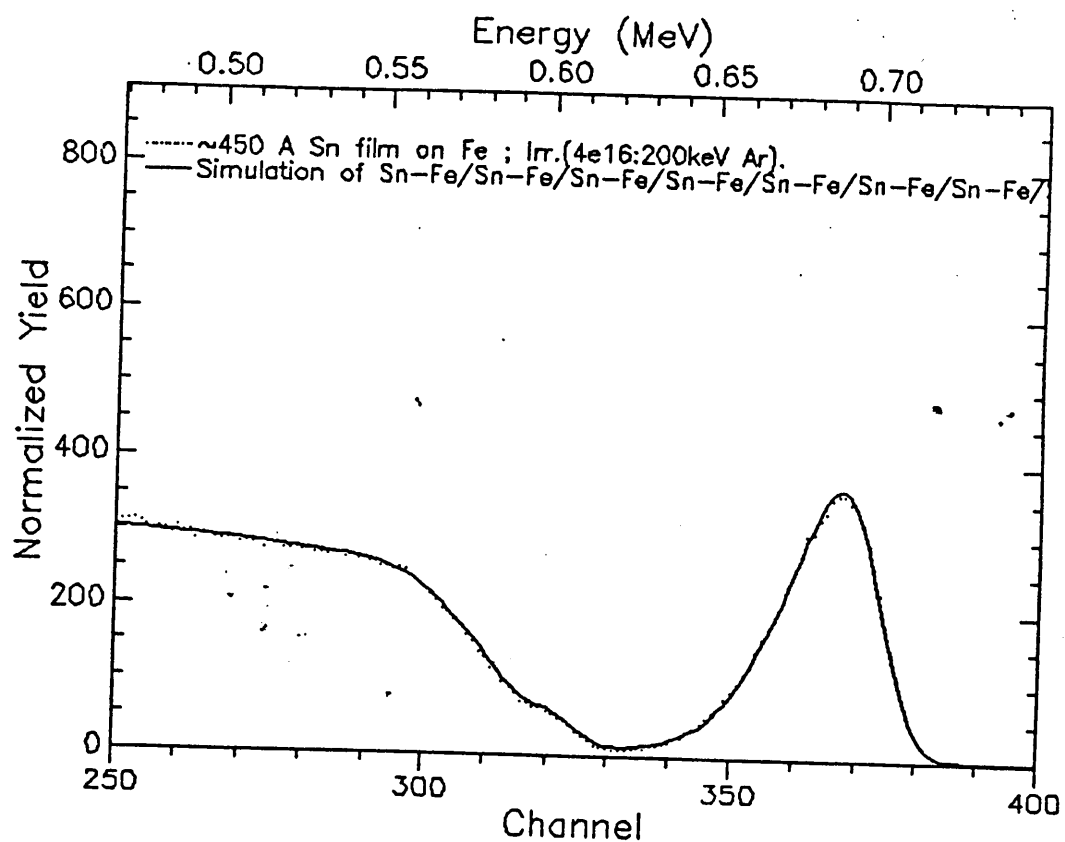
Current File: ANA2B.RBS
 Identifier: Sn film on Fe [\sim 1200 Å] Irr. {8.0E16|400keV Ar}
 Date: Feb 04, 1987
 0.800 MeV 3.00 uCoulombs
 Channel Energy Constants: 1.7966 24.2798
 Correction Factor: 1.0000
 Angles (Theta, Phi, Omega): 0.0000 20.0000 3.000
 Livetime text:
 Channel number of first data point: 0.0
 Number of data points: 513
 Detector FWHM: 20.0 keV Beam: He+
 RMS Beam current: 4.0 nA Geometry: IBM

Figure 74. Experimental and simulated RBS spectra after irradiation with 400keV Ar and fluence of 8×10^{16} ions/cm².



Current File: [GIRIDHAR.GIRI]SNFE2.RBS;1
Identifier: ~450 A Sn film on Fe ; Unirr./Irr. (2e16:200keV
Date:
0.800 MeV 2.50 uCoulombs
Channel Energy Constants: 1.7973 -10.4200
Correction Factor: 1.0000
Angles (Theta, Phi, Omega): 0.0000 20.0000 3.000
Livetime text:
Channel number of first data point: 209.0
Number of data points: 304
Detector FWHM: 16.0 keV Beam: He+
RMS Beam current: 9.0 nA Geometry: IBM

Figure 75. Experimental and simulated RBS spectra of an as-deposited ~ 450 Å Sn film on Fe.

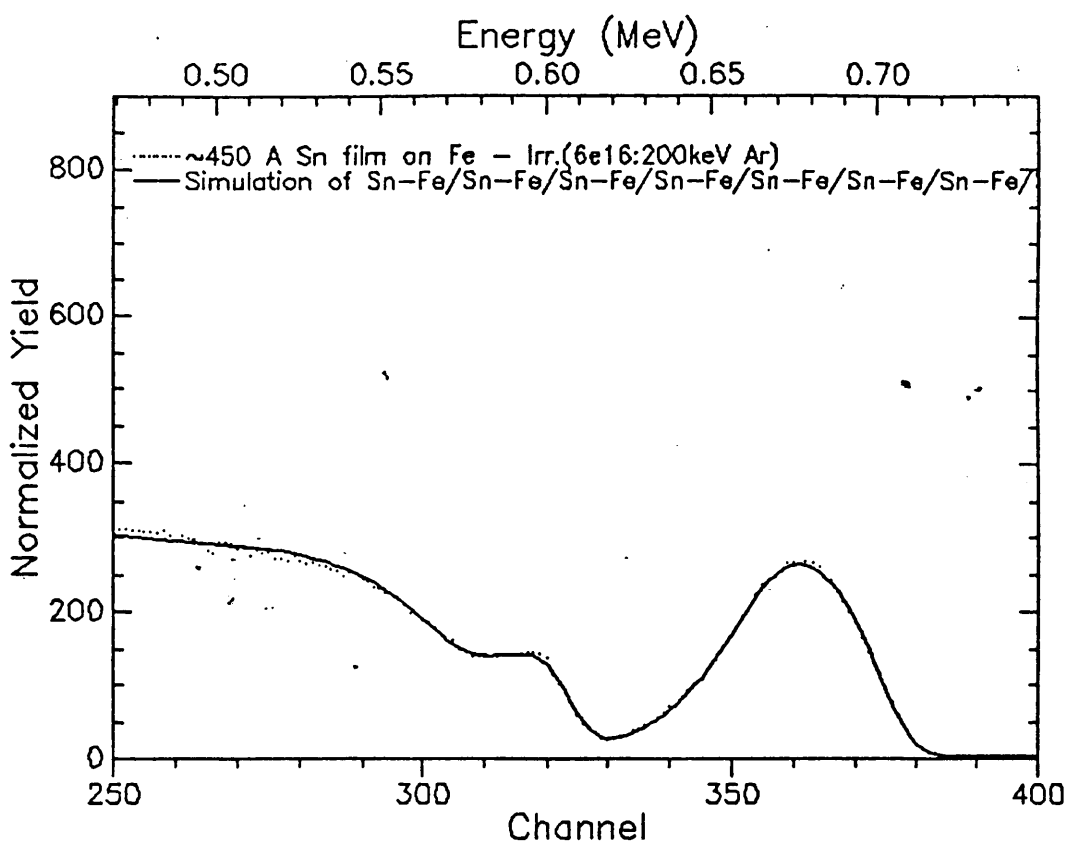


```

Current File: [GIRIDHAR.GIRI]SNFE4.RBS;i
Identifier: ~450 Å Sn film on Fe ; Irr.(4e16:200keV Ar).
Date:
0.801 MeV      4.38 uCoulombs
Channel Energy Constants:      1.8686      2.2072
Correction Factor:      1.0000
Angles (Theta, Phi, Omega):      0.0000      20.0000      3.000
Livetime text:
Channel number of first data point: 162.0
Number of data points: 343
Detector FWHM:      17.4 keV      Beam: He+
RMS Beam current:    7.0 nA      Geometry: IBM

```

Figure 76. Experimental and simulated RBS spectra after irradiation with 200keV Ar and fluence of 4×10^{16} ions/cm².



Current File: [GIRIDHAR.GIRI]SNFE6A.RBS;1
Identifier: ~450 A Sn film on Fe - Irr.(6e16:200keV Ar)
Date:
0.801 MeV 4.15 uCoulombs
Channel Energy Constants: 1.8686 2.2072
Correction Factor: 1.0000
Angles (Theta, Phi, Omega): 0.0000 20.0000 3.000
Livetime text:
Channel number of first data point: 250.0
Number of data points: 152
Detector FWHM: 17.4 keV Beam: He+
RMS Beam current: 9.0 nA Geometry: IBM

Figure 77. Experimental and simulated RBS spectra after irradiation with 200keV Ar and fluence of 6×10^{16} ions/cm².

**The vita has been removed from
the scanned document**